

NATIONAL TECHNICAL UNIVERSITY OF ATHENS

SCHOOL OF ELECTRICAL AND COMPUTER ENGINEERING DIVISION OF SIGNALS, CONTROL AND ROBOTICS

Teager–Kaiser Energy Operator for the Analysis of Brain Signal Dynamics

DIPLOMA THESIS of

Ioanna Chourdaki

Supervisor: Petros Maragos

Professor NTUA



NATIONAL TECHNICAL UNIVERSITY OF ATHENS

SCHOOL OF ELECTRICAL AND COMPUTER ENGINEERING DIVISION OF SIGNALS, CONTROL AND ROBOTICS

Teager–Kaiser Energy Operator for the Analysis of Brain Signal Dynamics

DIPLOMA THESIS of

Ioanna Chourdaki

Supervisor: Po	etros Maragos rofessor NTUA	
Approved by the ϵ	examining committee on 17 th October, 2025.	
Petros Maragos Professor NTU	Athanasios Rontogiannis	Ioannis Kordonis Assistant Professor NTUA

Athens, October 2025

Ioanna Chourdaki Graduate of Electrical and Computer Engineering NTUA
Copyright © Ioanna Chourdaki, 2025.
All rights reserved. Copying, storing and distributing this work, in whole or in part, for commercial purposes is prohibited. Reproduction, storing and distributing for non-profit, educational or research purposes is permitted, provided that the source is acknowledged and this message is retained. Questions regarding the use of the work for commercial purposes should be addressed to the author.

not be interpreted as representing the official positions of the National Technical University

of Athens.



Περίληψη

Τα σήματα του εγκεφάλου, όπως το Ηλεκτροεγκεφαλογράφημα (ΗΕΓ), μπορούν να προσεγγιστούν ως σήματα Διαμόρφωσης Πλάτους-Συχνότητας (ΑΜ-FM), τα οποία αποτυπώνουν τη θεμελιωδώς ταλαντωτική και δυναμική φύση της νευρωνικής δραστηριότητας. Σε αυτή την αναπαράσταση, το στιγμιαίο πλάτος και η στιγμιαία συχνότητα περιέχουν ουσιώδεις πληροφορίες για τη φυσιολογία του εγκεφάλου, που σχετίζονται με τις μεταβολές ενέργειας και τον συγχρονισμό των νευρώνων. Ωστόσο, η εξαγωγή αυτών των συνιστωσών από τα ΗΕΓ είναι ιδιαίτερα απαιτητική, λόγω του μη γραμμικού, μη στάσιμου και ευαίσθητου στον θόρυβο χαρακτήρα τους. Στην παρούσα Διπλωματική Εργασία, διερευνάται η χρήση του μη γραμμικού Τελεστή Ενέργειας Τeager-Καίser (ΤΚΕΟ) ως εργαλείο για την αποδιαμόρφωση ΗΕΓ και την ανάλυση της ενέργειας σε γνωστικά και κλινικά πειράματα.

Καθότι ο εν λόγω τελεστής είναι κατάλληλος για σήματα στενής ζώνης, εφαρμόζεται αρχικά συστοιχία φίλτρων Gabor, με σκοπό την απομόνωση των συχνοτικών μπαντών του ΗΕΓ. Στη συνέχεια, χρησιμοποιείται ο Αλγόριθμος Διαχωρισμού Ενέργειας διακριτού χρόνου (DESA-1) για την εξαγωγή του στιγμιαίου πλάτους και της στιγμιαίας συχνότητας σε κάθε υπο-μπάντα, επιτρέποντας λεπτομερή ανάλυση των δυναμικών διαμόρφωσης πλάτους—συχνότητας. Από την ενέργεια Teager—Καίser και τις συνιστώσες αποδιαμόρφωσης, προκύπτει ένα εκτενές σύνολο χαρακτηριστικών. Για τη συστηματική αξιολόγησή τους, επιλέγουμε τρία αντιπροσωπευτικά προβλήματα του πεδίου των ΗΕΓ — Αναγνώριση Συναισθήματος, Ταξινόμηση Κινητικής Νο-ερής Απεικόνισης και Ανίχνευση Επιληψίας — και τα συγκρίνουμε με συμβατικά ενεργειακά και φασματικά χαρακτηριστικά. Αποσκοπώντας στην εκτίμηση της γενίκευσης της μεθόδου μας, εξάγουμε πειράματα τόσο σε εξαρτώμενο από το άτομο (Subject-Dependent), όσο και σε ανεξάρτητο (Subject-Independent) πλαίσιο.

Τα πειραματικά αποτελέσματα δείχνουν ότι τα ΤΚΕΟ χαρακτηριστικά επιτυγχάνουν υψηλότερη απόδοση ταξινόμησης στα προβλήματα Κινητικής Νοερής Απεικόνισης και Ανίχνευσης Επιληψίας σε σύγκριση με τα συμβατικά χαρακτηριστικά, ενώ παρουσιάζουν αντίστοιχα αποτελέσματα στην Αναγνώριση Συναισθήματος. Επιπλέον, η συνένωση χαρακτηριστικών μεταξύ συχνοτικών μπαντών βελτιώνει τη συνολική απόδοση, υπογραμμίζοντας την ευαισθησία των ΤΚΕΟ χαρακτηριστικών στις πιο στενές ζώνες. Αναλύοντας τα αποτελέσματα διαφορετικών συστοιχίων φίλτρων Gabor, παρατηρούμε ότι η αύξηση του αριθμού των φίλτρων βελτιώνει την απόδοση στις περισσότερες περιπτώσεις, καθώς η λεπτομερέστερη φασματική αποσύνθεση επιτρέπει στον ΤΚΕΟ να ανιχνεύει ενεργειακές διακυμάνσεις που διαφορετικά θα εξομαλύνονταν. Πέραν των αριθμητικών δεικτών απόδοσης, τα εξαγόμενα χαρακτηριστικά διατηρούν βιολογική ερμηνεία, αποτυπώνοντας άμεσα τις στιγμιαίες ενεργειακές και συχνοτικές μεταβολές που διέπουν τη νευρωνική δραστηριότητα.

Λέξεις Κλειδιά — Ενεργειαχός Τελεστής Teager–Kaiser, Διαμόρφωση Πλάτους–Συχνότητας, Αλγόριθμος Διαχωρισμού Ενέργειας, Ηλεκτροεγκεφαλογράφημα (ΗΕΓ), Αναγνώριση Συναισθήματος, Κινητική Νοερή Απεικόνιση, Ανίχνευση Επιληψίας

Abstract

Brain signals such as Electroencephalography (EEG) can be effectively modeled as Amplitude–Frequency Modulated (AM–FM) signals, reflecting the intrinsic oscillatory and dynamic nature of neural activity. In this representation, the instantaneous amplitude and frequency capture physiologically meaningful information about energy variations and neuronal synchrony. However, the extraction of such components from EEG is challenging due to the signal's non-linear, non-stationary, and noise-prone characteristics. In this Thesis, we investigate the Teager–Kaiser Energy Operator (TKEO) as a non-linear tool for demodulating EEG signals and analyze their energy dynamics across cognitive and clinical EEG paradigms.

To accommodate the narrowband nature of the operator, a Gabor filterbank is first applied to isolate canonical frequency bands. The Discrete Energy Separation Algorithm (DESA-1) is then employed to extract the amplitude envelope and the instantaneous frequency components within each sub-band, enabling a detailed analysis of amplitude–frequency modulated dynamics. From both the Teager-Kaiser energy and the demodulation components, we derive a comprehensive set of energy-based descriptors. These features are systematically evaluated across three representative EEG classification tasks—Emotion Recognition, Motor Imagery, and Epilepsy Detection—and compared with conventional energy and spectral-domain features, under both Subject-Dependent and Subject-Independent settings to assess generalization performance.

Experimental results demonstrate that TKEO-based features yield higher classification performance in Motor Imagery and Epilepsy Detection, while achieving comparable results in Emotion Recognition. Furthermore, feature fusion across frequency bands enhances overall performance, emphasizing the narrowband sensitivity of TKEO-based descriptors. Analysis of the filterbank configuration shows that increasing the number of filters improves performance in most cases, as finer spectral decomposition enables TKEO to capture subtle energy fluctuations that would otherwise be averaged out. Beyond quantitative improvements, the extracted features retain physiological interpretability, directly reflecting the instantaneous energy and frequency modulations underlying neural activity.

Keywords — Teager-Kaiser Energy Operator, Amplitude-Frequency Modulation, Energy Separation Algorithm, EEG, Emotion Recognition, Motor Imagery, Epilepsy Detection

Ευχαριστίες

Η παρούσα Δ ιπλωματική αποτελεί την τελευταία εργασία που καλούμαι να παραδώσω στα πλαίσια της Σ χολής μου, σηματοδοτώντας το κλείσιμο ενός ιδιαίτερα σημαντικού και καθοριστικού για εμένα κύκλου. Θα ήθελα, λοιπόν, να ευχαριστήσω τους εξής ανθρώπους που με βοήθησαν και συνόδεψαν, τόσο κατά το διάστημα εκπόνησης της Δ ιπλωματικής Eργασίας, όσο και καθ' όλη τη διάρκεια των 6 ετών φοίτησής μου:

Τον επιβλέποντα καθηγητή, κύριο Πέτρο Μαραγκό, για την ουσιαστική συμβολή του στην ενίσχυση του ενδιαφέροντός μου για την έρευνα, ήδη από τα πρώτα προπτυχιακά μαθήματα που παρακολούθησα μαζί του, μέσα από την παρότρυνσή του προς τους φοιτητές να συμμετέχουν σε εκδηλώσεις και ομιλίες ερευνητικού περιεχομένου, καθώς και για τη συνεργασία και καθοδήγησή του κατά την εκπόνηση της Διπλωματικής Εργασίας.

Τους συν-επιβλέποντες της Διπλωματικής μου: μεταδιδακτορική ερευνήτρια Δρ. Νάνσυ Ζλαντίντση, υποψήφιο διδάκτορα Χρήστο Γαρούφη και υποψήφιο διδάκτορα Κλεάνθη Αβραμίδη, ο οποίος - παρότι βρίσκεται σε άλλη ήπειρο - ήταν πάντα εδώ, με αμέριστη προσοχή και πολύ καλή διάθεση. Η συμβολή σας ήταν καθοριστική και σας είμαι ευγνώμων!

Τις φίλες μου Ιόλη, Μαργαρίτα και Νεφέλη, οι οποίες ήταν και είναι το σημείο αναφοράς μου σε κάθε σημαντικό (και μη) βήμα μου.

Τους γονείς μου, Λ ίνα και Γιώργο, για κάθε εφόδιο, άποψη, συζήτηση, σκέψη και την αδιάκοπη και έμπρακτη στήριξη όλα αυτά τα χρόνια.

Τον Γιάννη, ο οποίος είναι πάντα δίπλα μου, δίνοντας μου ώθηση, δύναμη και χρώμα.

Ιωάννα Χουρδάκη Οκτώβριος 2025

Contents

\mathbf{C}	Contents			
Li	st of	Figure	es es	16
Li	st of	Tables	3	18
E :	κτετ	αμένη	Περίληψη	21
1	Intr	oducti	on	44
	1.1 1.2 1.3 1.4 1.5	1.1.1 1.1.2 1.1.3 1.1.4 1.1.5 Theory Theory	Analysis Fundamentals Brain Anatomy Physiology of Neurons Electroencephalography Signals EEG Channels Frequency Bands y of Emotion y of Motor Imagery y of Epilepsy Structure & Contributions	. 44 . 45 . 46 . 48 . 50 . 51
2	The	eoretica	al Background	56
-	2.1	Signal	Processing Fundamentals	. 56
		2.1.1	What is a Signal?	
		2.1.2	What is a System?	
		2.1.3	Fourier Analysis	
		2.1.4	Energy and Power of a Signal	
		2.1.5	Signal Filtering	
		2.1.6	Signal Decomposition	
	0.0	2.1.7	Biosignals	
	2.2	Teager	:-Kaiser Energy Operator	. 65

Contents

		2.2.1	Energy Separation Algorithm	66
		2.2.2	Applying Filterbanks on TKEO	68
	2.3	Machi	ne Learning Models	68
		2.3.1	Support Vector Machines	69
		2.3.2	Random Forests	72
3	Rel	ated W	Vork & Methodology	75
	3.1		ets	75
	3.2	Literat	ture Review	76
		3.2.1	Traditional EEG Features	76
		3.2.2	TKEO Applications	76
		3.2.3	EEG-Based Emotion Recognition Methods	77
		3.2.4	EEG-Based Motor Imagery and BCI Systems	78
		3.2.5	EEG-Based Epilepsy Detection Methods	79
	3.3	Prepro	ocessing	80
	3.4	Featur	re Extraction	82
		3.4.1	Baseline Features	82
		3.4.2	TKEO Features	83
		3.4.3	Selection of TKEO Features	87
	3.5	Evalua	ation Protocol	88
		3.5.1	Classification Models	88
		3.5.2	Evaluation Metrics	88
4	Res	sults &	Discussion	91
	4.1	SEED	Results	91
	4.2	DEAP	Results	94
	4.3	BCI-I	V 2a Results	96
	4.4	TUEP	Results	99
	4.5	Ablati	on Study	101
	4.6	Summ	ary	103
5	Cor	nclusio	n	104
	5.1		ary of the Contributions	104
	5.2		e Work	105
\mathbf{A}_{1}	ppen	dix A:	The SEED Dataset	106
\mathbf{A}	ppen	dix B:	The DEAP Dataset	110
	-		The BCI-IV 2a Dataset	115
^	phen	idix C:	The DOT-IV 2a Dataset	тто

Contents	Contents
Appendix D: The TUEP Dataset	118
Appendix E: List of Publications	120
Bibliography	121

List of Figures

	υστοιχία Φίλτρων Gabor, αποτελούμενη από 12 φίλτρα σε κατανομή Mel με
	τικάλυψη 50% (Ρυθμός Δ ειγματοληψίας $=22.05~ m{kHz}$) $[123]$
3 E	φαρμογή Ανάλυσης Ανεξάρτητων Συνιστωσών σε ΗΕΓ από το Σύνολο Δε-
δι	ρμένων TUEP
4 E	φαρμογή Συστοιχίας Φίλτρων Gabor με 12 Φίλτρα στα Κανάλια από ένα ΗΕΓ
τ	ου Συνόλου Δεδομένων DEAP στην Beta Μπάντα
	χετικές τετραγωνικές και Teager–Kaiser ενέργειες του καναλιού FC4 από το ύνολο δεδομένων BCI-IV 2a στη ζώνη Alpha. Οι γκρι διακεκομμένες κάθετες
	ραμμές αντιστοιχούν στην έναρξη του ερεθίσματος $(1\mathrm{s})$, στη λήξη του ερεθίσ-
-	ατος $(2.25 \mathrm{s})$ και στη λήξη της φάσης κινητικής νοερής απεικόνισης $(5 \mathrm{s})$. Η
	χετική ενέργεια ΤΚΕΟ παρουσιάζει λιγότερες διακυμάνσεις εντός κάθε περιό-
	ου, παραμένοντας χαμηλή κατά τη διάρκεια της κινητικής νοερής απεικόνισης
(1	ΜΙ) και υψηλότερη κατά τις περιόδους ηρεμίας, υποδεικνύοντας ότι η σχετική
	νέργεια ΤΚΕΟ προσφέρει μια πιο ομαλή και διακριτική αναπαράσταση γία την
	$ ext{II.}$
	α) Σήμα καναλιού CP4 από το σύνολο δεδομένων BCI-IV 2a στη ζώνη Alpha.
	ο) Τετραγωνική ρίζα του ΤΚΕΟ. (c) Εκτιμώμενη περιβάλλουσα πλάτους με
	ρήση του DESA-1. (d) Εκτιμώμενη στιγμιαία συχνότητα με χρήση του DESA-
	, εχφρασμένη ως χλάσμα του π
	οπολογική Απεικόνιση των ΗΕΓ Καναλιών του Συνόλου Δεδομένων TUEP
X	άθε Συχνοτικής Μπάντας για το Χαρακτηριστικό v-IFM 43
1.1 L	obes of the Brain [83] 44
1.2 T	the Structure of a Neuron [99]
	0-20 System [10]: Schematic Overview of Electrode Placement
1.4 E	EG Recording Setup with Representative Signals [17]
1.5 T	the Primary Frequency Bands of an EEG signal [14]
	rain Regions involved in Motor Execution (red) and Motor Imagery (blue),
\mathbf{s} l	nowing Overlapping and Distinct Activations across Cortical and Subcortical

List of Figures

List of Figures

1.8	Seizure Stages [48]: (a) Pre-ictal; (b) Transition from Pre-ictal to Ictal; (c) Ictal; (d) Transition from Ictal to Postictal; (e) Postictal	53
2.1 2.2	Normalized Frequency Response of a 1D Gabor Filter	62 63
2.3	Illustration of a Linear SVM showing the optimal separating hyperplane, support vectors, and margin between two classes.	69
2.4	Illustration of a Random Forest showing an Ensemble of N Decision Trees and their Aggregated Predictions for two Classes	72
3.1 3.2	Diagram of a MI-based BCI System for Exoskeleton Control [23] Independent Component Analysis (ICA) Applied to EEG Data From the TUEP Dataset. The Figure Shows the Original EEG Channel Signals (Left), the Time Courses of the Extracted ICA Components (Middle), the Corresponding Spatial Topographies of Selected Components (Right Middle), and	79
3.3	the Corrected EEG After Artifact Removal (Right)	81
3.4	right inset	82
3.5	were Notch-filtered at 50 Hz using Finite Impulse Response Band-pass filter. Relative Squared and Teager–Kaiser Energies of the FC4 Channel From the	83
J. J	BCI-IV 2a Dataset in the Alpha Band. Gray dotted vertical lines represent the Start of the Cue (1s), the End of the Cue (2.25s), and the End of Motor Imagery (5s). TKEO Relative Energy shows fewer variations within each period, remaining low during MI and higher during the Resting Periods, whereas SE exhibits more fluctuations. This indicates that TKEO Relative Energy pro-	
3.6	vides a smoother and more discriminative Representation for MI (a) CP4 Channel Signal from the BCI-IV 2a Dataset in the Alpha Band. (b)	86
	Square Root of TKEO. (c) Estimated Amplitude Envelope using DESA-1. (d) Estimated Instantaneous Frequency using DESA-1, expressed as a fraction of π .	87
3.7	Binary Classification Confusion Matrix, presenting key Evaluation Metrics	89
3.8	ROC Curves for Binary Classifiers, illustrating Model Performance against	00
	Random, with the AUC reported for one Model	90
4.1	Absolute SHAP Values of Frequency Bands, indicating their contributions to Fused-band TKEO Predictions across EEG Channels in BCI-IV 2a; higher	
	SHAP values represent greater contribution	98

List of Figures

List of Figures

4.2	Topology Maps of EEG Channels from the TUEP Dataset across Frequency	
	Bands of the v-IFM Feature	100
4.3	Comparison of Prediction Accuracies across Different Window Sizes and Fil-	
	terbank Configurations on the SEED Dataset for the Subject-Independent	
	Setting	101
4.4	Comparison of Prediction Accuracies across Different Window Sizes and Fil-	
	terbank Configurations on the SEED Dataset for the Subject-Dependent Setting.	102
A.1	Experimental Setup [122]	107
A.2	62-Channel EEG Electrode Layout [122]	108
B.1	Distribution of the 120 Candidate Music Video Stimuli in the Valence–Arousal	
	Space, based on Online Subjective Ratings. The 40 Final Clips used in the	
	DEAP Experiment are Highlighted in Green [59]	112
B.2	Placement of Physiological Sensors [59]	113
C.1	Timing scheme of one trial in the BCI Competition IV 2a Dataset [20]	116
C.2	Electrode montage for EEG (left) and EOG (right) recordings [20]	117

List of Tables

1	Παράμετροι Προεπεξεργασίας σε κάθε Σ ύνολο Δ εδομένων	31
2	Μετρικές Ακρίβειας για το Subject-Dependent στο Σύνολο Δεδομένων SEED.	37
3	Μετρικές Ακρίβειας για το Subject-Independent στο Σύνολο Δεδομένων SEED.	38
4	Μετρικές Ακρίβειας του Valence για το Subject-Dependent στο Σύνολο Δε-	
	δομένων DEAP	39
5	Μετρικές Ακρίβειας του Arousal για το Subject-Dependent στο Σύνολο Δε-	
	δομένων DEAP	39
6	Μετρικές Ακρίβειας του Valence για το Subject-Independent στο Σύνολο Δε-	
	δομένων DEAP	40
7	Μετρικές Ακρίβειας του Arousal για το Subject-Independent στο Σύνολο Δε-	
	δομένων DEAP	41
8	Μετρικές Ακρίβειας για το Subject-Dependent στο Σύνολο Δεδομένων BCI-IV	
	2a	41
9	Μετρικές Ακρίβειας για το Subject-Independent στο Σύνολο Δεδομένων BCI-	
	IV 2a	42
10	Μετρικές Ακρίβειας για το Subject-Independent στο Σύνολο Δεδομένων TUEP.	42
3.1	Dataset-wise Preprocessing Parameters	81
4.1	Subject-Dependent 5-fold Mean Classification Performance and Standard De-	
4.1	viation on SEED	92
4.2	Comparison of the Highest Reported Accuracies of Differential Entropy—based	52
4.2	Features in [122] with the Proposed TKEO-based Features on the SEED	
	Dataset for the Subject-Dependent Task	92
4.3	Subject-Independent 5-fold Mean Classification Performance and Standard	92
4.5	Deviation on SEED	93
4 4		93
4.4	Comparison of the Highest Reported Accuracies of the Proposed TKEO-based	
	Features with State-Of-The-Art Machine Learning Architectures on the SEED	02
	Dataset for the Subject-Independent Task	93

List of Tables

List of Tables

4.5	Subject-Dependent of Valence 5-fold Mean Classification Performance and	
	Standard Deviation on DEAP	Ć
4.6	Subject-Dependent of Arousal 5-fold Mean Classification Performance and	
	Standard Deviation on DEAP	Ć
4.7	Subject-Independent of Valence 5-fold Mean Classification Performance and	
	Standard Deviation on DEAP	Ć
4.8	Subject-Independent of Arousal 5-fold Mean Classification Performance and	
	Standard Deviation on DEAP	Ć
4.9	Comparison of the Highest Reported Accuracies of the Proposed TKEO-	
	based Features with State-of-the-Art Machine Learning Models on the DEAP	
	Dataset for the Subject-Independent Task	(
4.10	Subject-Dependent 5-fold Mean Classification Performance and Standard De-	
	viation on BCI-IV 2a	Ć
4.11	Subject-Independent 5-fold Mean Classification Performance and Standard	
	Deviation on BCI-IV 2a	Ć
4.12	Comparison of the Highest Reported Accuracies of the Proposed TKEO-based	
	Features with different Machine Learning Architectures proposed by [120] on	
	the BCI-IV 2a Dataset for the Subject-Independent Task	Ć
4.13	Subject-Independent 5-fold Mean Classification Performance and Standard	
	Deviation on TUEP	Ć
4.14	Comparison of the Highest Reported Accuracies of the Proposed TKEO-based	
	Features with State-Of-The-Art Machine Learning Architectures on the TUEP	
	Dataset for the Subject-Independent Task	10

Εκτεταμένη Περίληψη

Εισαγωγή

Ο Ανθρώπινος Εγκέφαλος

Ο ανθρώπινος εγκέφαλος αποτελεί το κύριο όργανο του νευρικού συστήματος, υπεύθυνο για την επεξεργασία αισθητηριακών πληροφοριών, τη ρύθμιση των σωματικών λειτουργιών και την εκδήλωση της σκέψης και των συναισθημάτων. Η Ηλεκτροεγκεφαλογραφία (ΗΕΓ) είναι μια μη επεμβατική μέθοδος καταγραφής της ηλεκτρικής δραστηριότητας του εγκεφάλου μέσω ηλεκτροδίων που τοποθετούνται στην επιφάνεια του κρανίου [101]. Η τοποθέτηση των ηλεκτροδίων ακολουθεί το διεθνές σύστημα 10–20 [25], το οποίο βασίζεται σε ανατομικά σημεία αναφοράς ώστε να εξασφαλίζεται η ομοιόμορφη κάλυψη όλων των εγκεφαλικών περιοχών και η αντιστοίχισή τους με συγκεκριμένα κανάλια μέτρησης. Πέρα από τη χωρική οργάνωση, τα ΗΕΓ σήματα αναλύονται και ως προς τη συχνοτική τους σύσταση, η οποία χωρίζεται σε πέντε κύριες συχνοτικές μπάντες [5]: Delta (0.5–3 Hz), Theta (4–7 Hz), Alpha (8–12 Hz), Beta (13–30 Hz) και Gamma (30–50 Hz). Κάθε μπάντα αντιστοιχεί σε διαφορετικές καταστάσεις εγκεφαλικής λειτουργίας, από τον βαθύ ύπνο (Delta) έως την ενεργή γνωστική επεξεργασία (Gamma [76]), προσφέροντας πολύτιμες ενδείξεις για τη μελέτη της νευρωνικής δραστηριότητας και την ανίχνευση νευρολογικών διαταραχών.

Θεωρία των Συναισθημάτων

Η μελέτη των ανθρώπινων συναισθημάτων αποτελεί διαχρονικό πεδίο έρευνας στην Ψυχολογία και τη Νευροεπιστήμη, με διάφορες θεωρητικές προσεγγίσεις να επιχειρούν να εξηγήσουν τη φύση και τη δομή τους [33], [37], [63], [93], [97]. Η θεωρία των James-Lange [63] υποστηρίζει ότι τα συναισθήματα αποτελούν συνειδητή αντίληψη των σωματικών αντιδράσεων, ενώ ο Ekman [36], [37] πρότεινε την ύπαρξη έξι βασικών καθολικών συναισθημάτων, και ο Plutchik [93] ανέπτυξε ένα ψυχοεξελικτικό μοντέλο οκτώ πρωτογενών συναισθημάτων σε κυκλική διάταξη. Τέλος, ο Russell [97], [98] εισήγαγε το διδιάστατο μοντέλο συναισθηματικού χώρου, με άξονες τη συναισθηματική ευχαρίστηση (valence) και τη διέγερση (arousal), το οποίο αποτελεί σήμερα

θεμελιώδες πλαίσιο στην ανάλυση και αναπαράσταση των συναισθημάτων.

Θεωρία της Κινητικής Νοερής Απεικόνισης

Η Κινητική Νοερή Απεικόνιση είναι η νοητική προσομοίωση μιας κίνησης χωρίς φυσική εκτέλεση, κατά την οποία ενεργοποιούνται περιοχές του εγκεφάλου που σχετίζονται με τον κινητικό σχεδιασμό και τον έλεγχο, όπως ο προκινητικός φλοιός και η παρεγκεφαλίδα [31], [71]. Έρευνες δείχνουν ότι η Κινητική Νοερή Απεικόνιση μοιράζεται κοινά νευρωνικά υποστρώματα με την πραγματική κίνηση και παρουσιάζει παρόμοιες χρονικές και φυσιολογικές δυναμικές, επιβεβαιώνοντας τη λειτουργική της ισοδυναμία με την εκτέλεση κίνησης [32], [86].

Θεωρία της Επιληψίας

Η επιληψία είναι χρόνια νευρολογική διαταραχή που χαρακτηρίζεται από προδιάθεση του εγκεφάλου να παράγει επιληπτικές κρίσεις, συνοδευόμενη από νευροβιολογικές, γνωστικές και ψυχολογικές επιπτώσεις [11], [39]. Η παθοφυσιολογία της σχετίζεται με αφύσικα συγχρονισμένες νευρωνικές εκφορτίσεις, λόγω διαταραχών στη νευροδιαβίβαση, τη λειτουργία της γλοίας ή την ιοντική ομοιόσταση, ενώ η διάγνωση βασίζεται κυρίως στην ηλεκτροεγκεφαλογραφία (ΗΕΓ) για τον εντοπισμό επιληπτομορφικών εκφορτίσεων και περιοχών έναρξης κρίσεων [30], [40]. Κλινικά, οι κρίσεις ταξινομούνται σε εστιακές, γενικευμένες και αγνώστου έναρξης, παρουσιάζοντας χαρακτηριστικά ΗΕΓ μοτίβα (spikes, sharp waves, ρυθμικές εκφορτίσεις) και διακριτές φάσεις εξέλιξης —από την προδρομική έως τη μετακριτική—που διευκολύνουν την παρακολούθηση και τη θεραπευτική παρέμβαση [106].

Θεωρητικό Υπόβαθρο

Βασική Θεωρία Επεξεργασίας Σημάτων

Η επεξεργασία σημάτων αποτελεί έναν επιστημονικό κλάδο που επικεντρώνεται στην ανάλυση, αναπαράσταση και τροποποίηση σημάτων, με σκοπό τη διευκόλυνση της εξαγωγής ή της ενίσχυσης των πληροφοριών που αυτά μεταφέρουν [87]. Ανάλογα με την εκάστοτε εφαρμογή, αυτό μπορεί να περιλαμβάνει διαδικασίες όπως η απομόνωση μεμονωμένων σημάτων από ένα μείγμα, η ανάδειξη συγκεκριμένων χαρακτηριστικών ενδιαφέροντος ή η εκτίμηση παραμέτρων που περιγράφουν ένα υποκείμενο μοντέλο σήματος. Στα συστήματα επικοινωνιών, για παράδειγμα, τα σήματα συνήθως υποβάλλονται σε μια σειρά προεπεξεργασιών —όπως διαμόρφωση ή συμπίεση—πριν από τη μετάδοση, ενώ ο δέκτης εκτελεί την αντίστοιχη μετα-επεξεργασία για την όσο το δυνατόν ακριβέστερη ανάκτηση των μεταδιδόμενων πληροφοριών. Μέσα σε αυτό το ευρύ πεδίο, η Ψηφιακή Επεξεργασία Σημάτων (ΨΕΣ) έχει αναδειχθεί ως μια ευρέως χρησιμοποιούμενη και καλά εδραιωμένη προσέγγιση.

Σύμφωνα με τους Oppenheim et al. [87], «ο όρος σήμα χρησιμοποιείται γενικά για να περιγράψει κάτι που μεταφέρει πληροφορία». Ουσιαστικά, τα σήματα κωδικοποιούν δεδομένα που αφορούν τη δυναμική, την κατάσταση ή τη συμπεριφορά φυσικών συστημάτων. Μπορούν να παραχθούν σκόπιμα για τη μετάδοση πληροφορίας, επιτρέποντας την ανθρώπινη επικοινωνία, αλληλεπίδραση σε αυτοματοποιημένα συστήματα ή διεπαφές ανθρώπου—μηχανής, ενώ παράλληλα παρέχουν ουσιώδη δεδομένα για την παρατήρηση, τον έλεγχο και τη λήψη αποφάσεων, τόσο σε τεχνητά όσο και σε φυσικά περιβάλλοντα. Τα σήματα συνεχούς χρόνου, γνωστά και ως αναλογικά, ορίζονται σε ένα συνεχές εύρος χρόνου, δηλαδή η ανεξάρτητη μεταβλητή τους μεταβάλλεται συνεχώς. Αντίθετα, τα σήματα διακριτού χρόνου ορίζονται μόνο σε συγκεκριμένες χρονικές στιγμές, οπότε η ανεξάρτητη μεταβλητή τους λαμβάνει διακριτές τιμές· μαθηματικά, αναπαρίστανται ως ακολουθίες αριθμών. Το πλάτος ενός σήματος μπορεί επίσης να είναι είτε συνεχές είτε διακριτό. Στην περίπτωση της ταυτόχρονης διακριτοποίησης του χρόνου και του πλάτους, τα προκύπτοντα σήματα ταξινομούνται ως ψηφιακά σήματα.

Σε πολλές πρακτικές εφαρμογές, τα σήματα προέρχονται από φυσικές πηγές. Μια ιδιαίτερη υποκατηγορία τέτοιων σημάτων είναι τα βιοσήματα. Τα βιοσήματα [82] είναι μετρήσιμα σήματα που προέρχονται από βιολογικά συστήματα και μεταφέρουν πληροφορίες σχετικά με φυσιολογικές διεργασίες και λειτουργίες. Μπορούν να ταξινομηθούν σε δύο κύριες κατηγορίες: ηλεκτρικά και μη ηλεκτρικά σήματα.

Ανάλυση Fourier

Στην ανάλυση σημάτων, μια συνάρτηση μπορεί να ερμηνευθεί ως στοιχείο ενός διανυσματικού χώρου, όπου διαφορετικές συναρτήσεις βάσης επιτρέπουν εναλλακτικές αναπαραστάσεις. Ο Μετασχηματισμός Fourier παρέχει την πιο ευρέως χρησιμοποιούμενη αποσύνθεση, εκφράζοντας ένα σήμα συνεχούς χρόνου x(t) ως υπέρθεση μιγαδικών εκθετικών συναρτήσεων:

$$X(\omega) = \int_{-\infty}^{\infty} x(t) e^{-j\omega t} dt, \quad x(t) = \frac{1}{2\pi} \int_{-\infty}^{\infty} X(\omega) e^{j\omega t} d\omega$$

Στην πράξη, τα σήματα είναι συνήθως διακριτά και πεπερασμένου μήκους. Σε αυτήν την περίπτωση, χρησιμοποιείται ο Διακριτός Μετασχηματισμός Fourier, ο οποίος αντιστοιχίζει μια ακολουθία N δειγμάτων x[n] στους φασματικούς της συντελεστές:

$$X[k] = \sum_{n=0}^{N-1} x[n] e^{-j\frac{2\pi}{N}kn}, \quad k = 0, 1, \dots, N-1$$

Ο υπολογισμός του Δ ιαχριτού Μετασχηματισμού Fourier πραγματοποιείται συνήθως με τη χρήση του Γρήγορου Μετασχηματισμού Fourier (FFT) [27], ενός αλγορίθμου που μειώνει την υπολογιστική πολυπλοκότητα από $O(N^2)$ σε $O(N\log N)$.

Ενέργεια και Ισχύς Σήματος

Στην επεξεργασία σημάτων, η ενέργεια E, η στιγμιαία ισχύς P(t) και η μέση ισχύς P ενός σήματος συνεχούς χρόνου x(t) ορίζονται ως:

$$E = \int_{-\infty}^{\infty} |x(t)|^2 dt$$
, $P(t) = |x(t)|^2$, $P = \lim_{T \to \infty} \frac{1}{2T} \int_{-T}^{T} |x(t)|^2 dt$

Για ένα σήμα διαχριτού χρόνου x[n], οι ορισμοί είναι ανάλογοι:

$$E = \sum_{n = -\infty}^{\infty} |x[n]|^2, \quad p[n] = |x[n]|^2, \quad P = \lim_{N \to \infty} \frac{1}{2N + 1} \sum_{n = -N}^{N} |x[n]|^2$$

Πέρα από τους ορισμούς στο πεδίο του χρόνου, η ενέργεια ενός σήματος μπορεί επίσης να εκφραστεί στο πεδίο της συχνότητας. Αυτή η σχέση καθορίζεται από το Θεώρημα του Parseval, το οποίο δηλώνει ότι η συνολική ενέργεια ενός σήματος στο πεδίο του χρόνου είναι ίση με τη συνολική του ενέργεια στο πεδίο της συχνότητας. Για ένα σήμα συνεχούς και διακριτού χρόνου με μετασχηματισμό Fourier $X(\omega)$ και X[k], προκύπτουν αντίστοιχα:

$$\int_{-\infty}^{\infty} |x(t)|^2 dt = \frac{1}{2\pi} \int_{-\infty}^{\infty} |X(\omega)|^2 d\omega, \quad \sum_{n=0}^{N-1} |x[n]|^2 = \frac{1}{N} \sum_{k=0}^{N-1} |X[k]|^2$$

Φασματική Πυκνότητα Ισχύος

Η Φασματική Πυκνότητα Ισχύος περιγράφει το πώς κατανέμεται η ισχύς ενός σήματος ή μιας τυχαίας διαδικασίας στις διάφορες συχνότητες. Αποτελεί μία βασική μετρική στην ανάλυση βιοσημάτων [16], καθώς παρέχει πληροφορία για τα φασματικά χαρακτηριστικά και τη δυναμική του σήματος. Μαθηματικά, ορίζεται ως:

$$S_{xx}(\omega) = \int_{-\infty}^{\infty} R_{xx}(\tau) e^{-j\omega\tau} d\tau,$$

όπου x(t) είναι ένα στάσιμο σήμα και $R_{xx}(\tau)$ είναι η συνάρτηση αυτοσυσχέτισης του σήματος. Η αυτοσυσχέτιση μετρά την ομοιότητα μεταξύ του σήματος και μιας χρονικά μετατοπισμένης εκδοχής του κατά καθυστέρηση τ .

Στην πράξη, ωστόσο, υπολογίζεται συνήθως μέσω του DFT του σήματος:

$$P[k] = \frac{1}{N} |X[k]|^2.$$

Συστοιχία Φίλτρων Gabor

Το φίλτρο Gabor είναι ένα γραμμικό (LTI) φίλτρο, το οποίο σε μία διάσταση, ορίζεται ως:

$$g(t) = \exp\left(-\frac{t^2}{2\sigma^2}\right)\cos(2\pi f_c t + \phi)$$

όπου σ είναι η τυπική απόκλιση του γκαουσιανού περιβλήματος, η οποία ελέγχει την χρονική του διασπορά, f_c είναι η κεντρική συχνότητα του φίλτρου και ϕ είναι η διαφορά φάσης.

Μια συστοιχία φίλτρων Gabor κατασκευάζεται δημιουργώντας μια ακολουθία φίλτρων Gabor, των οποίων οι κεντρικές συχνότητες κατανέμονται μεταξύ μιας κατώτερης (f_{low}) και μιας ανώτερης (f_{high}) συχνότητας αποκοπής. Με αυτόν τον τρόπο, το ευρυζωνικό σήμα αποσυντίθεται σε υποζώνες, με κάθε φίλτρο να αποτυπώνει τοπικό φασματικό περιεχόμενο γύρω από τη δική του κεντρική συχνότητα. Στην υλοποίησή μας, το βήμα συχνότητας ορίζεται ως $\Delta f = \frac{f_{\text{high}} - f_{\text{low}}}{N}$, όπου N είναι ο αριθμός των φίλτρων. Οι κεντρικές συχνότητες ορίζονται ως $f_{\text{c}}(k) = f_{\text{low}} + k\Delta f$, όπου $k \in \mathbb{Z}_{>0}: k < N$.

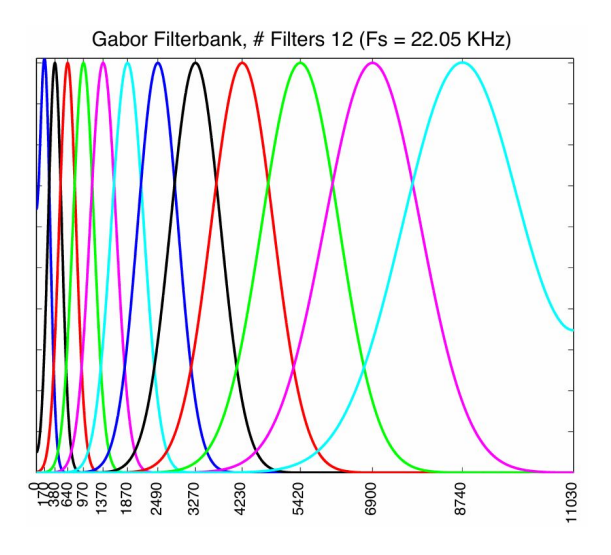


Figure 1 Συστοιχία Φίλτρων Gabor, αποτελούμενη από 12 φίλτρα σε κατανομή Mel με επικάλυψη 50% (Ρυθμός Δειγματοληψίας = 22.05 kHz) [123].

Ανάλυση Ανεξάρτητων Συνιστωσών

Η Ανάλυση Ανεξάρτητων Συνιστωσών [26] είναι είναι μια υπολογιστική μέθοδος για το διαχωρισμό ενός σήματος σε προσθετικές, στατιστικά ανεξάρτητες συνιστώσες. Η μέθοδος αυτή υποθέτει ότι τα παρατηρούμενα σήματα αποτελούν γραμμικούς συνδυασμούς ανεξάρτητων, μη γκαουσιανών πηγών.

Ενεργειακός Τελεστής Teager-Kaiser

Σχεδόν όλα τα συστήματα επικοινωνιών ασχολούνται με ταλαντωτικές συναρτήσεις, που χαρακτηρίζονται από διαμόρφωση πλάτους (AM) και διαμόρφωση συχνότητας (FM). Για την ανίχνευση των διαμορφώσεων σε αυτά τα σήματα AM-FM, μπορεί να χρησιμοποιηθεί ένας μη γραμμικός διαφορικός τελεστής, γνωστός ως Ενεργειακός Τελεστής Teager-Kaiser (TKEO) ([54], [74]), ο οποίος εκτιμά το γινόμενο του χρονικά μεταβαλλόμενου πλάτους και της συχνότητας του σήματος. Ο ΤΚΕΟ έχει αναπτυχθεί τόσο για σήματα συνεχούς χρόνου (Ψ_c) , όσο και για σήματα διακριτού χρόνου (Ψ_d) και λειτουργεί ως «ανιχνευτής ενέργειας», επιτρέποντας τη μοντελοποίηση των χρονικών μεταβολών της ενέργειας ενός σήματος.

$$\Psi_c[x(t)] = (\dot{x}(t))^2 - x(t)\ddot{x}(t)$$

$$\Psi_d[x[n]] = x^2[n] - x[n-1]x[n+1]$$

Όπως εξήγησε ο Kaiser [54], στην απλή αρμονική ταλάντωση, η ενέργεια του σήματος θεωρείται ότι είναι ανάλογη του τετραγώνου του πλάτους και της συχνότητας:

$$E = \frac{1}{2}m\omega^2 A^2 \propto \omega^2 A^2$$

Παρά αυτή τη θεμελιώδη σχέση, προηγούμενες μεθοδολογίες υπολογισμού ενέργειας συχνά παραμελούσαν τη συνιστώσα της συχνότητας, εστιάζοντας αποχλειστιχά στον παράγοντα του πλάτους. Για ένα απλό ταλαντωτιχό σήμα $x[n]=A\cos(\Omega n+\phi)$, ο Kaiser έδειξε ότι:

$$x^{2}[n] - x[n+1]x[n-1] = A^{2}\sin^{2}(\Omega) \approx A^{2}\Omega^{2},$$

για μικρές τιμές της Ω . Για να διασφαλιστεί η ακρίβεια αυτής της προσέγγισης εντός αποδεκτών ορίων, ο Kaiser προτείνει τον περιορισμό της τιμής της Ω στο διάστημα $[0,\frac{\pi}{4}]$, ώστε να διατηρείται το σχετικό σφάλμα κάτω από 11%. Επομένως, για να θεωρηθεί αυτός ο τελεστής αξιόπιστο μέτρο ενέργειας, απαιτείται η δειγματοληψία τουλάχιστον δύο σημείων ανά τέταρτο της περιόδου της ημιτονοειδούς ταλάντωσης.

Αλγόριθμος Διαχωρισμού Ενέργειας

Για την εξαγωγή του περιβλήματος πλάτους και της στιγμιαίας συχνότητας σημάτων ΑΜ-FM, αναπτύχθηκε ο Αλγόριθμος Διαχωρισμού Ενέργειας (ESA) [74]. Ο ESA χρησιμοποιεί μη γραμμικούς συνδυασμούς στιγμιαίων εξόδων του τελεστή ενέργειας, ώστε να διαχωρίζει τις συνιστώσες διαμόρφωσης πλάτους και διαμόρφωσης συχνότητας εντός του γινομένου ενέργειας που παράγει.

CESA

Ο Συνεχής Αλγόριθμος Διαχωρισμού Ενέργειας (CESA) εισήχθη για σήματα συνεχούς χρόνου. Ο CESA παρέχει εκτιμήσεις της χρονικά μεταβαλλόμενης στιγμιαίας συχνότητας $\omega_i(t) \geq 0$ και του περιβλήματος πλάτους |a(t)| ως εξής:

$$\omega_i(t) = \sqrt{\frac{\Psi[\dot{x}(t)]}{\Psi[x(t)]}}$$

$$|a(t)| = \frac{\Psi[x(t)]}{\sqrt{\Psi[\dot{x}(t)]}}$$

DESA

Ο Διαχριτός Αλγόριθμος Διαχωρισμού Ενέργειας (DESA) αναπτύχθηκε για σήματα διαχριτού χρόνου, για τον οποίον έχουν προταθεί οι εξής τρεις παραλλαγές: DESA-1a, DESA-1 και DESA-2. Όπως αναφέρεται στο [74], ο DESA-2 είναι ο ταχύτερος μεταξύ των τριών και η μαθηματική του ανάλυση είναι η πιο απλή. Ο DESA-1a εμφανίζει χαμηλότερη απόδοση, ενώ ο DESA-1 επιτυγχάνει ελαφρώς καλύτερη απόδοση από τον DESA-2, με τη διαφορά να κυμαίνεται μεταξύ 0.01% και 0.1%. Παρακάτω παρουσιάζονται οι εξισώσεις κάθε αλγορίθμου, όπου η περιβάλλουσα πλάτους δηλώνεται ως |a[n]| και η στιγμιαία συχνότητα ως Ω_i .

DESA-1a Ο δείχτης '1' υποδηλώνει την προσέγγιση παραγώγων με διαφορά ενός δείγματος, ενώ το γράμμα 'a' αναφέρεται στη χρήση ασύμμετρης διαφοράς.

$$\Omega_i[n] \approx \arccos\left(1 - \frac{\Psi[x[n] - x[n-1]]}{2\Psi[x[n]]}\right)$$

$$|a[n]| \approx \sqrt{\frac{\Psi[x[n]]}{1 - \left[1 - \frac{\Psi[x[n] - x[n-1]]}{2\Psi[x[n]]}\right]^2}}$$

 ${f DESA-1}$ Η επίδραση του Ψ στις ασύμμετρες παραγώγους εξισορροπείται μερικώς με τη μέση τιμή δύο αντίθετων ασύμμετρων διαφορών, οδηγώντας σε μια μερική «συμμετριοποίηση».

$$y[n] = x[n] - x[n-1]$$

$$\Omega_i[n] \approx \arccos\left(1 - \frac{\Psi[y[n] + y[n+1]]}{4\Psi[x[n]]}\right)$$

$$|a[n]| pprox \sqrt{\frac{\Psi[x[n]]}{1 - \left[1 - \frac{\Psi[y[n] + y[n+1]]}{4\Psi[x[n]]}\right]^2}}$$

Η ορθή εκτίμηση συχνότητας προϋποθέτει τον περιορισμό $0<\Omega_i[n]<\pi$, καθώς το εύρος κύριας τιμής της συνάρτησης $\arccos(v)$ ορίζεται για $v\in[0,\pi]$. Κατά συνέπεια, ο DESA-1 μπορεί να εκτιμήσει στιγμιαίες συχνότητες έως και $\frac{1}{2}$ φορές τον ρυθμό δειγματοληψίας.

 ${f DESA-2}$ Ο αλγόριθμος αυτός χρησιμοποιεί συμμετρικές διαφορές. Ο δείκτης '2' υποδηλώνει την προσέγγιση των πρώτων παραγώγων μέσω διαφορών μεταξύ δειγμάτων με χρονικούς δείκτες που διαφέρουν κατά 2.

$$\Omega_i[n] \approx \frac{1}{2} \arccos \left(1 - \frac{\Psi[x[n+1] - x[n-1]]}{2\Psi[x[n]]} \right)$$

$$|a[n]| \approx \frac{2\Psi[x[n]]}{\sqrt{\Psi[x[n+1] - x[n-1]]}}$$

Εδώ, η ορθή εκτίμηση συχνότητας προϋποθέτει ότι $0 < \Omega_i[n] < \frac{\pi}{2}$.

Συστοιχίες Φίλτρων Gabor στον ΤΚΕΟ

Ο ΤΚΕΟ παρέχει αξιόπιστες εκτιμήσεις στιγμιαίας ενέργειας κυρίως όταν εφαρμόζεται σε σήματα στενής ζώνης [74]. Για την ικανοποίηση αυτής της προϋπόθεσης, η χρήση συστοιχίας φίλτρων βοηθά στη διάσπαση του ευρυζωνικού σήματος σε τοπικές υποζώνες συχνοτήτων, γεγονός που οδηγεί σε ομαλότερες διαμορφώσεις στιγμιαίου πλάτους και συχνότητας [34]. Για την υλοποίηση της συστοιχίας, καταλληλότερα κρίνονται τα φίλτρα Gabor, καθώς συνδυάζουν καλή χρονική και φασματική ανάλυση [74].

Όπως περιγράφηκε προηγουμένως, η συστοιχία φίλτρων Gabor κατασκευάζεται με τον ορισμό μιας ακολουθίας φίλτρων με κεντρικές συχνότητες μεταξύ των κατώτερων και ανώτερων ορίων αποκοπής. Στην παρούσα Εργασία, επιλέγονται κεντρικές συχνότητες ομοιόμορφα κατανεμημένες. Αφού καθοριστεί το σύνολο των κεντρικών συχνοτήτων f_c , κάθε σήμα διέρχεται από τα αντίστοιχα φίλτρα Gabor και εφαρμόζεται ο τελεστής ΤΚΕΟ στην έξοδο κάθε φίλτρου. Αυτό έχει ως αποτέλεσμα την παραγωγή N σημάτων ενέργειας, ένα για κάθε υποζώνη. Για κάθε σήμα ΤΚΕΟ, υπολογίζεται ο χρονικός μέσος ως μέτρο της μέσης ενέργειας υποζώνης. Η συστοιχία φίλτρων που αποδίδει τη μέγιστη μέση τιμή ΤΚΕΟ επιλέγεται, και το αντίστοιχο φιλτραρισμένο σήμα διατηρείται για περαιτέρω ανάλυση, καθώς αντιπροσωπεύει την υποζώνη, όπου ο ΤΚΕΟ παρέχει την περιγραφή της δυναμικής του σήματος με την περισσότερη πληροφορία.

Μοντέλα Μηχανικής Μάθησης

Μηχανές Διανυσμάτων Υποστήριξης (SVMs) [28]: Πρόκειται για μοντέλα επιβλεπόμενης μάθησης σχεδιασμένα για δυαδική ταξινόμηση και ενσωματώνουν μια απλή αλλά ισχυρή αρχή: αντί να αναζητούν απλώς οποιοδήποτε όριο απόφασης που διαχωρίζει τις κλάσεις, επιδιώκουν το βέλτιστο όριο. Το βέλτιστο υπερεπίπεδο ορίζεται ως εκείνο που διαχωρίζει τα δεδομένα εκπαίδευσης με το μέγιστο δυνατό περιθώριο, δηλαδή τη μέγιστη απόσταση μεταξύ του ορίου και των πλησιέστερων σημείων δεδομένων από κάθε κλάση.

Δέντρα Απόφασης και Τυχαίο Δάσος [18]: Τα Δέντρα Απόφασης αποτελούν μοντέλα επιβλεπόμενης μάθησης που χωρίζουν τον χώρο εισόδων σε περιοχές που αντιστοιχούν σε ετικέτες κλάσεων (στην περίπτωση ταξινόμησης) ή σε αριθμητικές τιμές (στην περίπτωση παλινδρόμησης). Ένα δέντρο κατασκευάζεται μέσω επαναληπτικών διαχωρισμών των δεδομένων εκπαίδευσης με βάση τις τιμές των χαρακτηριστικών. Σε κάθε εσωτερικό κόμβο, επιλέγεται ένα χαρακτηριστικό και ένα κατώφλι διαχωρισμού, έτσι ώστε να μεγιστοποιείται κάποια κατάλληλα επιλεγμένη μετρική, όπως το πληροφοριακό κέρδος. Η διαδικασία συνεχίζεται, έως ότου ικανοποιηθούν τα κριτήρια τερματισμού, όπως η επίτευξη μέγιστου βάθους ή ο μικρός αριθμός δειγμάτων που δεν επιτρέπει περαιτέρω διαχωρισμό. Οι τελικοί κόμβοι (φύλλα) αποδίδουν τις προβλέψεις. Η μέθοδος Τυχαίου Δάσους αποτελεί μια επέκταση των Δέντρων Απόφασης, όπου πολλαπλά δέντρα εκπαιδεύονται σε τυχαία υποσύνολα των δεδομένων και των χαρακτηριστικών. Η τελική πρόβλεψη προκύπτει μέσω ψηφοφορίας (στην ταξινόμηση) ή μέσω μέσου όρου (στην παλινδρόμηση), γεγονός που βελτιώνει τη γενίκευση και μειώνει τον κίνδυνο υπερεκπαίδευσης.

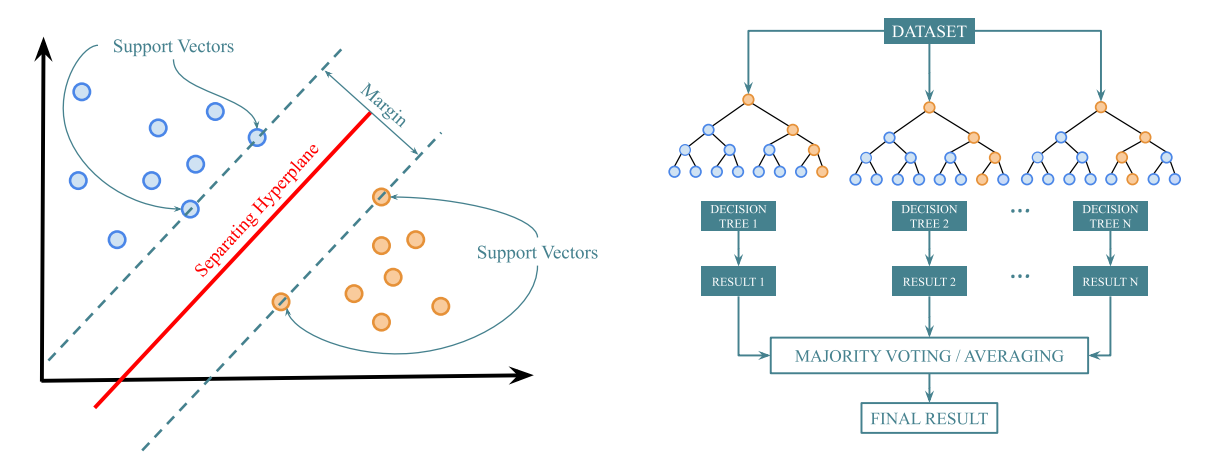


Figure 2.1 Γραμμικός SVM.

Figure 2.2 Τυχαίο Δ άσος με N Δ έντρα.

Εφαρμογή ΤΚΕΟ Σε ΗΕΓ

Προεπεξεργασία Σημάτων

Στην παρούσα εργασία χρησιμοποιούμε τέσσερα σύνολα δεδομένων, πληροφορίες για τα οποία παρέχουμε στα αντίστοιχα Παραρτήματα. Τα ΗΕΓ από τα σύνολα δεδομένων DEAP και SEED παρέχονται ήδη σε προεπεξεργασμένη μορφή. Αντίθετα, τα σύνολα δεδομένων BCI-IV 2a και TUEP, που είναι διαθέσιμα σε ακατέργαστη μορφή, απαιτούν επιπλέον στάδια προεπεξεργασίας. Για τα δύο τελευταία σύνολα δεδομένων, εφαρμόστηκε μια παρόμοια διαδικασία, η οποία περιλαμβάνει εφαρμογή Ανάλυσης Ανεξάρτητων Συνιστωσών για την αφαίρεση θορύβου, αξιοποιώντας τα διαθέσιμα ηλεκτροκαρδιογραφήματα στο TUEP και τα διαθέσιμα ηλεκτροοφθαλμογραφήματα στο BCI-IV 2a. Στη συνέχεια, εφαρμόστηκε φίλτρο αποκοπής ζώνης στα 60 Hz για το TUEP και στα 50 Hz για το BCI-IV 2a, προκειμένου να εξαλειφθεί ο θόρυβος δικτύου. Τέλος, όλα τα σήματα πέρασαν από υψιπερατό φίλτρο με συχνότητα αποκοπής 0.5 Hz.

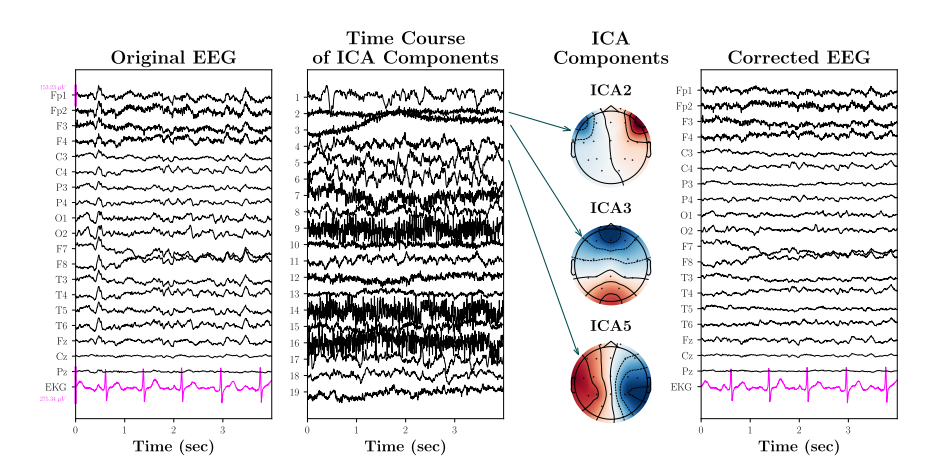


Figure 3 Εφαρμογή Ανάλυσης Ανεξάρτητων Συνιστωσών σε ΗΕΓ από το Σύνολο Δεδομένων TUEP.

Όλα τα αρχεία ΗΕΓ χωρίστηκαν σε επικαλυπτόμενα τμήματα, με τα μήκη παραθύρου και τα ποσοστά επικάλυψης να επιλέγονται ανάλογα με τα ιδιαίτερα χαρακτηριστικά κάθε συνόλου δεδομένων. Η προσέγγιση αυτή επιτρέπει την εξαγωγή χρονικά τοπικών χαρακτηριστικών, διατηρώντας παράλληλα τη συγκρισιμότητα μεταξύ διαφορετικών καταγραφών. Για την αξιολόγηση της επίδρασης της χρονικής ανάλυσης στην ανάλυση που βασίζεται στον τελεστή Teager-Kaiser ενέργειας (ΤΚΕΟ), οι καταγραφές 60 δευτερολέπτων του DEAP χωρίστηκαν σε παράθυρα διάρκειας 20 δευτερολέπτων με 50% επικάλυψη, αποδίδοντας 5 παράθυρα ανά δείγμα. Αντίστοιχα, οι καταγραφές του SEED, διάρκειας περίπου 4 λεπτών η καθεμία, χωρίστηκαν σε παράθυρα 20 δευτερολέπτων με 50% επικάλυψη, παράγοντας 23 τμήματα ανά καταγραφή. Τα

Dataset	Window (s)	Overlap (%)	# Filters
SEED	20	50	12, 25, 50
DEAP	20	50	12, 25, 50
BCI-IV 2a	4	0	12, 25, 50
TUEP	10	0	12

Table 1 Παράμετροι Προεπεξεργασίας σε κάθε Σύνολο Δεδομένων.

δείγματα του TUEP τμηματοποιήθηκαν σε παράθυρα 10 δευτερολέπτων χωρίς επικάλυψη, λόγω υπολολιστικών περιορισμών. Ο αριθμός των παραθύρων ανά δείγμα διαφοροποιήθηκε ανάλογα με τη διάρκεια της καταγραφής (από περίπου 1 λεπτό έως 1 ώρα), με αποτέλεσμα να κυμαίνεται μεταξύ 11 και 719 παραθύρων ανά δείγμα. Για το σύνολο δεδομένων BCI-IV 2a, κάθε καταγραφή αντιστοιχεί σε μία συνεχή συνεδρία για κάθε συμμετέχοντα, η οποία περιλαμβάνει τόσο περιόδους παρουσίασης ερεθισμάτων όσο και διαστήματα μεταξύ δοκιμών. Δεδομένου ότι παρέχονται ακριβείς χρονικές σημάνσεις για την έναρξη κάθε ερεθίσματος, εξήχθησαν τμήματα σταθερού μήκους 4 δευτερολέπτων μετά από κάθε παρουσίαση ερεθίσματος. Η διαδικασία αυτή παρήγαγε 288 παράθυρα κινητικής φαντασίας ανά καταγραφή.

Πριν από την εξαγωγή ΤΚΕΟ χαρακτηριστικών, κάθε τμήμα ΕΕG αποσυντέθηκε σε πέντε πιο στενές ζώνες συχνοτήτων μέσω ζωνοπερατού φιλτραρίσματος, που αντιστοιχούν στις κανονικές ζώνες ΕΕG. Στη συνέχεια εφαρμόστηκαν πολλαπλές διατάξεις φίλτρων (12, 25 και 50 φίλτρα) εντός του εύρους συχνοτήτων κάθε κανονικής ζώνης στα σύνολα δεδομένων DEAP, SEED και BCI-IV 2a, με σκοπό τη συστηματική αξιολόγηση της επίδρασης της ανάλυσης του φίλτρου στα εξαγόμενα χαρακτηριστικά. Αντίθετα, στο σύνολο δεδομένων TUEP εφαρμόστηκαν μόνο 12 φίλτρα, λόγω υπολογιστικών περιορισμών. Οι παράμετροι προεπεξεργασίας που μόλις αναλύθηκαν συνοψίζονται στον Πίνακα 1.

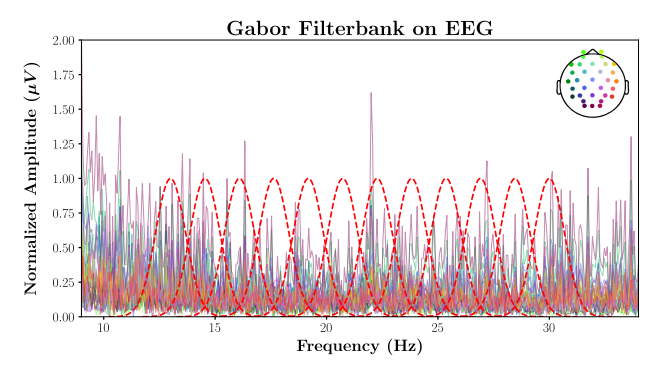


Figure 4 Εφαρμογή Συστοιχίας Φίλτρων Gabor με 12 Φίλτρα στα Κανάλια από ένα ΗΕΓ του Συνόλου Δεδομένων DEAP στην Beta Μπάντα.

Εξαγωγή Χαρακτηριστικών

Χαρακτηριστικά ΤΚΕΟ

Εξάγουμε ΤΚΕΟ χαρακτηριστικά από τα σήματα ΗΕΓ, με σκοπό την απόκτηση πολύτιμων πληροφοριών. Κάθε χαρακτηριστικό υπολογίζεται ανεξάρτητα για κάθε κανάλι ΗΕΓ και για κάθε ζώνη συχνοτήτων, με αποτέλεσμα ένα διάνυσμα χαρακτηριστικών μεγέθους (μπάντες × κανάλια × χαρακτηριστικά) για κάθε δείγμα. Τα ΤΚΕΟ χαρακτηριστικά, που προτείνονται στην παρούσα εργασία, ομαδοποιούνται σε τρεις κατηγορίες: στατιστικά χαρακτηριστικά, χαρακτηριστικά σχετικής ενέργειας και χαρακτηριστικά βασισμένα στον Αλγόριθμο Διαχωρισμού Ενέργειας. Από εδώ και στο εξής, θεωρούμε $\Psi \equiv \Psi_d$.

Στατιστικά Χαρακτηριστικά

Έστω ότι s σήμα που αντιστοιχεί σε ένα συγκεκριμένο ζεύγος καναλιού–ζώνης, αποτελούμενο από N δείγματα, και s_i το i-στο δείγμα του. Υπολογίζουμε τα εξής:

• Μέση Teager-Kaiser ενέργεια:

$$\mu_{\Psi}(s) = \frac{1}{N} \sum_{i=1}^{N} \Psi(s_i)$$

• Διακύμανση της Teager–Kaiser ενέργειας:

$$v-\Psi(s) = \frac{1}{N} \sum_{i=1}^{N} (\Psi(s_i) - \mu_{\Psi}(s))^2$$

• Απόλυτη διαφορά μεταξύ της μέγιστης και της ελάχιστης Teager-Kaiser ενέργειας:

$$\text{Max-Min}_{\Psi}(s) = \max_{i \in [1,N]} \{ \Psi(s_i) \} - \min_{i \in [1,N]} \{ \Psi(s_i) \}$$

• Ασυμμετρία της Teager-Kaiser ενέργειας:

$$s-\Psi(s) = \frac{\frac{1}{N} \sum_{i=1}^{N} (\Psi(s_i) - \mu_{\Psi}(s))^3}{\left(\frac{1}{N} \sum_{i=1}^{N} (\Psi(s_i) - \mu_{\Psi}(s))^2\right)^{3/2}}$$

• Κύρτωση της Teager–Kaiser ενέργειας:

$$k-\Psi(s) = \frac{\frac{1}{N} \sum_{i=1}^{N} (\Psi(s_i) - \mu_{\Psi}(s))^4}{\left(\frac{1}{N} \sum_{i=1}^{N} (\Psi(s_i) - \mu_{\Psi}(s))^2\right)^2} - 3$$

• Δείκτης μέγιστης Teager-Kaiser ενέργειας:

$$i_{\Psi_{\max}}(s) = \underset{i \in [1, N]}{\operatorname{arg}} \max \{ \Psi(s_i) \}$$

• Απόλυτη διαφορά μεταξύ των δεικτών μέγιστης και ελάχιστης Teager-Kaiser ενέργειας:

$$i_{\Psi_{\max-\min}}(s) = |\arg\max_{i \in [1,N]} {\{\Psi(s_i)\}} - \arg\min_{i \in [1,N]} {\{\Psi(s_i)\}}|$$

Χαρακτηριστικά Σχετικής Ενέργειας

Για ένα σήμα συγκεκριμένης μπάντας s, η σχετική συνεισφορά της Teager–Kaiser ενέργειας σε σχέση με όλες τις υπό εξέταση μπάντες συχνοτήτων ορίζεται ως:

$$RE_{band}(s) = \frac{\Psi_{band}(s)}{\sum_{k} \Psi_{k}(s)}$$

όπου $k \in \{ \text{Delta}, \text{Theta}, \text{Alpha}, \text{Beta}, \text{Gamma} \}$. Στη συνέχεια, υπολογίζονται τα ακόλουθα στατιστικά της σχετικής ενέργειας ως χαρακτηριστικά:

• Μέση σχετική ενέργεια:

$$\text{m-RE}_{\text{band}}(s) = \frac{1}{N} \sum_{i=1}^{N} \text{RE}_{\text{band}}(s_i)$$

• Διακύμανση της σχετικής ενέργειας:

$$v-RE_{band}(s) = \frac{1}{N} \sum_{i=1}^{N} (RE_{band}(s_i) - m-RE_{band}(s))^2$$

• Απόλυτη διαφορά μεταξύ μέγιστης και ελάχιστης σχετικής ενέργειας:

$$\operatorname{Max-Min}_{\operatorname{RE}}(s) = \max_{i \in [1,N]} \{\operatorname{RE}_{\operatorname{band}}(s_i)\} - \min_{i \in [1,N]} \{\operatorname{RE}_{\operatorname{band}}(s_i)\}$$

• Δείκτης μέγιστης σχετικής ενέργειας:

$$i_{\text{RE}_{\text{max}}}(s) = \underset{i \in [1,N]}{\operatorname{arg max}} \{ \text{RE}_{\text{band}}(s_i) \}$$

 Απόλυτη διαφορά μεταξύ των δεικτών μέγιστης και ελάχιστης σχετικής ενέργειας:

$$i_{\text{RE}_{\text{max-min}}}(s) = |\underset{i \in [1,N]}{\arg \max} \{ \text{RE}_{\text{band}}(s_i) \} - \underset{i \in [1,N]}{\arg \min} \{ \text{RE}_{\text{band}}(s_i) \} |$$

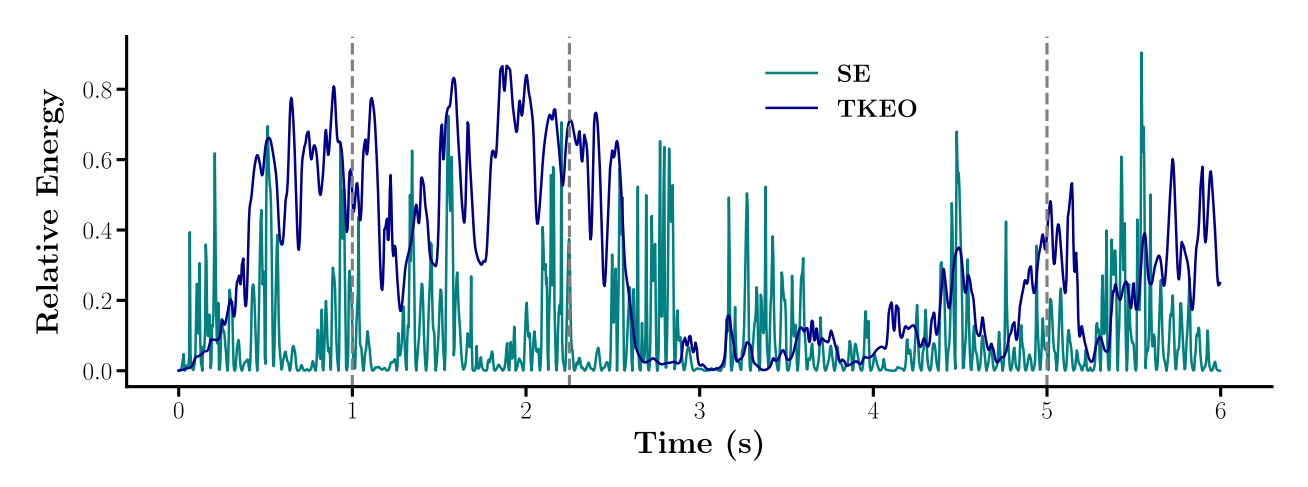


Figure 5 Σχετικές τετραγωνικές και Teager–Kaiser ενέργειες του καναλιού FC4 από το σύνολο δεδομένων BCI-IV 2a στη ζώνη Alpha. Οι γκρι διακεκομμένες κάθετες γραμμές αντιστοιχούν στην έναρξη του ερεθίσματος (1s), στη λήξη του ερεθίσματος (2.25s) και στη λήξη της φάσης κινητικής νοερής απεικόνισης (5s). Η σχετική ενέργεια ΤΚΕΟ παρουσιάζει λιγότερες διακυμάνσεις εντός κάθε περιόδου, παραμένοντας χαμηλή κατά τη διάρκεια της κινητικής νοερής απεικόνισης (MI) και υψηλότερη κατά τις περιόδους ηρεμίας, υποδεικνύοντας ότι η σχετική ενέργεια ΤΚΕΟ προσφέρει μια πιο ομαλή και διακριτική αναπαράσταση για την MI.

Χαρακτηριστικά Αλγορίθμου Διαχωρισμού Ενέργειας

Στην παρούσα εργασία, υιοθετούμε τον αλγόριθμο DESA-1 για την εξαγωγή της στιγμιαίας διαμόρφωσης πλάτους (a(s)) και της στιγμιαίας διαμόρφωσης συχνότητας $(\Omega(s))$. Ακολούθως, υπολογίζονται τα χαρακτηριστικά που βασίζονται στον DESA:

• Μέση τιμή στιγμιαίας διαμόρφωσης πλάτους [124]:

$$\text{m-IAM}(s) = \frac{1}{N} \sum_{i=1}^{N} |a(s_i)|$$

• Σταθμισμένος μέσος όρος στιγμιαίας διαμόρφωσης συχνότητας [124]:

$$\text{m-IFM}(s) = \frac{\sum_{i=1}^{N} \Omega(s_i) \cdot \left(\text{m-IAM}(s_i)\right)^2}{\sum_{i=1}^{N} \left(\text{m-IAM}(s_i)\right)^2}$$

• Διακύμανση της στιγμιαίας διαμόρφωσης συχνότητας:

v-IFM(s) =
$$\frac{1}{N} \sum_{i=1}^{N} (\Omega(s_i) - \mu_{\Omega}(s))^2$$
,

όπου
$$\mu_{\Omega}(s) = \frac{1}{N} \sum_{i=1}^{N} \Omega(s_i)$$
.

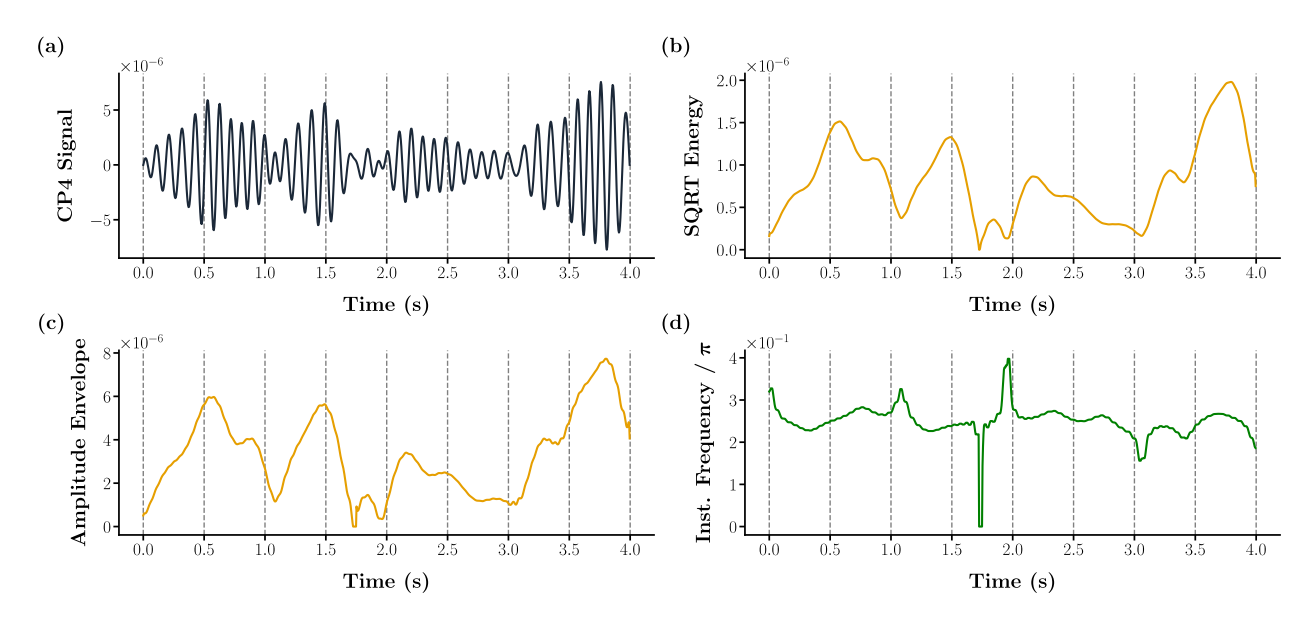


Figure 6 (a) Σήμα καναλιού CP4 από το σύνολο δεδομένων BCI-IV 2a στη ζώνη Alpha. (b) Τετραγωνική ρίζα του ΤΚΕΟ. (c) Εκτιμώμενη περιβάλλουσα πλάτους με χρήση του DESA-1. (d) Εκτιμώμενη στιγμιαία συχνότητα με χρήση του DESA-1, εκφρασμένη ως κλάσμα του π.

Μέθοδοι Αναφοράς και Επιλογή Χαρακτηριστικών ΤΚΕΟ

Αποσκοπώντας στην αξιολόγηση των ΤΚΕΟ χαρακτηριστικών και στην εκτίμηση της ενδεχόμενης συμπληρωματικότητάς τους με καθιερωμένα χαρακτηριστικά των ΗΕΓ, υπολογίζουμε τα παρακάτω μεθόδων αναφοράς:

- Φασματική Πυκνότητα Ισχύος (PSD), χρησιμοποιώντας τη μέθοδο Welch, παράγωντας $\frac{f_s}{2}$ χαρακτηριστικά, όπου f_s η συχνότητα δειγματοληψίας.
- Ενέργεια Σήματος (SE), το οποίο χαρακτηριστικό περιέχει τη μέση τιμή του τετραγώνου ενέργειας/στιγμιαίας ισχύος σήματος και τη μέση τιμή της σχετικής ενέργειας σήματος, κατ'αναλογία με τα χαρακτηριστικά ΤΚΕΟ.

Οι ζώνες συχνοτήτων εξήχθησαν από τις μεθόδους αναφοράς χρησιμοποιώντας ένα τυπικό ζωνοπερατό φίλτρο Butterworth 10ης τάξης.

Στο πειραματικό μας πλαίσιο, αρχικά αξιολογήσαμε την απόδοση του μοντέλου χρησιμοποιώντας το πλήρες σύνολο των 15 εξαγόμενων χαρακτηριστικών. Για να διερευνήσουμε περαιτέρω τη σχετική συνεισφορά των επιμέρους περιγραφικών μεγεθών, εξετάσαμε επίσης διαφορετικά υποσύνολα χαρακτηριστικών και αξιολογήσαμε την αποτελεσματικότητά τους μέσω συστηματικών δοκιμών. Με βάση τα αποτελέσματα αυτών των αξιολογήσεων, παρατηρήθηκε ότι ένα συγκεκριμένο υποσύνολο, αποτελούμενο από τα mean Teager-Kaiser energy (m-TKEO), mean Relative Energy (m-RE), mean Instantaneous Amplitude Modulation (m-IAM) και variance of Instantaneous Frequency Modulation (v-IFM), παρήγαγε σταθερά ανώτερη απόδοση ταξινόμησης σε σχέση με το άλλα υποσύνολα χαρακτηριστικών.

Για λόγους σαφήνειας στις επόμενες ενότητες, ορίζουμε την ορολογία ως εξής: το πλήρες σύνολο των 15 χαραχτηριστιχών αναφέρεται ως τα χαραχτηριστιχά "TKEO", ενώ το μειωμένο υποσύνολο των τεσσάρων βέλτιστων περιγραφιχών μεγεθών (m-TKEO, m-RE, m-IAM και v-IFM) χαραχτηρίζεται ως τα χαραχτηριστιχά " $Selected\ TKEO$ ". Αυτή η διάχριση μας επιτρέπει να συγκρίνουμε ρητά την επίδραση της μείωσης της διαστατιχότητας των χαραχτηριστιχών στα αποτελέσματα ταξινόμησης που παρουσιάζονται στα επόμενα χεφάλαια. Επιπλέον, ορίζουμε τον όρο "Combined" χαραχτηριστιχά ως το σύνολο που προχύπτει από τη συνένωση των χαραχτηριστιχών $Selected\ TKEO$, του PSD, της μέσης ενέργειας του σήματος και της μέσης σχετιχής ενέργειας του σήματος.

Αξιολόγηση

Υπολογίζουμε τα ΤΚΕΟ χαρακτηριστικά σε τρία προβλήματα: Αναγνώριση Συναισθήματος, Ταξινόμηση Κινητικής Νοερής Απεικόνισης και Εντοπισμό Επιληψίας. Πραγματοποιούμε πειράματα στον κάθε συμμετέχοντα ξεχωριστά (Subject-Dependent) και σε όλους τους συμμετέχοντες από κοινού (Subject-Independent). Ενοποιούμε τα ΗΕΓ κανάλια, αφού γίνει εξαγωγή των χαρακτηριστικών, και εφαρμόζουμε μη γραμμική Μηχανή Διανυσμάτων Υποστήριξης για τα Subject-Dependent πειράματα, ενώ επιλέγουμε ταξινόμηση με Τυχαίο Δάσος 100 Δέντρων Αποφάσεως για τα Subject-Independent πειράματα, λόγω του χαμηλού υπολογιστικού κόστους του αλγορίθμου. Ταξινομούμε το κάθε δείγμα σε μία μόνο κλάση. Συγκεκριμένα: (1) υψηλής ή χαμηλής ευχαρίστησης (valence) και διέγερσης (arousal) στο σύνολο δεδομένων DEAP, με καθορισμό κλάσεων βάσει της διαμέσου, (2) θετικό, ουδέτερο ή αρνητικό συναίσθημα στο SEED, (3) ύπαρξη επιληψίας έναντι μη ύπαρξης στο TUEP και (4) νοερή κινητική απεικόνιση αριστερού χεριού, δεξιού χεριού, ποδιών ή γλώσσας στο BCI-IV 2a. Για την αξιολόγηση, χρησιμοποιούμε τις μετρικές Balanced Accuracy και ROC-AUC, οι οποίες είναι χρήσιμες, ιδιαίτερα σε μη ισορροπημένα σύνολα δεδομένων.

Πειραματική Αξιολόγηση

Αποτελέσματα: SEED

Στο σύνολο δεδομένων SEED, το Subject-Dependent (Πίναχας 2) πειραματικό πλαίσιο δείχνει ότι το SE επιτυγχάνει το μέγιστο συνολικό Balanced Accuracy, με ποσοστό 93.8%. Πολύ κοντά σε αυτά τα αποτελέσματα, τα χαρακτηριστικά TKEO-12 FB παρουσιάζουν ακρίβεια μόλις 3.6% χαμηλότερη στη συγχωνευμένη ζώνη (fused-band), δηλαδή στα συνενωμένα χαρακτηριστικά των επιμέρους ζωνών. Αξιοσημείωτο είναι ότι, σε σχεδόν όλες τις πειραματικές διατάξεις, τα TKEO χαρακτηριστικά υπερέχουν της μεθόδου αναφοράς PSD ως προς το Balanced Accuracy, καθώς και των δύο μεθόδων αναφοράς ως προς το ROC-AUC, γεγονός που υποδηλώνει, ότι η προτεινόμενη προσέγγιση επιτυγχάνει ανώτερη διαχωρισιμότητα μεταξύ των κλάσεων σε σχέση με τις μεθόδους αναφοράς. Επιπλέον, τα χαρακτηριστικά της συγχωνευμένης ζώνης υπερέχουν εκείνων των επιμέρους ζωνών, γεγονός που υποδεικνύει ότι η ενσωμάτωση πληροφορίας από πολλαπλές συχνοτικές μπάντες βελτιώνει την απόδοση στην Αναγνώριση Συναισθημάτων. Τέλος, κατά τη σύγκριση επιμέρους ζωνών, οι ζώνες Beta και Gamma παρουσιάζουν υψηλότερη ακρίβεια από τη ζώνη Alpha, εύρημα που ευθυγραμμίζεται με τα αποτελέσματα που αναφέρονται από τους Zheng et al. [122].

Features		Balanc	ed Accura	cy (%)	ROC-AUC ($\times 10^2$)						
	Alpha	Beta	Gamma	Raw	Fused	Alpha	Beta	Gamma	Raw	Fused	
SE PSD	$ \begin{array}{c} \hline 84.4_{\pm 10.2} \\ 74.2_{\pm 17.5} \end{array} $	$ \begin{array}{c} 83.1_{\pm 11.1} \\ 79.6_{\pm 18.3} \end{array} $	$ 82.2_{\pm 13.7} 69.8_{\pm 18.8} $	$ 80.4_{\pm 15.1} 85.8_{\pm 11.1} $	$\overline{ 93.8_{\pm 8.3} \atop 86.2_{\pm 12.5} }$	$\begin{array}{c} \hline 93.1_{\pm 8.2} \\ 90.0_{\pm 12.6} \end{array}$	$ \begin{array}{r} \hline 94.2_{\pm 7.7} \\ 91.3_{\pm 10.3} \end{array} $	$ \begin{array}{r} \hline 93.5_{\pm 7.7} \\ 87.8_{\pm 10.3} \end{array} $	$89.3_{\pm 7.6}$ $96.4_{\pm 4.1}$	$ \begin{array}{r} \hline 97.6_{\pm 3.7} \\ 94.4_{\pm 6.8} \end{array} $	
TKEO-12 FB TKEO-25 FB	$86.2_{\pm 10.4} \ 86.7_{\pm 12.9}$	$89.3_{\pm 9.7} \ 88.9_{\pm 10.5}$	$88.0_{\pm 13.4} \\ 86.7_{\pm 10.3}$	$85.8_{\pm 9.1} \\ 87.1_{\pm 9.9}$	$90.2_{\pm 8.7}\atop88.4_{\pm 11.0}$	$94.7_{\pm 6.3} \\ 97.3_{\pm 3.5}$	$97.1_{\pm3.8}\ 96.2_{\pm5.0}$	$93.8_{\pm 8.1}0$	$95.3_{\pm 4.8} \\ 95.6_{\pm 4.5}$	$97.6_{\pm 4.3} \\ 97.1_{\pm 4.7}$	
TKEO-50 FB Selected-12 FB	$85.3_{\pm 12.0}$ $84.9_{\pm 11.8}$	$87.1_{\pm 10.2}$ $83.6_{\pm 17.2}$	$85.8_{\pm 11.9}$	$86.7_{\pm 10.6}$	$87.1_{\pm 10.4}$		$96.0_{\pm 5.6} \\ 95.8_{\pm 7.6}$	$94.7_{\pm 7.8} \\ 95.8_{\pm 7.8}$	$egin{array}{c} 97.3_{\pm 4.1} \ 96.2_{\pm 4.7} \end{array}$	$98.2_{\pm 2.7}$ $97.6_{\pm 5.1}$	
Selected-25 FB Selected-50 FB Combined	$82.2_{\pm 12.1} \\ 85.3_{\pm 12.2} \\ 79.1_{\pm 14.8}$	$85.3_{\pm 14.8}$ $86.7_{\pm 13.5}$ $83.6_{\pm 13.7}$	$86.7_{\pm 11.9}$ $84.9_{\pm 11.8}$ $79.1_{\pm 14.8}$	$88.0_{\pm 9.8} \\ 86.7_{\pm 12.2} \\ 86.2_{\pm 14.3}$		$95.6_{\pm 6.4}$	$96.2_{\pm 4.7} \\ 94.5_{\pm 6.8} \\ 94.0_{\pm 8.9}$	$94.2_{\pm 9.1}$ $95.6_{\pm 6.7}$ $90.2_{\pm 11.1}$	$97.3_{\pm 4.3}$ $97.3_{\pm 4.6}$ $95.5_{\pm 7.2}$	$97.8_{\pm 5.8}$ $96.4_{\pm 4.6}$ $95.8_{\pm 5.8}$	

Table 2 Μετρικές Ακρίβειας για το Subject-Dependent στο Σύνολο Δεδομένων SEED.

Στο Subject-Independent (Πίναχας 3) πειραματιχό πλαίσιο, το SE επιτυγχάνει επίσης το υψηλότερο συνολιχό Balance Accuracy (68.1%), ενώ η Selected-25 FB παρουσιάζει μόλις 0.5% χαμηλότερη επίδοση στη συγχωνευμένη ζώνη (fused-band). Επιπλέον, οι τιμές μετριχών του PSD είναι χαμηλότερες και εδώ από αυτές των ΤΚΕΟ χαραχτηριστιχών σε όλες τις μπάντες, εχτός της ευρείας ζώνης μπάντα "raw-band". Αξίζει να σημειωθεί, ότι η χρήση συστοιχίας φίλτρων Gabor με περισσότερα από 12 φίλτρα βελτιώνει γενιχά την αχρίβεια, καθώς η αυξημένη φασματιχή ανάλυση επιτρέπει στο ΤΚΕΟ να ανιχνεύει ταλαντώσεις στενής ζώνης, οι οποίες διαφορετιχά θα εξομαλύνονταν από ευρύτερες φασματιχές διαιρέσεις.

Features		Balance	ed Accura	acy (%)		ROC-AUC $(\times 10^2)$						
	Alpha	Beta	Gamma	Raw	Fused	Alpha	Beta	Gamma	Raw	Fused		
SE PSD	$\frac{58.1_{\pm 5.8}}{46.7_{\pm 4.2}}$	$ 61.4_{\pm 1.7} $ $55.5_{\pm 4.7}$	$\overline{60.6_{\pm 3.4}}$ $55.6_{\pm 4.2}$	$ 55.3_{\pm 4.5} 63.2_{\pm 2.1} $	$\overline{68.1_{\pm 3.9}}$ $62.0_{\pm 4.2}$	$75.7_{\pm 4.7}$ $64.9_{\pm 5.2}$	$79.4_{\pm 2.4}$ $75.7_{\pm 3.8}$	$79.6_{\pm 3.1}$ $76.0_{\pm 2.6}$	$73.4_{\pm 4.7}$ $81.4_{\pm 1.8}$	$84.9_{\pm 2.9} \\ 80.6_{\pm 3.5}$		
TKEO-12 FB TKEO-25 FB TKEO-50 FB Selected-12 FB Selected-25 FB Selected-50 FB Combined	$\begin{array}{c} 62.3_{\pm 3.7} \\ 62.8_{\pm 3.9} \\ 62.6_{\pm 3.8} \\ 63.4_{\pm 3.8} \\ 63.2_{\pm 3.5} \\ \textbf{63.6}_{\pm 4.0} \\ 59.7_{\pm 4.5} \end{array}$	$\begin{array}{c} 61.1_{\pm 3.2} \\ 61.7_{\pm 3.8} \\ 61.8_{\pm 3.1} \\ 61.1_{\pm 3.6} \\ 61.4_{\pm 3.5} \\ \textbf{62.0}_{\pm 3.9} \\ 57.8_{\pm 4.4} \end{array}$	$\begin{array}{c} 61.8_{\pm3.6} \\ 61.9_{\pm3.5} \\ 61.4_{\pm3.3} \\ 62.9_{\pm2.6} \\ 62.9_{\pm4.1} \\ \textbf{63.2}_{\pm3.2} \\ 56.1_{\pm3.5} \end{array}$	$60.9_{\pm3.7}\atop 60.7_{\pm2.7}\atop 61.4_{\pm3.7}\atop 61.4_{\pm2.7}\atop 62.3_{\pm3.4}\atop 62.1_{\pm2.9}\\ 64.2_{\pm1.8}$	$67.0_{\pm 3.9}$	$\begin{array}{c} 80.5_{\pm3.1} \\ 80.4_{\pm3.1} \\ 80.5_{\pm2.9} \\ 81.3_{\pm3.1} \\ 81.0_{\pm2.8} \\ \textbf{81.3}_{\pm2.9} \\ 77.9_{\pm3.4} \end{array}$	$\begin{array}{c} 79.7_{\pm 2.9} \\ 79.9_{\pm 3.2} \\ \textbf{80.1}_{\pm 2.9} \\ 79.6_{\pm 3.1} \\ 79.9_{\pm 3.1} \\ 80.1_{\pm 3.1} \\ 77.8_{\pm 3.2} \end{array}$	$80.1_{\pm 3.3} \\ 79.9_{\pm 3.1} \\ 79.9_{\pm 3.1} \\ 80.8_{\pm 2.9} \\ 80.6_{\pm 3.4} \\ 80.8_{\pm 3.2} \\ 77.1_{\pm 2.3}$	$79.4_{\pm 2.9}$ $79.3_{\pm 2.3}$ $79.6_{\pm 2.8}$ $79.6_{\pm 2.6}$ $80.0_{\pm 2.6}$ $80.1_{\pm 2.3}$ $82.1_{\pm 1.8}$	$83.5_{\pm 3.2} \\ 83.5_{\pm 3.1} \\ 83.7_{\pm 3.0} \\ 84.3_{\pm 2.6} \\ 84.4_{\pm 2.8} \\ 84.0_{\pm 2.9} \\ 82.4_{\pm 3.1}$		

Table 3 Μετρικές Ακρίβειας για το Subject-Independent στο Σύνολο Δεδομένων SEED.

Αποτελέσματα: DEAP

Το Subject-Dependent (Πίναχες 4, 5) πειραματικό πλαίσιο στο σύνολο δεδομένων DEAP παρουσιάζει σταθερά υψηλότερες τιμές ακρίβειας για τα χαρακτηριστικά που βασίζονται στην TKEO, υπερέχοντας των μεθόδων αναφοράς στην ταξινόμηση arousal, ενώ στην περίπτωση του valence, το PSD εμφανίζει τις υψηλότερες τιμές (Balanced Accuracy 64.7%, ROC-AUC 70.2). Μεταξύ αυτών, τα χαρακτηριστικά Selected-50 FB επιτυγχάνουν τα καλύτερα αποτελέσματα, με Balanced Accuracy 64.6% και 59.2%, καθώς και τιμές ROC-AUC 69.4 και 64.0 στη συγχωνευμένη ζώνη (fused-band) για τις διαστάσεις valence και arousal, αντίστοιχα. Η συγχώνευση φασματικών ζωνών ενισχύει περαιτέρω την απόδοση σε όλες τα τα χαρακτηριστικά που εξάγονται με χρήση TKEO, επιβεβαιώνοντας ότι η ενσωμάτωση συμπληρωματικής φασματικής πληροφορίας ωφελεί την Αναγνώριση Συναισθημάτων από ΗΕΓ.

Στη διάσταση του valence, η Gamma μπάντα υπερέχει των Alpha και Beta μπαντών, γεγονός που υποδηλώνει, ότι η δραστηριότητα υψηλότερων συχνοτήτων του ΗΕΓ μεταφέρει πλουσιότερη συναισθηματική πληροφορία στο συγκεκριμένο πλαίσιο. Συνολικά, η ταξινόμηση valence παρουσιάζει ανώτερη απόδοση σε σχέση με το arousal για όλα τα σύνολα χαρακτηριστικών, υποδεικνύοντας ότι τα στιγμιαία μοτίβα ενέργειας που συνδέονται με το valence είναι πιο διακριτά και σταθερά, ενώ η δραστηριότητα που σχετίζεται με το arousal τείνει να είναι περισσότερο μεταβλητή.

Το Subject-Independent (Πίνακας 6) πειραματικό πλαίσιο παρουσιάζει τη αναμενόμενη μείωση της συνολικής ακρίβειας σε σύγκριση με το Subject-Dependent, γεγονός που αντικατοπτρίζει τη μεγαλύτερη μεταβλητότητα που εισάγεται, λόγω των διαφοροποιήσεων μεταξύ των ατόμων. Οι τιμές απόδοσης συγκλίνουν γύρω από το 50%, αναδεικνύοντας τη δυσκολία γενίκευσης μεταξύ συμμετεχόντων στο πρόβλημα Αναγνώρισης Συναισθημάτων.

Μεταξύ των χαρακτηριστικών που αξιολογήθηκαν, οι αναπαραστάσεις βασισμένες στην ΤΚΕΟ

Features		Balanc	ed Accura	cy (%)		ROC-AUC ($\times 10^2$)						
	Alpha	Beta	Gamma	Raw	Fused	Alpha	Beta	Gamma	Raw	Fused		
SE PSD	$ 60.8_{\pm 11.8} 59.4_{\pm 10.9} $	$62.8_{\pm 12.2} 62.9_{\pm 13.9}$	$61.8_{\pm 8.8}$ $63.5_{\pm 9.1}$	$ 62.8_{\pm 11.6} $ $ 64.7_{\pm 9.1} $	$\overline{63.0_{\pm 11.2}_{\pm 10.6}}$ $63.8_{\pm 10.6}$	$ 66.1_{\pm 14.7} 62.9_{\pm 13.6} $	$\overline{68.6_{\pm 14.2}}$ $67.6_{\pm 16.7}$	$ 66.7_{\pm 11.8} 67.2_{\pm 13.6} $	$\overline{66.9_{\pm 13.9}}_{70.2_{\pm 10.8}}$	$ 68.4_{\pm 12.9} $ $ 68.4_{\pm 13.7} $		
TKEO-12 FB	$60.6_{\pm 10.3}$	$62.0_{\pm 12.0}$	$63.6_{\pm 11.1}$	$62.3_{\pm 11.5}$	$64.3_{\pm 9.2}$	$65.0_{\pm 13.1}$	$65.4_{\pm 15.5}$	$69.2_{\pm 13.8}$	$66.1_{\pm 11.5}$	$70.6_{\pm 10.8}$		
TKEO-25 FB	$60.2_{\pm10.6}$		$64.0_{\pm 10.1}$	$61.2 \scriptstyle{\pm 9.2}$	$63.1_{\pm10.5}$	$63.3_{\pm 12.0}$	$67.6_{\pm 13.5}$	$68.5_{\pm 12.5}$	$65.5_{\pm 9.1}$	$68.5_{\pm 12.1}$		
TKEO- 50 FB	$61.4_{\pm 9.7}$		$\textbf{64.2}_{\pm 10.4}$			$65.6_{\pm13.0}$		$\textbf{69.8}_{\pm 13.0}$	$64.1_{\pm 12.8}$	$68.4_{\pm 12.3}$		
Selected-12 FB	$61.4_{\pm 11.5}$			$62.9_{\pm 10.3}$		$65.5_{\pm 14.0}$	$66.5_{\pm 14.4}$	$67.4_{\pm 12.2}$	$65.9_{\pm 14.2}$	$69.1_{\pm 13.9}$		
Selected-25 FB	$60.6_{\pm 9.7}$	$61.6_{\pm 10.9}$	$61.1_{\pm10.5}$	$62.3_{\pm 10.4}$		$62.4_{\pm 15.2}$	$65.5_{\pm 14.1}$	$67.3_{\pm 12.9}$	$69.2_{\pm 13.3}$	$67.8_{\pm 12.2}$		
Selected- 50 FB	60.6 ± 12.1	$60.3_{\pm 12.3}$	$62.3_{\pm 10.5}$	$62.1_{\pm 11.1}$	$\textbf{64.6}{\scriptstyle\pm10.4}$	$63.4_{\pm 15.6}$	$64.6_{\pm 13.9}$	$67.9_{\pm 13.0}$	$64.9_{\pm 14.8}$	$69.4_{\pm 13.5}$		
Combined	$57.5_{\pm 7.5}$	$60.5_{\pm 9.6}$	$60.8_{\pm 8.9}$	$62.7_{\pm8.8}$	$60.8_{\pm7.7}$	$61.5{\scriptstyle\pm10.5}$	$65.5_{\pm 12.5}$	$64.9_{\pm 11.3}$	$66.9_{\pm11.4}$	$65.1{\scriptstyle~\pm10.5}$		

Table 4 Μετρικές Ακρίβειας του Valence για το Subject-Dependent στο Σύνολο Δεδομένων DEAP.

Features		Baland	ed Accura	acy (%)		ROC-AUC ($\times 10^2$)					
	Alpha	Beta	Gamma	Raw	Fused	Alpha	Beta	Gamma	Raw	Fused	
SE PSD	$\overline{57.0_{\pm 8.7}}$ $54.3_{\pm 8.7}$	$ 56.4_{\pm 9.8} $ $56.2_{\pm 10.9}$	$55.6_{\pm 9.6}_{\pm 9.9}$ $54.7_{\pm 9.9}$	$ 53.4_{\pm 11.6} $ $55.2_{\pm 10.0}$	$58.5_{\pm 8.2}$ $57.0_{\pm 9.5}$	$ 62.4_{\pm 12.5} $ $58.0_{\pm 12.9}$	$\frac{59.8_{\pm 14.1}}{56.9_{\pm 15.4}}$	$\frac{59.3_{\pm 11.9}}{55.5_{\pm 13.9}}$	$\frac{54.6_{\pm 14.3}}{57.5_{\pm 13.6}}$	$\overline{62.6_{\pm 10.7}\atop 60.4_{\pm 13.1}}$	
TKEO-12 FB	$58.0_{\pm 8.9}$	$55.2_{\pm 12.2}$	$56.6_{\pm 11.3}$	$\textbf{58.1}_{\pm 10.0}$	$58.0_{\pm 8.8}$	$59.4_{\pm 12.6}$	$59.1_{\pm 15.2}$	$60.2_{\pm 14.6}$	$60.7_{\pm 14.2}$	$63.3_{\pm 11.3}$	
TKEO- 25 FB	$54.0_{\pm 9.9}$	$55.6_{\pm 12.1}$	$58.2_{\pm 10.1}$	$55.4_{\pm 10.0}$	$57.1_{\pm 9.8}$	$57.4_{\pm 13.8}$	$56.6_{\pm 16.5}$	$61.0_{\pm 14.8}$	$60.6_{\pm 11.5}$	$61.7_{\pm 12.7}$	
TKEO-50 FB	$55.6_{\pm 7.9}$	$56.2_{\pm 11.8}$	$56.9_{\pm 9.6}$	$56.1_{\pm 10.2}$	$58.3_{\pm 7.9}$	$58.7_{\pm 12.1}$	$57.2_{\pm 15.9}$	$59.7_{\pm 13.1}$	$57.4_{\pm 14.7}$	$61.5_{\pm 11.2}$	
Selected-12 FB	$56.8_{\pm 9.8}$	$55.1_{\pm 10.0}$	$57.2_{\pm 11.5}$	$57.5_{\pm 8.6}$	$58.9_{\pm 8.6}$	$61.4_{\pm 14.4}$	$58.7_{\pm 15.4}$	${\bf 61.6}_{\pm 13.2}$	${\bf 60.9}_{\pm 12.4}$	$62.8_{\pm 11.4}$	
Selected-25 FB	$57.2_{\pm 9.5}$	$57.0_{\pm 10.2}$		$57.1_{\pm 10.7}$	$57.6_{\pm 10.0}$	$60.1_{\pm 13.6}$	$58.6_{\pm 13.6}$	$59.7_{\pm 15.0}$	$60.5_{\pm 12.5}$	$60.7_{\pm 14.9}$	
Selected- 50 FB	$58.2_{\pm 8.7}$		$55.8_{\pm 8.7}$	$56.3_{\pm 10.0}$	$59.2_{\pm7.8}$	$61.0_{\pm 13.3}$	${\bf 60.9}_{\pm 13.9}$	$59.1_{\pm 12.2}$	$60.0_{\pm 13.9}$	${\bf 64.0}_{\pm 11.1}$	
Combined	$55.8_{\pm6.5}$	$53.9_{\pm 9.0}$	$53.5_{\pm 8.0}$	$55.0_{\pm 7.9}$	$54.9_{\pm 6.9}$	$57.6_{\pm 7.6}$	$55.4_{\pm 12.8}$	$56.3_{\pm 11.0}$	$57.2_{\pm 11.4}$	$58.4_{\pm 9.7}$	

Table 5 Μετρικές Ακρίβειας του Arousal για το Subject-Dependent στο Σύνολο Δεδομένων DEAP.

επιτυγχάνουν συγκρίσιμη απόδοση με τις μεθόδους αναφοράς, διατηρώντας το Balanced Accuracy μεταξύ 50–53% και τις τιμές ROC–AUC περίπου 51–56. Τα καλύτερα αποτελέσματα προκύπτουν από τα χαρακτηριστικά Combined και Selected-12 FB, τα οποία υπερέχουν ελαφρώς των υπολοίπων, επιτυγχάνοντας Balanced Accuracy 54.2% και 54.0%, καθώς και ROC–AUC 56.2 και 54.8, αντίστοιχα.

Τα ευρήματα αυτά υποδηλώνουν ότι, αν και ο ΤΚΕΟ εντοπίζει χρήσιμη πληροφορία για τις δυναμικές των νευρωνικών σημάτων, η διακριτική της ικανότητα είναι περιορισμένη υπό Subject-Independent συνθήκες. Σε αντίθεση με τη ρύθμιση Subject-Dependent, η συγχώνευση φασματικών ζωνών προσφέρει εδώ οριακές μόνο βελτιώσεις, γεγονός που δείχνει ότι η γενίκευση μεταξύ ατόμων εξαρτάται περισσότερο από αμετάβλητα χωρο-χρονικά μοτίβα παρά από φασματικές διαφορές ενέργειας συγκεκριμένων ζωνών.

Features		Balance	ed Accura	acy (%)	ROC-AUC $(\times 10^2)$					
	Alpha	Beta	Gamma	Raw	Fused	Alpha	Beta	Gamma	Raw	Fused
SE PSD	$52.8_{\pm 2.4} \atop 51.0_{\pm 0.6}$	$ 53.6_{\pm 2.6} $ $53.0_{\pm 2.6}$	$ 51.1_{\pm 4.4} $ $52.5_{\pm 1.9}$	$\overline{54.0_{\pm 2.6}}$ $53.4_{\pm 2.8}$	$\overline{53.6_{\pm 3.3}}$ $54.7_{\pm 3.6}$	$\overline{53.7_{\pm 3.2}}$ $52.4_{\pm 4.2}$	$\overline{54.8_{\pm 4.2}}$ $54.1_{\pm 3.9}$	$\overline{51.3_{\pm 6.3}}$ $51.4_{\pm 0.8}$	$55.9_{\pm 3.9}$ $54.5_{\pm 2.2}$	$\overline{ 54.8_{\pm 5.2} } $ $56.0_{\pm 5.0}$
TKEO-12 FB TKEO-25 FB TKEO-50 FB Selected-12 FB Selected-25 FB Selected-50 FB Combined	$\begin{array}{c} 52.0_{\pm 1.7} \\ 52.3_{\pm 1.0} \\ 52.5_{\pm 2.4} \\ 52.2_{\pm 1.3} \\ 52.8_{\pm 1.9} \\ 53.1_{\pm 1.7} \\ \textbf{53.2}_{\pm 3.1} \end{array}$	$53.4_{\pm 3.2}$ $52.4_{\pm 3.4}$ $53.0_{\pm 3.4}$ $54.0_{\pm 2.5}$ $52.3_{\pm 3.0}$ $52.5_{\pm 2.3}$ $53.6_{\pm 2.6}$	$\begin{array}{c} 51.5_{\pm3.6} \\ 51.0_{\pm2.5} \\ 50.3_{\pm3.5} \\ 51.0_{\pm3.1} \\ 51.1_{\pm2.8} \\ 50.8_{\pm3.2} \\ \textbf{52.8}_{\pm4.1} \end{array}$	$\begin{array}{c} 50.7_{\pm 2.8} \\ 51.1_{\pm 1.1} \\ 51.0_{\pm 1.8} \\ 50.1_{\pm 2.2} \\ 50.6_{\pm 2.1} \\ 50.3_{\pm 1.7} \\ 54.2_{\pm 3.7} \end{array}$	$\begin{array}{c} 52.6_{\pm 2.8} \\ 52.5_{\pm 3.3} \\ 53.2_{\pm 3.0} \\ 52.6_{\pm 2.4} \\ 52.0_{\pm 3.1} \\ 52.8_{\pm 2.5} \\ 54.1_{\pm 2.7} \end{array}$	$\begin{array}{c} 52.9_{\pm 2.1} \\ 53.6_{\pm 1.6} \\ 53.3_{\pm 2.6} \\ 52.7_{\pm 1.4} \\ 54.1_{\pm 2.3} \\ 53.4_{\pm 2.2} \\ 54.8_{\pm 3.9} \end{array}$	$\begin{array}{c} 53.4_{\pm 4.1} \\ 53.2_{\pm 4.8} \\ 53.0_{\pm 4.8} \\ 54.8_{\pm 3.2} \\ 53.5_{\pm 3.6} \\ 53.3_{\pm 3.5} \\ \textbf{55.2}_{\pm 4.4} \end{array}$	$51.8_{\pm 4.9}$ $51.6_{\pm 3.5}$ $51.0_{\pm 5.2}$ $50.8_{\pm 4.7}$ $51.6_{\pm 5.0}$ $50.7_{\pm 4.9}$ $53.0_{\pm 5.8}$	$51.0_{\pm 3.6}$ $51.5_{\pm 1.7}$ $51.5_{\pm 2.7}$ $50.3_{\pm 2.9}$ $50.8_{\pm 2.8}$ $50.3_{\pm 2.9}$ $56.2_{\pm 5.3}$	$52.9_{\pm 4.7} \\ 53.1_{\pm 4.7} \\ 53.3_{\pm 4.7} \\ 52.9_{\pm 3.6} \\ 53.1_{\pm 3.5} \\ 53.6_{\pm 4.1} \\ 55.2_{\pm 4.7}$

Table 6 Μετρικές Ακρίβειας του Valence για το Subject-Independent στο Σύνολο Δ εδομένων DEAP.

Αποτελέσματα: BCI-IV 2a

Όπως φαίνεται στους Πίναχες 8 και 9, στο σύνολο δεδομένων BCI-IV 2a τα Selected ΤΚΕΟ χαρακτηριστικά υπερέχουν σταθερά όλων των άλλων συνόλων χαρακτηριστικών στο πρόβλημα Κινητικής Νοερής Απεικόνισης.

Στο Subject-Dependent πειραματικό πλαίσιο, η συγχωνευμένη ζώνη (fused-band) επιτυγχάνει τη υψηλότερη συνολική απόδοση, με Balanced Accuracy 51.2% και ROC-AUC 77.0, υπερβαίνοντας σημαντικά την τυχαία ταξινόμηση. Επιπλέον, η ενσωμάτωση ΤΚΕΟ χαρακτηριστικών με τις μεθόδους αναφοράς οδηγεί σε βελτιωμένη απόδοση σε σχέση με τη χρήση μόνο της PSD, γεγονός που αναδεικνύει τη συμπληρωματική φύση των χαρακτηριστικών αυτών.

Κατά τη σύγκριση διαφορετικών συστοιχιών φίλτρων Gabor, παρατηρείται ότι η χρήση περισσότερων από 12 φίλτρων τείνει να βελτιώνει την απόδοση στις περισσότερες περιπτώσεις. Αυτό υποδηλώνει, ότι ένα πυκνότερο φασματικό φίλτρο παρέχει υψηλότερη φασματική ανάλυση, επιτρέποντας στην ΤΚΕΟ να αποτυπώνει δυναμικές ΗΕΓ στενής ζώνης, που διαφορετικά θα εξομαλύνονταν με μικρότερο αριθμό φίλτρων.

Επιπλέον, η ζώνη Beta φαίνεται να αποδίδει καλύτερα σε σύγκριση με τις υπόλοιπες επιμέρους ζώνες στα ΤΚΕΟ χαρακτηριστικά, εύρημα που συμφωνεί με τα αποτελέσματα των Scherer et al. [100] για το πρόβλημα της Κινητικής Νοερής Απεικόνισης.

Στο Subject-Independent (Πίναχας 8) πειραματικό πλαίσιο, παρατηρούνται παρόμοιες τάσεις με εκείνες του Subject-Dependent πλαισίου. Τα χαρακτηριστικά Selected-50 FB επιτυγχάνουν το υψηλότερο Balanced Accuracy (41.0%) και ROC-AUC 66.8. Η συνδυαστική χρήση χαρακτηριστικών PSD και TKEO βελτιώνει περαιτέρω την απόδοση, επιβεβαιώνοντας τα ευρήματα του Subject-Dependent πλαισίου.

Features		Balance	ed Accura	acy (%)	ROC-AUC ($\times 10^2$)					
	Alpha	Beta	Gamma	Raw	Fused	Alpha	Beta	Gamma	Raw	Fused
SE PSD	$\overline{50.1_{\pm 0.9}\atop 50.6_{\pm 0.2}}$	$\overline{51.9_{\pm 2.0}}$ $50.3_{\pm 2.0}$	$ 51.5_{\pm 1.7} $ $50.9_{\pm 0.8}$	$\overline{49.3_{\pm 1.5}}_{52.0_{\pm 2.4}}$	$\overline{51.9_{\pm 1.5}}$ $50.7_{\pm 2.8}$	$ 51.3_{\pm 1.3} $ $50.2_{\pm 1.5}$	$\overline{52.3_{\pm 3.2}}$ $51.6_{\pm 2.6}$	$ 52.3_{\pm 2.3} $ $50.3_{\pm 0.8}$	$\overline{49.0_{\pm 2.5}}_{50.3_{\pm 3.3}}$	$ 52.8_{\pm 2.8} $ $50.9_{\pm 3.5}$
TKEO-12 FB	$51.5_{\pm 1.6}$	$50.4_{\pm 1.4}$	$52.0_{\pm 1.4}$	$51.5_{\pm 2.7}$	$51.9_{\pm 1.4}$	51.8 _{±1.9}	$49.9_{\pm 1.6}$	$52.8_{\pm 2.0}$	$51.6_{\pm 3.3}$	$52.0_{\pm 1.9}$
TKEO- $25~\mathrm{FB}$	$51.1_{\pm 1.2}$	$50.1_{\pm 1.6}$	$51.1_{\pm 1.1}$	$52.1_{\pm1.7}$	$52.3_{\pm1.0}$	$51.7_{\pm 0.9}$	$50.5_{\pm 1.3}$	$52.1_{\pm 1.5}$	$52.4_{\pm 2.2}$	$53.6_{\pm1.6}$
TKEO-50 FB	$50.8_{\pm 1.5}$	$50.4_{\pm 1.9}$	$52.1_{\pm 1.5}$	$50.1_{\pm 2.5}$	$52.1_{\pm 1.2}$	$51.9_{\pm 1.6}$	$50.9_{\pm 2.0}$	$52.8_{\pm 2.8}$	$50.7_{\pm 2.8}$	$53.3_{\pm 2.0}$
Selected-12 FB	$50.9_{\pm 1.3}$	$49.4_{\pm 0.3}$	$52.2_{\pm 1.5}$	$50.4_{\pm 1.5}$	$51.4_{\pm 1.6}$	$51.5_{\pm 1.4}$	$49.1_{\pm0.8}$	$52.9_{\pm 2.0}$	$51.1_{\pm 1.9}$	$52.1_{\pm 2.0}$
Selected-25 FB	$51.4_{\pm 0.7}$	$49.9_{\pm 0.8}$	$51.5_{\pm 1.2}$	$50.8_{\pm1.8}$	$52.1_{\pm 1.7}$	$52.0_{\pm 2.1}$	$49.8_{\pm0.5}$	$51.8_{\pm 1.7}$	$50.9_{\pm 2.5}$	$52.5_{\pm 2.3}$
Selected- 50 FB	$51.2_{\pm 1.7}$	$49.7_{\pm 0.6}$	$50.7_{\pm2.1}$	$50.5_{\pm1.4}$	$52.0_{\pm 1.0}$	$51.5_{\pm 2.0}$	$50.2_{\pm 1.6}$	$51.0_{\pm 2.1}$	$51.4_{\pm 2.5}$	$52.5_{\pm 1.6}$
Combined	$51.7_{\pm0.7}$	$51.0_{\pm 1.6}$	$51.4_{\pm1.6}$	$51.1_{\pm2.5}$	$52.0_{\pm0.8}$	$52.0_{\pm0.8}$	$52.2_{\pm2.1}$	$52.1_{\pm2.8}$	$51.4_{\pm 3.3}$	$53.0_{\pm1.6}$

Table 7 Μετρικές Ακρίβειας του Arousal για το Subject-Independent στο Σύνολο Δεδομένων DEAP.

Features		Balance	ed Accura	cy (%)	ROC-AUC ($\times 10^2$)						
	Alpha	Beta	Gamma	Raw	Fused	Alpha	Beta	Gamma	Raw	Fused	
SE PSD	$\frac{44.1_{\pm 14.7}}{40.7_{\pm 13.2}}$	$\overline{43.6_{\pm 7.5}}_{38.2_{\pm 6.6}}$	$37.6_{\pm 8.2}$ $28.3_{\pm 5.3}$	$\begin{array}{c} \hline 40.4_{\pm 8.1} \\ 43.2_{\pm 5.9} \end{array}$	$47.1_{\pm 8.8}\atop 40.6_{\pm 6.0}$	$\overline{70.4_{\pm 12.8}\atop 65.7_{\pm 13.4}}$	$ 70.6_{\pm 8.0} 67.4_{\pm 5.7} $	$\overline{66.3_{\pm 8.5}}$ $56.2_{\pm 6.3}$	$ \begin{array}{r} \hline 67.3_{\pm 8.4} \\ 71.7_{\pm 6.1} \end{array} $	$\overline{73.7_{\pm 8.2}\atop 67.9_{\pm 7.7}}$	
TKEO - 12 FB	$44.6_{\pm 12.6}$	$47.5_{\pm 10.2}$	$43.5_{\pm 7.0}$	$46.4_{\pm 9.0}$	$49.5_{\pm 10.0}$	$70.1_{\pm 13.6}$	$74.6_{\pm 9.7}$	$68.9_{\pm 9.6}$	$72.7_{\pm 9.8}$	$74.9_{\pm 9.0}$	
TKEO - 25 FB	$43.4_{\pm 13.1}$	$48.6_{\pm 10.3}$	$43.3_{\pm7.4}$	$45.9_{\pm 9.2}$	$49.7_{\pm 10.6}$		$74.9_{\pm 9.2}$	$69.4_{\pm 9.2}$	$72.4_{\pm 9.7}$	$75.4_{\pm 8.8}$	
TKEO - 50 FB	$44.9_{\pm 13.1}$	$48.4_{\pm 10.4}$	$43.1_{\pm 7.9}$	$45.9_{\pm 8.6}$	$48.9_{\pm 9.1}$	$69.9_{\pm 13.5}$	$74.8_{\pm 9.8}$	$68.7_{\pm 9.1}$	$72.4_{\pm 9.7}$	$75.0_{\pm 8.8}$	
Selected - 12 FB	$45.4_{\pm 14.3}$	$49.1_{\pm 11.3}$	$44.9_{\pm 7.5}$	$47.7_{\pm 11.0}$	$49.8_{\pm 10.3}$	$71.2_{\pm 12.3}$	$75.0_{\pm 10.7}$	$71.8_{\pm 8.9}$	$73.3_{\pm 11.4}$	$75.8_{\pm 8.8}$	
Selected - 25 FB	$\textbf{45.8}{\scriptstyle\pm13.3}$		$45.3_{\pm7.1}$	$47.9_{\pm 10.7}$	$50.1_{\pm 11.0}$	$70.8_{\pm 12.6}$	$76.1_{\pm 9.9}$	$72.5_{\pm 8.1}$	$73.0_{\pm 11.5}$	$76.3_{\pm 8.6}$	
Selected - 50 FB	$45.7_{\pm 13.5}$	$50.0_{\pm 10.4}$		$48.9_{\pm 11.9}$		${\bf 71.4}_{\pm 11.8}$	$\textbf{76.1}_{\pm 9.1}$	$72.3_{\pm 8.8}$	$\textbf{73.7}_{\pm 11.6}$	$\textbf{77.0}_{\pm 8.6}$	
Combined	$42.7_{\pm 12.6}$	$41.4_{\pm 7.1}$	$31.3_{\pm6.3}$	$44.3_{\pm 6.9}$	$42.7_{\pm 7.4}$	$66.5_{\pm 14.2}$	$68.3_{\pm7.7}$	$60.3_{\pm 6.9}$	$72.4_{\pm 6.8}$	$68.6_{\pm 8.5}$	

Table 8 Μετρικές Ακρίβειας για το Subject-Dependent στο Σύνολο Δεδομένων BCI-IV 2a.

Αποτελέσματα: TUEP

Στο σύνολο δεδομένων TUEP (Πίνακας 10), τα Combined χαρακτηριστικά επιτυγχάνουν στις περισσότερες περιπτώσεις την υψηλότερη απόδοση. Πιο συγκεκριμένα, η Gamma μπάντα παρουσιάζει το μεγαλύτερο Balanced Accuracy (78.4%) —περίπου 15% υψηλότερο από τα υπόλοιπα σύνολα χαρακτηριστικών—, καθώς και τη μεγαλύτερη τιμή ROC-AUC (86.0). Το αποτέλεσμα αυτό είναι σύμφωνο με προηγούμενα ευρήματα, τα οποία δείχνουν ότι η απόδοση στην ανίχνευση επιληψίας βελτιώνεται με τη χρήση χαρακτηριστικών ΗΕΓ υψηλότερων συχνοτήτων [51].

Ενδεικτικά, παρουσιάζονται στο Σχήμα 4.2 οι τοπογραφικοί χάρτες των χαρακτηριστικών v-IFM για ένα επιληπτικό και ένα μη επιληπτικό σήμα, ανά φασματική μπάντα. Το επιληπτικό σήμα εμφανίζει έντονες διακυμάνσεις στη στιγμιαία συχνότητα, σχεδόν ομοιόμορφα σε όλα τα

Features		Balanc	ed Accura	acy (%)		ROC-AUC $(\times 10^2)$					
	Alpha	Beta	Gamma	Raw	Fused	Alpha	Beta	Gamma	Raw	Fused	
SE PSD	$37.3_{\pm 6.8}$ $36.1_{\pm 6.7}$	$35.1_{\pm 5.3}$ $35.6_{\pm 3.1}$	$32.8_{\pm 1.5} \\ 27.8_{\pm 2.2}$	$35.3_{\pm 4.3}$ $38.0_{\pm 5.8}$	$37.4_{\pm 4.8}$ $36.4_{\pm 5.0}$	$\overline{64.0_{\pm 6.1}\atop 62.3_{\pm 6.7}}$	$ 62.3_{\pm 4.8} 62.2_{\pm 4.0} $	$\overline{60.0_{\pm 1.3}\atop 54.1_{\pm 2.7}}$	$ 62.0_{\pm 4.5} 64.0_{\pm 6.0} $	$\overline{64.0_{\pm 5.0}}$ $63.0_{\pm 5.7}$	
TKEO - 12 FB	$37.8_{\pm 8.3}$	$38.2_{\pm 6.2}$	$35.3_{\pm 3.9}$	$39.2_{\pm 6.1}$	$38.4_{\pm 6.7}$	$64.1_{\pm7.3}$	$65.0_{\pm 6.3}$	$62.8_{\pm 4.3}$	$65.5_{\pm 5.0}$	$65.3_{\pm 6.4}$	
TKEO - 25 FB TKEO - 50 FB	$38.6_{\pm7.6} \ 37.4_{\pm7.4}$	$38.8_{\pm 6.6} \\ 39.7_{\pm 7.9}$	$35.5_{\pm2.6} \ 36.8_{\pm2.3}$	$39.7_{\pm 5.5} \\ 38.4_{\pm 4.8}$	$39.5_{\pm 5.8} \ 39.1_{\pm 6.7}$	$65.2_{\pm 6.5}$ $64.0_{\pm 6.9}$	$65.4_{\pm 6.2} \ 66.1_{\pm 7.0}$	$63.0_{\pm 3.3} \\ 63.2_{\pm 2.8}$	$65.3_{\pm 5.5}$ $64.4_{\pm 5.9}$	$65.9_{\pm 5.3}$ $65.4_{\pm 5.6}$	
Selected - 12 FB	$38.4_{\pm 8.0}$	$40.2_{\pm 8.8}$		$40.0_{\pm 6.1}$	$39.9_{\pm 6.8}$	$64.9_{\pm 7.6}$	$66.3_{\pm 7.2}$	$63.8_{\pm 3.3}$	$65.9_{\pm 6.5}$	$66.6_{\pm 6.4}$	
Selected - 25 FB	$38.6_{\pm 8.1}$	$39.4_{\pm 7.9}$	${f 39.0}_{\pm3.1}$	$\textbf{40.8}_{\pm 6.5}$		$64.9_{\pm 7.4}$	$66.2_{\pm7.0}$	$64.7_{\pm 3.4}$	$\textbf{66.0}_{\pm6.2}$	$66.2_{\pm 6.3}$	
Selected - 50 FB Combined	$39.2_{\pm 9.1} \ 37.0_{\pm 7.9}$	$40.5_{\pm 7.9} \ 36.5_{\pm 4.2}$	$38.3_{\pm 3.1} \ 32.8_{\pm 3.2}$	$39.6_{\pm 6.8} \\ 37.6_{\pm 6.4}$	$41.0_{\pm 7.3} \ 37.3_{\pm 6.6}$	$65.4_{\pm 7.9}$ $64.0_{\pm 7.2}$		$65.0_{\pm 3.0}$ $60.0_{\pm 2.9}$	$66.0_{\pm 6.6} \\ 64.8_{\pm 5.3}$	$66.8_{\pm 6.4} \ 64.2_{\pm 5.6}$	

Table 9 Μετρικές Ακρίβειας για το Subject-Independent στο Σύνολο Δεδομένων BCI-IV 2a.

κανάλια, σε αντίθεση με το μη επιληπτικό, όπου οι διακυμάνσεις είναι σημαντικά χαμηλότερες. Το εύρημα αυτό αναδεικνύει τις διακυμάνσεις συχνοτήτων στη Gamma μπάντα ως αξιόπιστο δείκτη επιληπτικής δραστηριότητας.

Αξίζει να αναφερθεί, ότι στη raw μπάντα, η ακρίβεια μειώνεται συγκριτικά με τις μεμονωμένες μπάντες, αλλά και με τις συγχωνευμένες (fused-band), γεγονός που υποδηλώνει ότι η συμπληρωματικότητα των ΤΚΕΟ χαρακτηριστικών εξασθενεί σε σήματα ευρείας μπάντας. Η παρατήρηση αυτή ενισχύει περαιτέρω την άποψη ότι ο ΤΚΕΟ παρουσιάζει αυξημένη ευαισθησία σε σήματα στενής ζώνης.

Features		Balance	ed Accura		RO	C-AUC (>	(10 ²)			
	Alpha	Beta	Gamma	Raw	Fused	Alpha	Beta	Gamma	Raw	Fused
SE PSD	$59.2_{\pm 2.5}$ $58.2_{\pm 2.4}$	$ 61.7_{\pm 7.9} 62.5_{\pm 4.9} $	$\overline{63.2_{\pm 8.4}}$ $61.7_{\pm 9.3}$		$\overline{61.4_{\pm 6.0}\atop 61.1_{\pm 7.6}}$		$ \begin{array}{c} \hline 64.5_{\pm 13.5} \\ 72.3_{\pm 13.6} \end{array} $			$75.5_{\pm 13.5} 74.2_{\pm 13.6}$
TKEO Selected Combined	$58.5_{\pm 2.3}$ $59.0_{\pm 2.8}$ $66.3_{\pm 6.2}$	$61.0_{\pm 0.9} \\ 60.0_{\pm 9.8} \\ \textbf{70.9}_{\pm 10.0}$	$61.6_{\pm7.2}$		$61.2_{\pm 5.9}$	$66.3_{\pm 2.9}$		$70.3_{\pm 13.6}^{-}$	$70.5_{\pm 14.5}^{-}$	$73.8_{\pm 11.2}$

Table 10 Μετρικές Ακρίβειας για το Subject-Independent στο Σύνολο Δεδομένων TUEP.

Επίλογος

Στην παρούσα Διπλωματική Εργασία, πραγματοποιήθηκε συστηματική αξιολόγηση των χαρακτηριστικών βασισμένων στον Ενεργειακό Τελεστή Teager-Kaiser σε τρία προβλήματα: Αναγνώριση Συναισθήματος, Ταξινόμηση Κινητικής Νοερής Απεικόνισης και Εντοπισμό Επιληψίας.

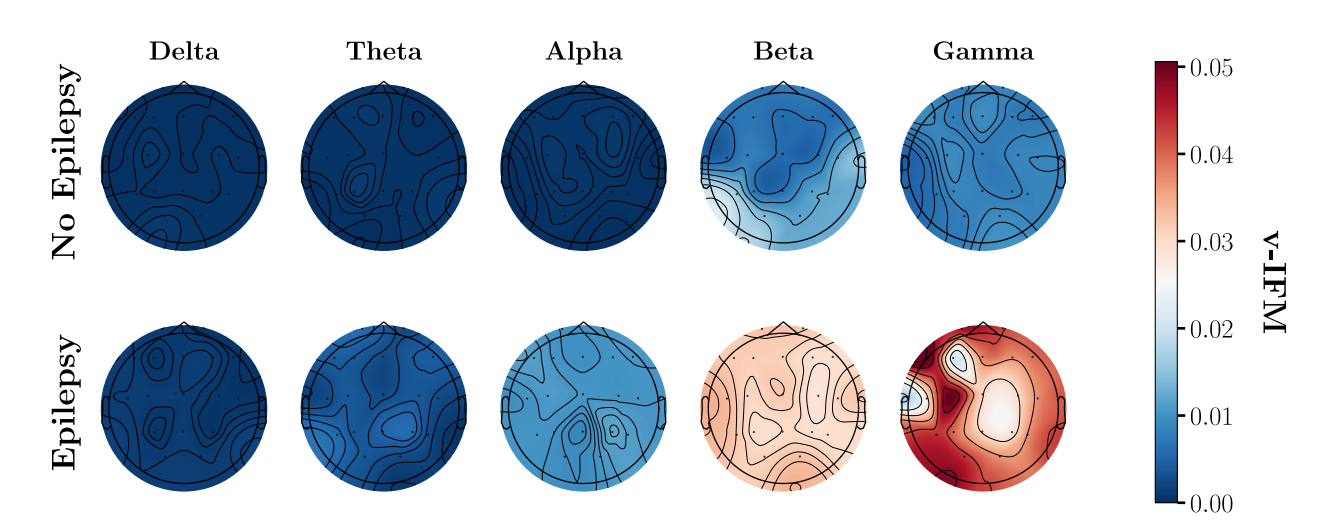


Figure 7 Τοπολογική Απεικόνιση των ΗΕΓ Καναλιών του Συνόλου Δεδομένων ΤUEP κάθε Συχνοτικής Μπάντας για το Χαρακτηριστικό v-IFM.

Μέσω αυτής της μελέτης, διερευνήθηκαν τα πλεονεκτήματα και οι περιορισμοί των ΤΚΕΟ χαρακτηριστικών στο πλαίσιο της ανάλυσης ΗΕΓ, ενώ προσδιορίστηκαν οι συνθήκες υπό τις οποίες η μέθοδος προσφέρει προστιθέμενη αξία στην αναπαράσταση και ανάλυση νευροφυσιολογικών σημάτων.

Η προτεινόμενη προσέγγιση αξιολογήθηκε συγκριτικά με συμβατικά χαρακτηριστικά βασισμένα στην Φασματική Πυκνότητα Ισχύος και στην τετραγωνική ενέργεια, χρησιμοποιώντας ταξινομητές Μηχανικής Μάθησης, τόσο στο Subject-Dependent, όσο και στο Subject-Independent πλαίσιο. Τα πειραματικά αποτελέσματα καταδεικνύουν ότι τα ΤΚΕΟ χαρακτηριστικά επιτυγχάνουν παραπλήσια ή ανώτερη απόδοση έναντι των μεθόδων αναφοράς, βελτιώνοντας την ακρίβεια ταξινόμησης στα προβλήματα Κινητικής Νοερής Απεικόνισης και Εντοπισμού Επιληψίας, ενώ εμφανίζουν αντίστοιχα αποτελέσματα στην Αναγνώριση Συναισθήματος.

Συνολικά, τα ευρήματα υποδεικνύουν ότι ο ΤΚΕΟ παρέχει συμπληρωματική πληροφορία σε σχέση με τα συμβατικά ενεργειακά χαρακτηριστικά, ειδικά σε περιπτώσεις, όπου τα σήματα χαρακτηρίζονται από μη γραμμικές δυναμικές, προσφέροντας έτσι έναν ερμηνεύσιμο και υπολογιστικά αποδοτικό τρόπο ενίσχυσης της ακρίβειας πρόβλεψης στην ανάλυση ΗΕΓ.

Chapter 1

Introduction

1.1 Brain Analysis Fundamentals

1.1.1 Brain Anatomy

As the primary organ of the human nervous system, the brain processes sensory information, regulates bodily functions, and enables thought, emotion, and behavior. In a typical adult, it weighs approximately 1.2–1.4 kilograms, with about 60% of its mass composed of fat. The remaining 40% consists of water, proteins, carbohydrates, and mineral salts. Although it is not a muscle, the brain contains an intricate network of blood vessels and nerves, including specialized cells such as neurons and glial cells. Protected within the skull, it is organized into major regions: the cerebrum, cerebellum, and brainstem.

The cerebrum, which constitutes the largest portion of the brain, is divided into left and right hemispheres connected by the corpus callosum. Each hemisphere mainly controls the opposite side of the body and exhibits functional specialization—for example, the left hemisphere is frequently linked to language and analytical reasoning, whereas the right hemisphere is more engaged in spatial processing and creative activities. Distinct fissures divide the cerebral hemispheres into lobes, with each hemisphere containing four: the frontal, temporal, parietal, and occipital lobes. These lobes are further subdivided into regions dedicated to specific functions, though they operate in close coordination both within and across hemispheres.

The frontal lobe is associated with higher-order executive functions, including personality, emotional control, problem-solving, certain aspects of speech, voluntary motor activity, and self-awareness. The parietal lobe processes somatosensory information such as touch, pain, and temperature and and contributes to the interpretation of language, the integration of sensory signals from multiple modalities, and the management of spatial and visual per-

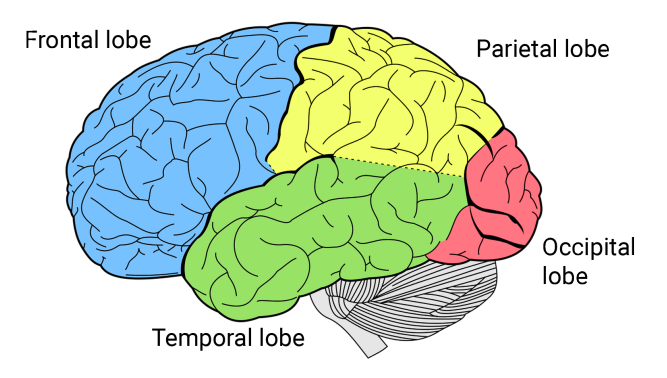


Figure 1.1 Lobes of the Brain [83].

ception. The temporal lobe is essential for auditory perception, language comprehension, memory formation, and the sequencing and organization of information. The occipital lobe is primarily responsible for processing visual stimuli, including colour, light, and motion. These lobes function interdependently, forming highly complex neural networks that support sophisticated behaviours and advanced cognitive abilities.

1.1.2 Physiology of Neurons

Neurons constitute the principal functional elements of the nervous system, specialized for rapid information transfer and processing through electrochemical signalling mechanisms. The human brain contains roughly 100 billion neurons, each potentially forming thousands of synaptic connections—adding up to an estimated 100–1,000 trillion synapses—thus creating an immensely complex communication network. Each neuron comprises three principal components: the cell body (soma), which houses the nucleus and is the primary site of protein synthesis; dendrites, tree-like branching extensions studded with dendritic spines that receive incoming information from other neurons; and a single axon, a cable-like projection that can extend from micrometers to over a meter in length in humans, transmitting electrical impulses from the soma in the direction of target cells. The axon emerges from the axon hillock, a region rich in voltage-gated sodium channels and critical for initiating electrical signals. Many axons are covered by myelin, a lipid-rich insulating layer produced by oligodendrocytes in the central nervous system and Schwann cells in the peripheral nervous system. The myelin sheath is interrupted by gaps called nodes of Ranvier, which enable rapid saltatory conduction. At the far end, axon terminals contain specialized synaptic boutons that mediate communication with other cells.

Neurons transmit signals using both electrical impulses and chemical messengers. In their resting state, neurons maintain a voltage gradient across their membrane due to selective ion distribution, primarily sodium, potassium, calcium, and chloride. When a stimulus alters this

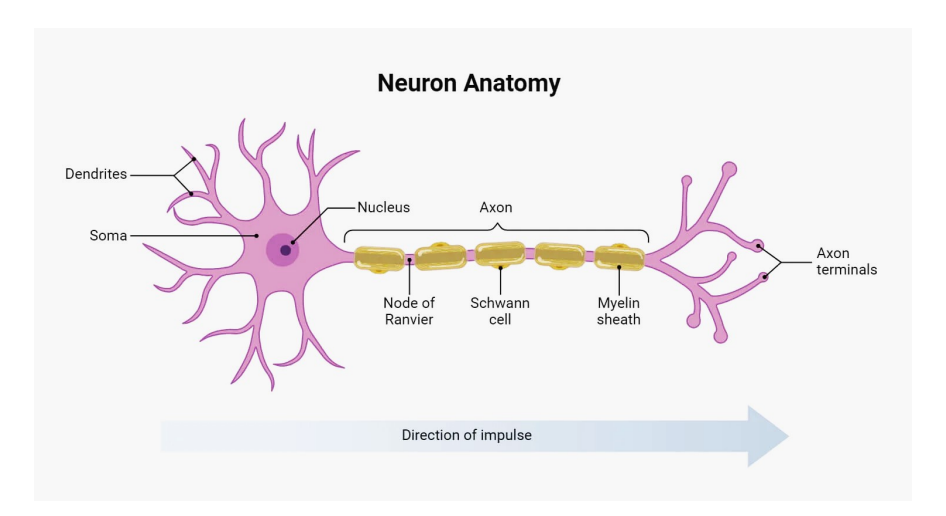


Figure 1.2 The Structure of a Neuron [99].

membrane potential beyond a threshold at the axon hillock, an Action Potential—a brief electrochemical pulse—is generated. As the signal reaches the axon terminals, it quickly induces the merging of neurotransmitter-filled vesicles with the presynaptic membrane. Neurotransmitters cross the approximately 20-nm synaptic cleft by diffusion and attach to receptors on the postsynaptic neuron, modifying the membrane's ion permeability and affecting the likelihood of Action Potential generation. Neurons themselves can be categorized according to structure—such as unipolar, bipolar, multipolar, anaxonic, and pseudounipolar forms—or by function, including afferent neurons that carry sensory input toward the central nervous system, efferent neurons that transmit motor commands away from it, and interneurons that integrate and relay information between other neurons. This transmission process—from electrical impulse to chemical signal and back again—occurs in less than two milliseconds and forms the basis of every brain function, from simple reflexes to complex cognition. Additionally, neuronal connections are dynamic; repeated activation can strengthen synapses, contributing to neuroplasticity and the brain's capacity for learning and memory.

1.1.3 Electroencephalography Signals

Electroencephalography (EEG) [101] is a non-invasive method to measure the spontaneous or induced electrical activity of the brain. EEG signals are recorded using electrodes, placed at specific locations of the scalp, which detect voltage fluctuations generated by neural activity. The 10-20 system [25], endorsed by the International Federation of Electroencephalography and Clinical Neurophysiology, is a widely adopted approach that utilizes anatomical landmarks to standardize the positioning of EEG electrodes. This system relies on establishing a relationship between electrode placement and the corresponding areas of the cerebral cortex, ensuring comprehensive coverage of all relevant brain regions. The numerical labels '10' and

'20' denote the distances between adjacent electrodes, which are either 10% or 20% of the total skull distance in the front-back or right-left directions. These distances are determined based on anatomical landmarks on the scalp: the nasion and inion for front-back direction, and the two preauricular points for right-left direction (see Fig. 1.3).

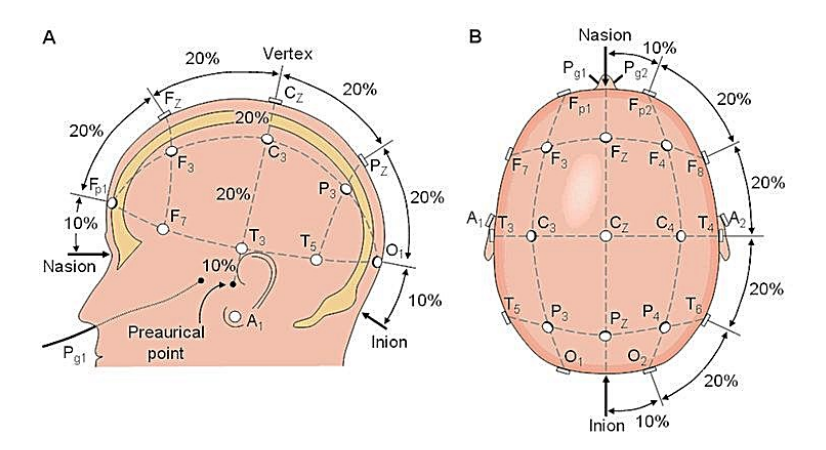


Figure 1.3 10-20 System [10]: Schematic Overview of Electrode Placement.

The neural basis of EEG lies in the coordinated activity of large populations of cortical neurons, particularly pyramidal cells in the cerebral cortex. While action potentials contribute to local electrical changes, EEG predominantly reflects postsynaptic potentials due to their longer duration and larger spatial reach. For these signals to be detectable at the scalp, many neurons need to be active at the same time and aligned in a similar direction. As the electrical currents travel from the brain through the fluid, skull, and scalp, they become spread out, a process called volume conduction. This spreading blurs the signals, which reduces the precision of the EEG and makes it hard to localize neural sources directly. Consequently, techniques such as computational modeling and integration with imaging modalities like MRI are often employed to improve source estimation.

Accurate EEG measurement also depends on electrode technology and recording systems. Conventional wet electrodes, typically silver/silver chloride (Ag–AgCl), require conductive gel or saline to reduce impedance and ensure stable signal quality. Recording setups generally include multiple active electrodes, a reference electrode, and a ground electrode, with modern high-density arrays offering up to 256 channels for improved spatial sampling [109]. These signals, initially in the microvolt range, are amplified, filtered, and digitized before storage. In the recorded data, amplitudes are represented again in microvolts. Despite technical advances, EEG remains highly sensitive to artifacts from muscle activity, eye movements, or environmental noise, requiring careful preprocessing to extract meaningful neural information.

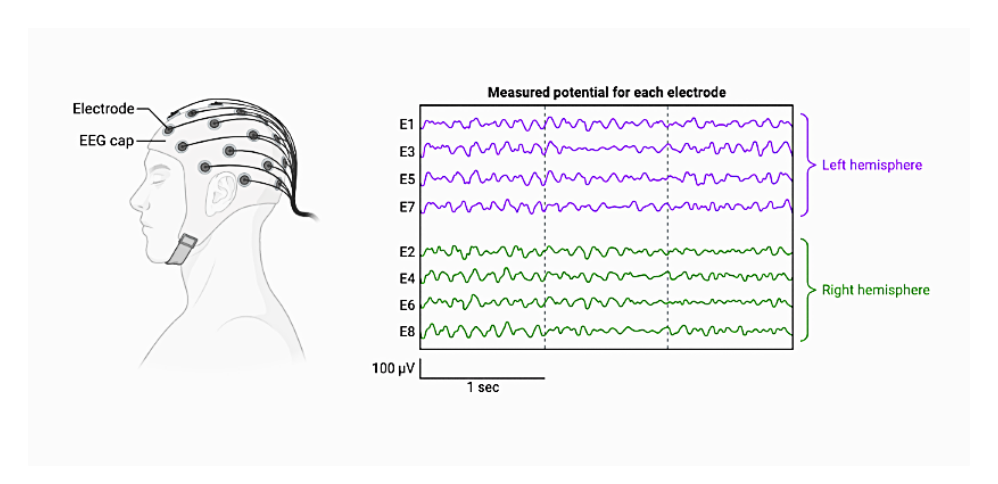


Figure 1.4 EEG Recording Setup with Representative Signals [17].

1.1.4 EEG Channels

Once electrodes are positioned according to the 10–20 system, the recorded signals are organized into channels. Each electrode is named after a letter and a number, representing its distinct location, as follows: **F**-Frontal lobe, **T**-Temporal lobe, **C**-Central lobe, **P**-Parietal lobe, and **O**-Occipital lobe, whereas even numbers refer to the right hemisphere and odd numbers to the left hemisphere of the scalp. The "Z" index refers to the electrodes on the mid-sagittal plane and is often used as a reference point. Channels can be configured in two main ways. In monopolar recordings, a single electrode serves as the reference point, while all other electrodes are compared to it. In bipolar recordings, EEG activity is captured by measuring the voltage difference between adjacent electrode pairs. The number of channels used varies depending on the application, with most modern systems ranging from 32 to 128 channels.

1.1.5 Frequency Bands

Beyond the spatial organization of electrodes into channels, EEG signals are also characterized by their temporal patterns. These patterns can be described in terms of frequency bands, which reflect different aspects of brain activity. EEG activity is typically divided into five main frequency bands [5]:

• Delta (δ) band at 0.5 Hz-3 Hz: Typically appears during deep, unconscious sleep and is considered normal in adults only during moderate to deep sleep stages. Its presence outside of these sleep stages suggests brain dysfunction. Anomalies in brain activity may manifest across all or specific channels, depending on the underlying neurological issue.

- Theta (θ) band at 4 Hz-7 Hz: Observed during some states of sleep and quiet focus. It can be classified as both a normal and abnormal activity depending on the age and state of the subject. For adults, it is considered normal during drowsiness, but it could signify neurological issues when observed in an alert state. Conversely, in younger individuals, theta activity may dominate recordings from the posterior and central regions of the scalp.
- Alpha (α) band at 8 Hz-12 Hz: Noticeable when an individual is relaxed with closed eyes yet remains awake. Alpha is a typical brain activity in adults during wakefulness, especially prominent in recordings from the posterior head channels. This activity is relatively balanced between the two hemispheres and exhibits an amplitude ranging from 40 to $100\mu V$. It's exclusive to closed-eye states and tends to diminish or vanish upon opening the eyes.
- Beta (β) band at 13 Hz-30 Hz: Appears during periods of regular awareness and focused attention. This brain activity is typical whether the eyes are open or closed and is commonly observed in recordings from the central or frontal areas of the head. Certain medications can elevate the level of beta activity in EEG recordings.
- Gamma (γ) band at 30 Hz-50 Hz: Particularly responsive to visual stimulation. It is linked to numerous sensory, emotional, and cognitive processes. During the processing of sensory data and memory-related cognitive tasks, gamma activity tends to intensify. Moreover, the heightened gamma activity observed in these tasks coincides with reduced power in other lower-frequency band signals [76].

Several additional patterns of brainwave activity exist and are more closely associated with specific conditions. For instance, spike and wave patterns are indicative of seizure disorders and might appear in EEG readings even outside of active epileptic seizures. The presence of spikes or sharp waves can aid in diagnosing various types of epilepsy.

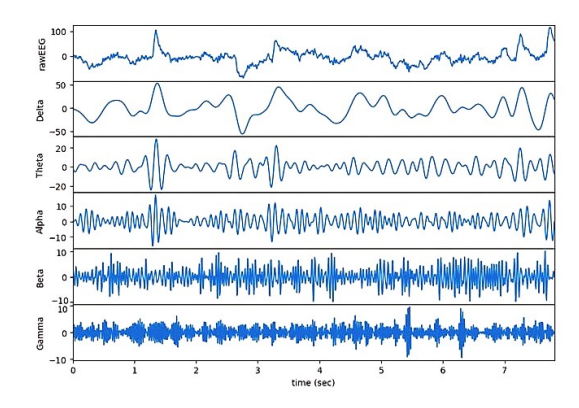


Figure 1.5 The Primary Frequency Bands of an EEG signal [14].

1.2 Theory of Emotion

While human emotions have been the subject of sustained inquiry in Psychology and Neuroscience, their underlying mechanisms and organization remain complex and, in many respects, unresolved. To better understand emotions, researchers have proposed various frameworks that aim not merely to categorize them, but to explain their structure, origins, and functions—whether through discrete classifications [37], [93], physiological theory [63], functional and behavioral analysis [33], or dimensional mapping based on affective experience [97]. These approaches reflect a broader shift from introspective models to scientific theories grounded in evolutionary biology, purposive behavior, and cognitive-affective structures, offering increasingly systematic accounts of emotional phenomena.

The James-Lange theory [63], developed by William James and Carl George Lange, presents a physiological explanation of emotion. It proposes that emotions are not the initiators of bodily changes but rather their outcome. James interpreted emotions as the conscious perception of somatic responses, while Lange attributed a central role to vascular activity, collectively asserting that emotional states emerge from autonomic physiological processes.

In his 1971 study, Paul Ekman [37] proposed a framework for categorizing facial expressions associated with discrete emotions, emphasizing their universality across cultures. Drawing on cross-cultural research, including work with preliterate populations such as the Fore people of New Guinea, Ekman identified six basic emotions—happiness, sadness, anger, fear, surprise, and disgust—that correspond to distinct facial muscle configurations. In later work, Ekman [36] suggested expanding this list to include additional candidate emotions such as awe, contempt, shame, guilt, embarrassment, and excitement, based on further evidence and theoretical considerations. This expanded framework, including a neutral category alongside the basic emotions, helped lay the groundwork for later theories on emotion recognition and classification.

James A. Russell (1980) [97] introduced a circular model of affect, proposing that emotional experiences can be systematically organized within a two-dimensional orthogonal space defined by valence and arousal. Valence reflects the degree of pleasure or displeasure associated with an emotion, while arousal captures the intensity of the emotional experience, ranging from low-energy states like sleepiness to high-energy states like excitement. Prior to this, Russell and Mehrabian (1977) [98] had identified a third, independent dimension—dominance—which captures the extent to which an individual feels in control or submissive within an emotional context, suggesting that a full description of affective states may require a three-dimensional space.

In 1982, Robert Plutchik [93] proposed a psychoevolutionary model of emotion, conceptualizing affective states within a wheel-like structure composed of eight primary emotions arranged in opposing pairs. These emotions vary in intensity and can combine to form more

complex emotional experiences, reflecting the dynamic and multidimensional nature of affect.

These theoretical frameworks provide essential foundations for understanding the structure and dynamics of human emotions. Despite their contributions, the precise mechanisms through which emotions emerge and can be systematically analyzed remain an open area of investigation. Contemporary research continues to explore methods for capturing and interpreting emotional states through physiological and neural indicators.

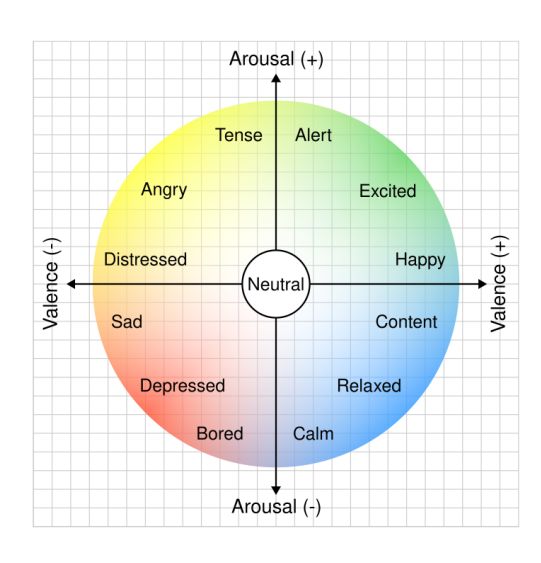


Figure 1.6.1 Valence—Arousal Space for Emotional States [79].

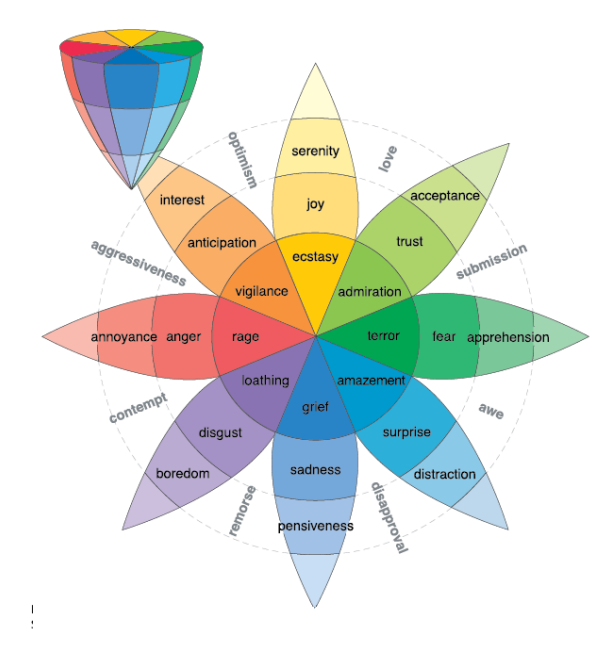


Figure 1.6.2 Plutchik's Wheel of Emotions [94].

1.3 Theory of Motor Imagery

Motor imagery (MI) refers to the mental simulation of movement without any actual physical execution. It involves creating an internal image of a motor action, usually from a first-person point of view, as if one were physically carrying out the movement [31]. During MI, the brain areas involved in planning and preparing movements are active, but the actual movement is voluntarily stopped within the corticospinal system. Evidence from behavioral and neurophysiological studies indicates that imagined and executed actions share, to some extent, common neural substrates. These include areas involved in movement programming such as the premotor cortex, anterior cingulate cortex, inferior parietal lobule, and cerebellum [31]. While motor imagery activates overlapping regions with actual execution, differences in activation patterns—particularly within the cerebellum—reflect the absence of sensory feedback during imagery [71]. This functional equivalence is further reinforced by studies

showing that the temporal dynamics of imagined movements often mirror those of real ones, and that response times during imagery follow rules like Fitts's law, which describes the relationship between movement speed and accuracy [32]. MI allows conscious access to motor plans typically involved in real execution and can even produce measurable physiological responses—such as changes in heart rate and respiration—originating from central motor processes [86]. Overall, these findings confirm that MI is a cognitive process closely connected to real motor control, laying the foundation for various applications, which are reviewed in detail in Section 3.2.

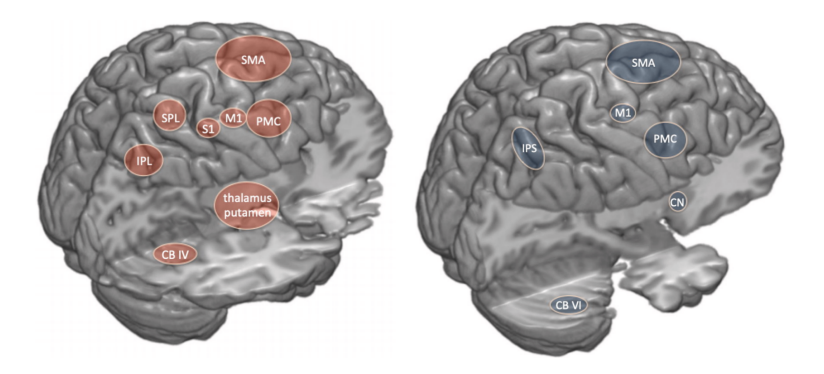


Figure 1.7 Brain Regions involved in Motor Execution (red) and Motor Imagery (blue), showing Overlapping and Distinct Activations across Cortical and Subcortical Areas [61].

1.4 Theory of Epilepsy

Epilepsy is a chronic neurological disease characterized by an enduring predisposition of the brain to generate epileptic seizures, accompanied by neurobiological, cognitive, psychological, and social consequences [39]. It may be diagnosed in individuals who experience at least two unprovoked seizures occurring more than 24 hours apart, after a single unprovoked seizure when there is a high estimated risk of future seizures ($\geq 60\%$), or upon identification of an epilepsy syndrome. Despite affecting an estimated 51 million people worldwide, a significant proportion of individuals with active epilepsy remain untreated due to a persistent treatment gap [11].

The pathophysiology of epilepsy involves abnormal hypersynchronous neuronal discharges, often resulting from disruptions in excitatory and inhibitory neurotransmission, glial function, or ion homeostasis [30]. Etiological classifications include structural, genetic, infectious, metabolic, immune, and unknown causes. Diagnostic protocols incorporate electroencephalography (EEG), which enables detection of interictal epileptiform discharges, identification of seizure onset zones, especially when coupled with advanced imaging techniques, and evaluation of treatment efficacy. A critical component of diagnosis and treatment plan-

ning involves the classification of seizures, which are primarily categorized by their mode of onset to focal, generalized and unknown [40]. Focal seizures originate in a specific region of one cerebral hemisphere and are further classified based on the patient's level of awareness during the event into focal aware seizures and focal impaired awareness seizures. They can also be categorized by their onset as motor seizures, involving movements such as clonic or tonic activity, or non-motor seizures, which include symptoms like sensory changes or altered emotions. In contrast, generalized seizures involve both sides of the brain at the onset and are subdivided into motor types (e.g., tonic-clonic, myoclonic, spasms) and non-motor types, such as typical absence seizures, characterized by brief lapses in awareness. Seizures of unknown onset are used when the beginning of the event is not observed, though these may later be classified upon further clinical or EEG evaluation.

From a clinical electrophysiological perspective, seizures are associated with distinct EEG patterns such as spikes, sharp waves, and rhythmic discharges, often classified according to frequency, morphology, and duration [106]. The progression of a seizure can be divided into five phases. The Prodromal phase occurs hours or days before the event and may involve subtle changes in mood or behavior. The Pre-ictal/Aura phase describes the period right before the event and is marked by unusual sensations or perceptual changes that can serve as a warning. The Ictal phase is the seizure itself, when abnormal brain activity leads to visible symptoms. The Interictal phase refers to the period between seizures, when the brain may still exhibit abnormal electrical activity without visible signs. Finally, the Postictal phase follows the seizure and is typically characterized by confusion, fatigue and headaches. Each phase exhibits distinct neurophysiological and behavioral features that provide critical insights into seizure onset, progression, and recovery, thereby facilitating more accurate monitoring and timely therapeutic intervention.

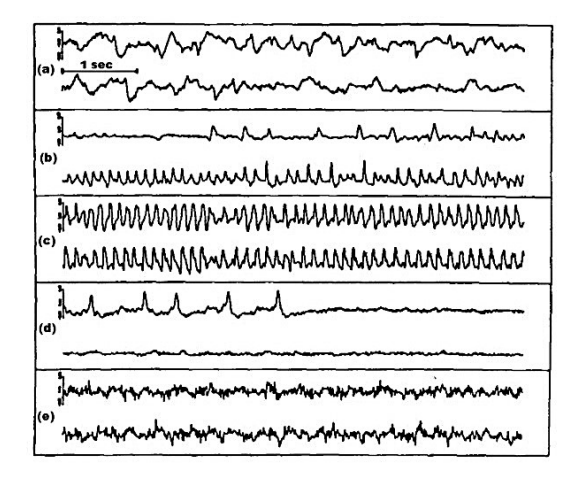


Figure 1.8 Seizure Stages [48]: (a) Pre-ictal; (b) Transition from Pre-ictal to Ictal; (c) Ictal; (d) Transition from Ictal to Postictal; (e) Postictal.

1.5 Thesis Structure & Contributions

EEG signals originate from the synchronized activity of extensive neuronal populations and manifest as oscillatory waveforms whose amplitude and frequency evolve continuously over time. These temporal fluctuations mirror rapid, state-dependent variations in neural dynamics, reflecting the inherently non-stationary nature of brain electrical activity. Modeling EEG as an Amplitude–Frequency Modulated (AM–FM) process therefore provides a physiologically grounded framework for characterizing the temporal evolution of cortical oscillations and for capturing subtle modulations in brain states across different experimental conditions [84].

This Thesis aims to provide further insights into the analysis of brain electrical signals under different experimental conditions. Building upon the AM–FM modeling framework, we investigate the spectral components of neural activity through appropriate signal decomposition techniques, enabling the isolation of physiologically meaningful oscillatory modes and the extraction of energy-related features to characterize relevant brain dynamics. These representations are systematically evaluated using established machine learning approaches to explore their correspondence with diverse cognitive and clinical tasks. The remainder of this Thesis is organized into 4 chapters, each described below.

- Chapter 2 presents the theoretical foundations underlying this work, encompassing signal processing, the Teager–Kaiser Energy Operator, and machine learning methodologies. In particular, it reviews fundamental properties of signals and systems, provides a comprehensive discussion of the Teager–Kaiser Energy Operator, and outlines the principles of supervised classification algorithms.
- In Chapter 3, we design a feature extraction pipeline based on the Teager–Kaiser Energy Operator to investigate the extent to which the derived descriptors capture emotional, cognitive, and pathological (epileptic) information. Furthermore, we establish the experimental settings and evaluation protocols employed for their assessment.
- Chapter 4 reports the experimental studies conducted across three paradigms: Emotion Recognition, Motor Imagery and Epilepsy Detection. In this context, Epilepsy Detection refers to the binary classification problem of discriminating between epileptic and non-epileptic patients. The results highlight the effectiveness of the Teager–Kaiser Energy Operator as a feature extraction framework for capturing EEG dynamics, particularly in tasks characterized by well-established transient dynamics.
- Chapter 5 summarizes the main findings of this work, draws general conclusions regarding the proposed methodologies and their applicability, and outlines potential directions for future research.
- In the **Appendices**, we provide information for the four datasets employed in this study and include a list of papers produced during the course of the Thesis.

Our contributions can be summarized as follows:

- We motivate and extract a comprehensive set of EEG features derived from instantaneous energy analysis using Teager-Kaiser Energy Operator (TKEO).
- We introduce a systematic evaluation of TKEO-derived features against conventional PSD-based energy and squared-energy features across four representative EEG benchmarks.
- We examine the influence of spectral resolution on TKEO-based features through the use of different filterbank configurations.
- We provide empirical evidence of the conditions under which TKEO features outperform and/or yield complementary insights over alternative energy measures, particularly in tasks including transient and non-linear dynamics.

Chapter 2

Theoretical Background

2.1 Signal Processing Fundamentals

Signal processing is a discipline that focuses on the analysis, representation, and modification of signals to facilitate the extraction or enhancement of the information they convey [87]. Depending on the application, this may involve tasks such as isolating individual signals from a mixture, emphasizing particular features of interest, or estimating parameters that describe an underlying signal model. In communication systems, for example, signals typically undergo a series of preprocessing operations—such as modulation, conditioning, or compression—before transmission, while the receiver performs the corresponding postprocessing to recover the transmitted information as accurately as possible. Within this broad field, *Digital Signal Processing (DSP)* has emerged as a widely used and well-established approach, operating on discretely sampled signals using digital computation.

Within this context, signal processing tasks can be categorized according to their objectives. Some tasks focus on transforming input signals to generate modified or derived outputs, while others aim to extract information or characterize the signals without necessarily producing a new output. The latter class, often referred to as signal interpretation, emphasizes analyzing a signal to derive meaningful information or a description of its underlying structure, rather than producing another signal as output. For instance, in biomedical signal analysis, the objective might be to interpret an electroencephalogram (EEG) to extract clinically relevant information, such identification of specific brain activity patterns. These systems generally include digital preprocessing, which may include operations such as noise reduction, filtering, and extraction of relevant characteristics, and are then followed by computational methods—such as classification or pattern analysis—to produce quantitative metrics or symbolic information that can support diagnosis, monitoring, or subsequent interpretation.

At the core of signal processing are two fundamental concepts: **signals**, which represent information, and **systems**, which operate on these signals to produce transformations or extract information.

2.1.1 What is a Signal?

According to Oppenheim et al. [87] "the term *signal* is generally applied to something that conveys information". In a technical context, signals encode data regarding the dynamics, state, or behavior of physical systems. They can be deliberately generated to transmit information, enabling interactions in human communication, automated systems, or human–machine interfaces, while also providing essential input for system observation, control, and decision-making in both engineered and natural environments.

Continuous-time signals, often referred to as analog, are defined over a continuous range of time, meaning their independent variable varies continuously. Discrete-time signals are defined only at specific time instances, so their independent variable assumes discrete values; mathematically, they are represented as sequences of numbers. In addition to the temporal domain, the amplitude of a signal can also be either continuous or discrete. When both the time samples and the amplitude levels are quantized, the resulting signals are classified as digital signals.

2.1.2 What is a System?

A discrete-time system is a system for which both input and output signals are discrete-time signals. Mathematically, such a system can be described as a transformation or operator $T\{\cdot\}$ that maps an input sequence x[n] to an output sequence y[n], expressed as $y[n] = T\{x[n]\}$. Different classes of systems are distinguished by imposing specific conditions on the properties of the transformation $T\{\cdot\}$. The fundamental characteristics used to describe discrete-time systems include **memory**, which indicates whether the output depends only on the current input or also on past or future inputs; **linearity**, which determines whether the system obeys the principle of superposition; **time-invariance**, which specifies whether a shift in the input produces a corresponding shift in the output; **causality**, which indicates whether the output depends solely on past and present inputs; and **stability**, expressed in terms of bounded-input bounded-output (BIBO) behavior, meaning that every bounded input produces a bounded output.

2.1.3 Fourier Analysis

In signal analysis, a function can be interpreted as an element of a vector space, where different basis functions allow alternative representations. The Fourier Transform (FT)

provides the most widely used decomposition, expressing a continuous-time signal x(t) as a superposition of complex exponentials:

$$X(\omega) = \int_{-\infty}^{\infty} x(t) e^{-j\omega t} dt$$

$$x(t) = \frac{1}{2\pi} \int_{-\infty}^{\infty} X(\omega) e^{j\omega t} d\omega$$

In practice, signals are usually discrete and of finite length. In this case, the **Discrete** Fourier Transform (DFT) is employed, mapping an N-point sequence x[n] to its spectral coefficients:

$$X[k] = \sum_{n=0}^{N-1} x[n] e^{-j\frac{2\pi}{N}kn}, \quad k = 0, 1, \dots, N-1$$

The DFT samples the spectrum at N equally spaced frequency bins, with spacing $\frac{1}{NT}$ between adjacent frequencies, where T denotes the sampling interval; the k-th bin corresponds to the natural frequency $f = f_s(k/N)$, where f_s denotes the sampling frequency. In practice, zero-padding or truncation is often applied when computing an M-point DFT with $M \neq N$. Since the analysis is based on a finite-duration sequence, the resulting spectrum is inherently periodic, which is why it is customary to visualize the DFT over the discrete frequency index range [0, N-1]. The computation of the DFT is typically performed using the **Fast Fourier Transform (FFT)** [27], an algorithm that reduces the computational complexity from $O(N^2)$ to $O(N \log N)$.

The Fourier Transform is fundamental in signal processing because it reveals the frequency content of a signal, indicating which frequencies are present and with what amplitudes. This frequency-domain view greatly simplifies tasks such as filtering, compression, and feature extraction, making it indispensable in applications from communications and audio processing to biomedical engineering.

2.1.4 Energy and Power of a Signal

In signal processing, the energy E_x of a continuous-time signal x(t) is defined as the integral of the squared magnitude of the signal over all time, i.e.,

$$E = \int_{-\infty}^{\infty} |x(t)|^2 dt$$

The instantaneous power P(t) and the average power P of a continuous-time signal are defined as

$$P(t) = |x(t)|^2$$

$$P = \lim_{T \to \infty} \frac{1}{2T} \int_{-T}^{T} |x(t)|^2 dt$$

For a discrete-time signal x[n], the definitions are analogous:

$$E = \sum_{n = -\infty}^{\infty} |x[n]|^2$$

$$p[n] = |x[n]|^2$$

$$P = \lim_{N \to \infty} \frac{1}{2N+1} \sum_{n=-N}^{N} |x[n]|^2$$

In addition to the time-domain definitions, the energy of a signal can also be expressed in the frequency domain. This relationship is established by *Parseval's theorem*, which states that the total energy of a signal in the time domain equals its total energy in the frequency domain. For a continuous-time signal with Fourier transform $X(\omega)$:

$$\int_{-\infty}^{\infty} |x(t)|^2 dt = \frac{1}{2\pi} \int_{-\infty}^{\infty} |X(\omega)|^2 d\omega$$

For a finite-length discrete-time signal of length N with discrete Fourier transform (DFT) X[k]:

$$\sum_{n=0}^{N-1} |x[n]|^2 = \frac{1}{N} \sum_{k=0}^{N-1} |X[k]|^2$$

Power Spectral Density

The Power Spectral Density (PSD) characterizes how the power of a signal or a random process is distributed across different frequencies and is widely used in biosignal analysis [16]. Mathematically, it is defined as:

$$S_{xx}(\omega) = \int_{-\infty}^{\infty} R_{xx}(\tau) e^{-j\omega\tau} d\tau,$$

Where x(t) is a stationary signal, and $R_{xx}(\tau)$ is its autocorrelation function. The autocorrelation measures the similarity between the signal and a time-shifted version of itself at lag τ .

By taking the Fourier Transform of the autocorrelation, we convert this time-domain measure of self-similarity into a frequency-domain representation. This reveals how the signal's power is distributed across frequencies. Peaks in the autocorrelation correspond to lags where the signal closely resembles a delayed copy of itself, and regularly spaced peaks indicate strong periodic components. The Fourier Transform of these patterns highlights the corresponding spectral contributions, which together define the PSD.

In practice, however, the PSD is typically estimated using the DFT of the signal:

$$P[k] = \frac{1}{N} |X[k]|^2.$$

Both definitions are equivalent under the Wiener–Khinchin theorem, but the former highlights the conceptual foundation, while the latter is more convenient for implementation and numerical analysis.

2.1.5 Signal Filtering

Signal filtering refers to the process of suppressing unwanted components of a signal while preserving the features of interest. Since many signal characteristics are most effectively represented in the frequency domain, filtering is typically described and analyzed in terms of frequency response.

Convolution

Linear time-invariant (LTI) systems, which include most filters, can be completely characterized by their impulse response. The output of such a system is obtained by convolving the input signal with the system's impulse response. Therefore, convolution provides the fundamental mathematical operation underlying filtering and many other signal transformations.

The convolution of two functions f and g is denoted by $f \star g$, where the operator \star signifies convolution. For continuous-time signals, it is defined as the integral of the product of the two functions, after one is reflected about the y-axis and shifted:

$$(f * g)(t) = \int_{-\infty}^{\infty} f(\tau) g(t - \tau) d\tau$$

For discrete-time signals, convolution is defined as a sum over all time indices:

$$(f * g)[n] = \sum_{k=-\infty}^{\infty} f[k] g[n-k]$$

In the context of filtering, f typically represents the input signal, while g represents the impulse response of the filter. The convolution operation thus produces the filtered output, capturing the effect of the system on the input.

An important property of convolution is its relationship with the Fourier transform: convolution in the time domain corresponds to multiplication in the frequency domain,

$$(f * g)(t) \stackrel{\mathcal{F}}{\longleftrightarrow} F(\omega) G(\omega)$$

This equivalence explains why filtering can also be interpreted as shaping a signal's spectrum according to the filter's frequency response.

Main types of Filters

With this foundation, filters can be categorized based on their magnitude response. The main types of filters, along with their idealized behaviours, are outlined below:

- Low-pass filters: Allow low-frequency components while attenuating high frequencies.
- **High-pass filters:** Allow high frequencies while removing low-frequencies.
- Band-pass filters: Allow signals within a specific frequency range while rejecting components outside this band.
- Band-Stop filters: Attenuate signals within a defined frequency band while allowing frequencies outside this band to pass. A band-stop response can be realized by combining a low-pass and a high-pass filter in parallel and summing their outputs.
- Notch filters: A special case of band-stop filters characterized by a very narrow stopband, typically used to suppress narrowband interference such as power line noise at 50/60 Hz.

Gabor Filter

The Gabor filter is a linear (LTI) filter widely used in signal and image processing because it can simultaneously capture information in both the spatial (or temporal) and frequency domains. In one dimension, the Gabor filter is mathematically expressed as:

$$g(t) = \exp\left(-\frac{t^2}{2\sigma^2}\right)\cos(2\pi f_c t + \phi)$$

where σ it the standard deviation of the Gaussian envelope, controlling its temporal spread, f_c is the central frequency of the filter, and ϕ is the phase offset.

The frequency response of the Gabor filter can be expressed as:

$$G(f) = \frac{\sigma\sqrt{2\pi}}{2} \left[\exp(-2\pi^2\sigma^2(f - f_c)^2) e^{j\phi} + \exp(-2\pi^2\sigma^2(f + f_c)^2) e^{-j\phi} \right]$$

From a signal processing perspective, the Gabor filter can be viewed as a band-pass filter with adjustable parameters. The Gaussian envelope governs the extent of temporal localization, while the sinusoidal carrier defines the central frequency to which the filter is most sensitive. This property allows the filter to selectively respond to signal components that match its

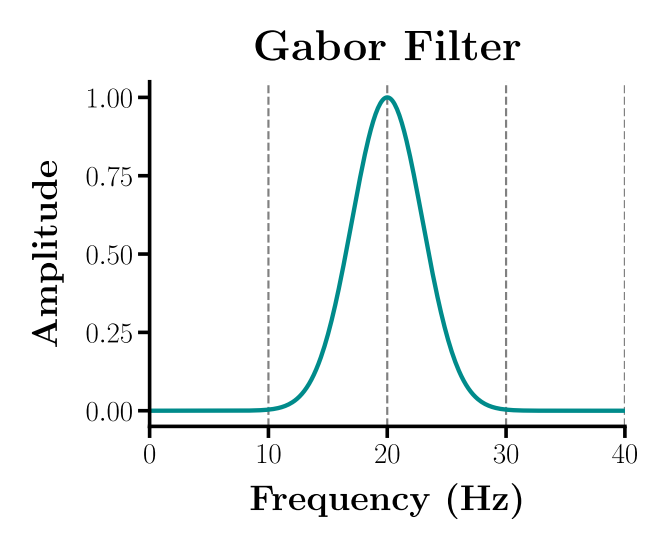


Figure 2.1 Normalized Frequency Response of a 1D Gabor Filter.

frequency and phase characteristics. In one dimension, the Gabor filter is commonly applied to extract local frequency and phase information, which is valuable in areas such as speech and biomedical signal analysis. In two dimensions, it is widely used in image processing tasks, including texture analysis [35] and edge detection [50].

Gabor Filterbank

A Gabor filterbank is constructed by generating a sequence of Gabor filters whose center frequencies are distributed between a lower (f_{low}) and an upper (f_{high}) cutoff frequency. In this way, the broadband signal is decomposed into subbands, each filter capturing localized spectral content around its center frequency. In the implementation, the frequency step is defined as:

$$\Delta f = \frac{f_{\text{high}} - f_{\text{low}}}{N},$$

where N is the number of filters. The center frequencies are then:

$$f_{\rm c}(k) = f_{\rm low} + k\Delta f,$$

where $k \in \mathbb{Z}_{>0} : k < N$.

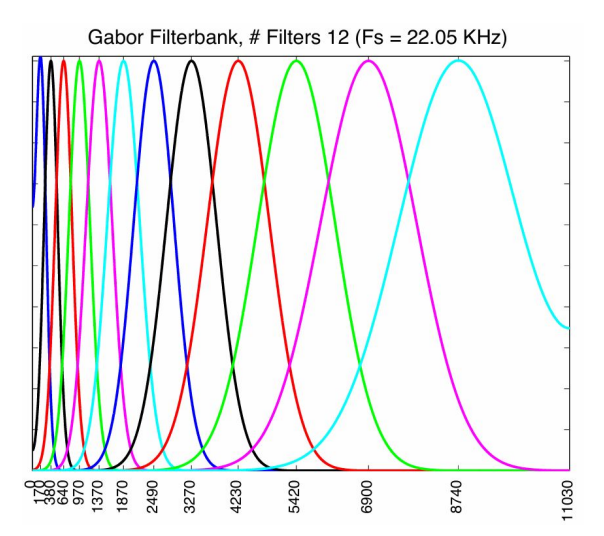


Figure 2.2 Gabor Filterbank Consisting of 12 Mel-Spaced Filters with 50% Overlap (Sampling Rate = 22.05 kHz) [123].

2.1.6 Signal Decomposition

Decomposition is a fundamental step in signal processing that allows complex signals to be expressed as combinations of simpler components, such as in the FT (Section 2.1.3). This process helps in identifying meaningful patterns and separating sources of interest from noise. In EEG analysis, decomposition is particularly important for isolating neural activity from artifacts.

Independent Component Analysis

Independent Component Analysis (ICA) [26] is a statistical decomposition algorithm that separates a multivariate signal into additive, statistically independent components. It is widely used for blind source separation [81], where the goal is to recover original source signals from their mixtures without prior knowledge of their structure. ICA assumes that the observed signals are linear mixtures of independent, non-Gaussian sources.

Mathematically [26], the ICA of a random vector $\mathbf{y} \in \mathbb{R}^m$ consists of finding a linear transformation that minimizes the statistical dependence between its components. Assume the following linear, noise-free statistical model:

$$y = Fz$$
,

where $\mathbf{z} = [z_1, z_2, \dots, z_n]^{\top}$ is a random vector whose components are statistically independent, and $\mathbf{F} \in \mathbb{R}^{m \times n}$ is an unknown full-rank *mixing matrix*.

The problem set by ICA is to estimate both \mathbf{F} and the corresponding realizations of the sources \mathbf{z} , given only realizations of \mathbf{y} . Since the decomposition is indeterminate up to scaling and permutation, if $\{\mathbf{F}, \mathbf{A}\}$ is an ICA of \mathbf{y} , then so is $\{\mathbf{F}', \mathbf{A}'\}$ with

$$\mathbf{F}' = \mathbf{F} \bar{\mathbf{\Lambda}} \mathbf{D} \mathbf{P}, \qquad \mathbf{A}' = \mathbf{P}^{\top} \bar{\mathbf{\Lambda}}^{-1} \mathbf{A} \mathbf{P},$$

where $\bar{\Lambda}$ is diagonal and invertible, **D** is diagonal with unit-modulus entries, and **P** is a permutation matrix.

The ICA is uniquely defined (up to scale and permutation) if at most one component of \mathbf{z} is Gaussian. In this case, there exists a demixing matrix $\mathbf{W} \in \mathbb{R}^{n \times m}$ such that

$$z = Wy$$

whose components are as statistically independent as possible.

A suitable contrast function \mathcal{J} is used to measure the degree of statistical dependence among components of \mathbf{z} . A theoretically valid choice is the (negative) mutual information,

$$\mathcal{J}(\mathbf{z}) = -I(p_{\mathbf{z}}) = -\int p_{\mathbf{z}}(\mathbf{u}) \log \frac{p_{\mathbf{z}}(\mathbf{u})}{\prod_i p_{z_i}(u_i)} d\mathbf{u},$$

which vanishes if and only if the components z_i are mutually independent.

In practice, mutual information can be approximated using measures of *non-Gaussianity*, since Gaussian variables maximize entropy among variables of equal variance. A common criterion is based on the *negentropy*,

$$J(p_{z_i}) = S(p_{z_i}^{G}) - S(p_{z_i}),$$

where $S(\cdot)$ denotes the differential entropy and $p_{z_i}^{G}$ is a Gaussian density with the same mean and variance as p_{z_i} . Hence, the ICA estimation problem can be expressed as

$$\max_{\mathbf{W}} \sum_{i=1}^{n} J(p_{z_i}),$$

that is, to find a demixing matrix \mathbf{W} yielding components $\mathbf{z} = \mathbf{W}\mathbf{y}$ of maximal non-Gaussianity, thereby ensuring their statistical independence.

In practice, the FastICA algorithm [47] is often used due to its computational efficiency, employing a fixed-point iteration to maximize non-Gaussianity via an approximation of negentropy.

In EEG analysis, ICA is especially useful for detecting and removing artifacts such as eye blinks, heartbeats, and muscle activity [53], as these sources are generally independent from neural signals. ICA can also help in isolating functionally distinct neural components for further analysis.

2.1.7 Biosignals

Biosignals [82] are measurable signals originating from biological systems that convey information about physiological processes and functions. They can be broadly classified into two primary categories: electrical and non-electrical signals. Common examples of biosignals include:

- Electroencephalogram (EEG): Measures electrical activity of the brain.
- Electrocardiogram (ECG/EKG): Records the electrical activity of the heart.
- Electromyogram (EMG): Captures the electrical activity produced by skeletal muscles during contraction and relaxation.
- Electrooculogram (EOG): Monitors eye movements by measuring the corneo-retinal standing potential between the front and back of the eye.
- Galvanic Skin Response (GSR): Measures changes in the skin's electrical conductance.
- Respiration rate
- Body temperature
- Pulse rate

Preprocessing of biosignals constitutes a critical step in biomedical signal analysis, as these signals are often characterized by low amplitudes and a high susceptibility to noise and artifacts. Signal processing techniques enable the amplification, filtering, and transformation of biosignals to extract meaningful information, such as spectral components, temporal dynamics, or statistical features. These processed signals have widespread applications in clinical and medical domains [107], supporting diagnostic, prognostic, and patient monitoring tasks. Beyond healthcare, biosignal analysis is increasingly employed in industrial and human—machine interaction contexts. For instance, driver vigilance monitoring systems utilize biosignals to assess alertness levels, thereby enhancing safety. Moreover, multimodal approaches that integrate multiple biosignals (e.g., EEG, ECG, respiration) are employed in advanced applications such as emotion recognition systems.

2.2 Teager-Kaiser Energy Operator

Almost all communication systems encounter oscillatory patterns characterized by both amplitude modulation (AM) and frequency modulation (FM). To detect modulations in these AM-FM signals, a nonlinear differential operator, known as the Teager-Kaiser Energy Operator (TKEO) ([54], [74]), which estimates the product of their time-varying amplitude and

frequency, can be employed. TKEO was developed for both continuous (Ψ_c) and discrete (Ψ_d) signals and is intended to function as an "energy tracker", enabling the modeling of energy variations within the signals.

$$\Psi_c[x(t)] = (\dot{x}(t))^2 - x(t)\ddot{x}(t)$$

$$\Psi_d[x[n]] = x^2[n] - x[n-1]x[n+1]$$

As Kaiser explained [54], in simple harmonic motion, the signal energy is classically understood to be proportional to the square of both amplitude and frequency.

$$E = \frac{1}{2}m\omega^2 A^2 \propto \omega^2 A^2$$

Despite this fundamental relationship, prior energy calculation methodologies often overlooked the frequency component, emphasizing solely the amplitude factor. Given a simple oscillatory signal $x[n] = A\cos(\Omega n + \phi)$, Kaiser showed that:

$$x^2[n]-x[n+1]x[n-1]=A^2sin^2(\Omega)\approx A^2\Omega^2$$

for small values of Ω . To ensure the accuracy of this approximation within acceptable bounds, Kaiser suggested constraining the value of Ω within the range $[0, \frac{\pi}{4}]$, thereby maintaining a relative error below 11%. Thus, in order to consider this operator as a reliable measure of signal energy, it necessitates the sampling of at least two points within each quarter cycle with respect to the sinusoidal oscillation.

2.2.1 Energy Separation Algorithm

For the purpose of extracting the amplitude envelope and instantaneous frequency of AM-FM signals, the Energy Separation Algorithm (ESA) [74] was developed. ESA employs nonlinear combinations of instantaneous signal outputs from the energy operator to distinguish between the amplitude modulation and frequency modulation components within its output energy product.

CESA

The Continuous Energy Separation Algorithm (CESA) was introduced for continuous-time signals. CESA offers estimates of the time-varying instantaneous frequency signal $\omega_i(t) \geq 0$ and of the amplitude envelope |a(t)| as follows:

$$\omega_i(t) = \sqrt{\frac{\Psi[\dot{x}(t)]}{\Psi[x(t)]}}$$

$$|a(t)| = \frac{\Psi[x(t)]}{\sqrt{\Psi[\dot{x}(t)]}}$$

DESA

The Discrete Energy Separation Algorithm (DESA) was developed for discrete-time signals and is divided into three categories of algorithms: DESA-1a, DESA-1, and DESA-2. As referred to in [74], DESA-2 stands out as the fastest among the three DESAs, and its mathematical analysis is the most straightforward. DESA-1a exhibits inferior performance compared to the other two, while DESA-1 demonstrates slightly better performance than DESA-2, with the variance in their performance within range 0.01% - 0.1%. Subsequently, we present the formulas of each algorithm, referring to the amplitude envelope as |a[n]| and to the instantaneous frequency as Ω_i .

DESA-1a Here '1' implies the approximation of derivatives with a single sample difference and 'a' refers to the usage of asymmetric difference.

$$\Omega_i[n] \approx arccos \left(1 - \frac{\Psi[x[n] - x[n-1]]}{2\Psi[x[n]]}\right)$$

$$|a[n]| \approx \sqrt{\frac{\Psi[x[n]]}{1 - \left[1 - \frac{\Psi[x[n] - x[n-1]]}{2\Psi[x[n]]}\right]^2}}$$

DESA-1 The effect of Ψ on asymmetric derivatives is partially balanced by averaging its effect on two opposing asymmetric derivatives, resulting in a partial "symmetrization".

$$y[n] = x[n] - x[n-1]$$

$$\Omega_i[n] \approx \arccos\left(1 - \frac{\Psi[y[n] + y[n+1]]}{4\Psi[x[n]]}\right)$$

$$|a[n]| \approx \sqrt{\frac{\Psi[x[n]]}{1 - \left[1 - \frac{\Psi[y[n] + y[n+1]]}{4\Psi[x[n]]}\right]^2}}$$

The frequency estimation component functions effectively when $0 < \Omega_i[n] < \pi$, as the principal value range of the $\arccos(v)$ function assumes that $v \in [0, \pi]$. Consequently, DESA-1 is capable of estimating instantaneous frequencies up to $\frac{1}{2}$ of the sampling frequency.

DESA-2 This DESA uses symmetric differences. Here '2' implies the approximation of first-order derivatives by differences between samples whose time indices differ by 2.

$$\Omega_i[n] \approx \frac{1}{2}\arccos\left(1 - \frac{\Psi[x[n+1] - x[n-1]]}{2\Psi[x[n]]}\right)$$
$$|a[n]| \approx \frac{2\Psi[x[n]]}{\sqrt{\Psi[x[n+1] - x[n-1]]}}$$

The frequency estimation part assumes that $0 < \Omega_i[n] < \frac{\pi}{2}$.

2.2.2 Applying Filterbanks on TKEO

TKEO provides reliable instantaneous energy estimates primarily when applied to narrow-band signals [74]. To apply this premise, the use of filterbanks helps decompose the broadband (raw) signal into localized frequency subbands, which, as a result, produces smoother instantaneous amplitude and frequency modulations [34]. Among possible choices, Gabor filters are particularly suitable due to their joint time–frequency resolution and compactness [74].

As described in Section 2.1.5, the Gabor filterbank is constructed by defining a sequence of filters with center frequencies between the lower and upper cutoff limits. In this work, the center frequencies computed are uniformly spaced. Once the set of central frequencies, f_c , has been determined, each signal is filtered with the corresponding Gabor filters, and TKEO is applied to each filter's output. This results in N energy signals, one for each subband. For each TKEO signal, we compute the temporal mean as a measure of the average sub-band energy. The filterbank that yields the maximum mean TKEO value is then selected. The corresponding filtered signal is retained for further analysis, as it represents the sub-band in which the TKEO provides the most informative characterization of the signal dynamics.

2.3 Machine Learning Models

Artificial intelligence (AI) refers to technologies engineered to imitate human mental functions, including comprehension, learning, analytical problem-solving, autonomous decision-making, and creative thinking. AI-enabled systems and applications are capable of learning from new experiences and data, recognizing objects, interpreting and responding to human language, performing tasks independently without human intervention—smart home assistants being a notable example.

Machine learning (ML) is a core subset of AI that enables systems to make predictions or decisions by learning from training data. Rather than being explicitly programmed for

every task, ML algorithms analyze examples to recognize patterns, infer insights, and improve their performance over time. Each ML technique—such as Support Vector Machines, Linear Regression, Decision Trees, Random Forests, k-Nearest Neighbors, k-Means Clustering—is particularly effective for specific types of problems and datasets.

Supervised learning is a fundamental paradigm in ML, where a model is trained using labeled data. Each input is paired with a corresponding target output (label). The primary goal for the algorithm is to learn the relationship between the inputs and the outputs, enabling accurate predictions on new, *unseen* data. Supervised learning problems are generally categorized into two types: (1) classification, which involves predicting discrete labels, and (2) regression, which involves predicting continuous values.

2.3.1 Support Vector Machines

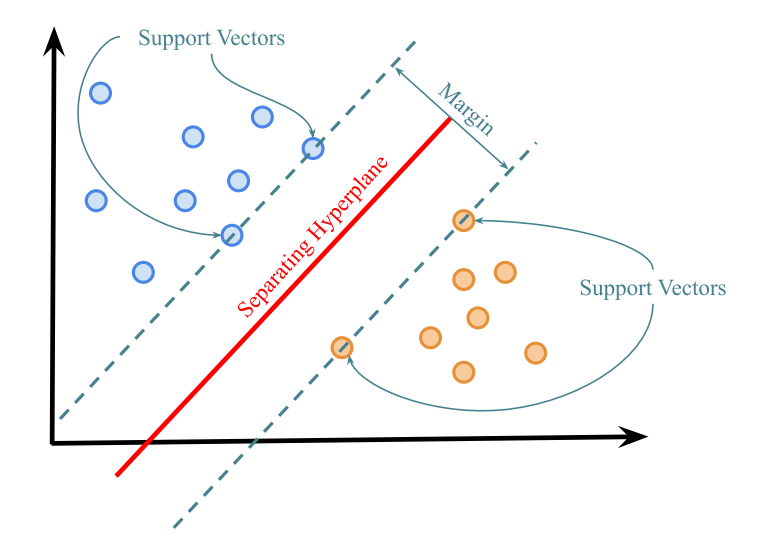


Figure 2.3 Illustration of a Linear SVM showing the optimal separating hyperplane, support vectors, and margin between two classes.

Support Vector Machines (SVMs) [28] are supervised learning models designed for binary classification that embody a simple but powerful principle: rather than merely finding any decision boundary that separates classes, they seek the *optimal* one. The optimal hyperplane is defined as that which separates the training data with the largest possible margin, i.e. the maximum distance between the boundary and the closest data points from each class (Fig. 2.4). These critical samples, called *support vectors*, alone determine the classifier. Intuitively, this margin maximization strategy reduces the chance of overfitting and yields robust generalization to unseen data.

Formally, let a training set $\{(\mathbf{x}_i, y_i)\}_{i=1}^{\ell}$ be given, where $x_i \in \mathbb{R}^d$ and labels $y_i \in \{-1, +1\}$. The data are linearly separable if there exists a vector \mathbf{w} and bias b such that

$$y_i \cdot (\mathbf{w} \cdot \mathbf{x}_i + b) \ge 1, \quad i = 1, \dots, \ell.$$

The optimal separating hyperplane is then

$$\mathbf{w}_0 \cdot \mathbf{x} + b_0 = 0.$$

Among all possible separating hyperplanes, the optimal one maximizes the margin between the two classes. The margin can be expressed as

$$p(\mathbf{w}, b) = \min_{\{\mathbf{x}: y_i = +1\}} \frac{\mathbf{x} \cdot \mathbf{w}}{\|\mathbf{w}\|} - \max_{\{\mathbf{x}: y_i = -1\}} \frac{\mathbf{x} \cdot \mathbf{w}}{\|\mathbf{w}\|}.$$

The margin at the optimal hyperplane (\mathbf{w}, b) is expressed:

$$\rho(\mathbf{w}_0, b_0) = \frac{2}{\|\mathbf{w}_0\|}.$$

As support vectors, the vectors \mathbf{x}_i , where $y_i \cdot (\mathbf{w} \cdot \mathbf{x}_i + b) = 1$ are defined.

At the optimum, the weight vector is expressed as a linear combination of support vectors:

$$\mathbf{w}_0 = \sum_{i=1}^{\ell} y_i \alpha_i^0 \mathbf{x}_i,$$

where $\alpha_i^0 \geq 0$. The vector of parameters $\mathbf{A}_0^T = (\alpha_1^0, ..., \alpha_l^0)$ is calculated by solving the quadratic programming problem:

$$\max_{\mathbf{A}} W(\mathbf{A}) = \mathbf{A}^T \mathbf{1} - \frac{1}{2} \mathbf{A}^T \mathbf{D} \mathbf{A},$$
subject to $\mathbf{A} \ge 0$,
 $\mathbf{A}^T \mathbf{y} = 0$,

where $\mathbf{1}^T = (1, ..., 1)$ and $\mathbf{D} = y_i y_j (\mathbf{x}_i \cdot \mathbf{x}_j), \quad i, j = 1, ..., \ell$.

The optimal weight vector can be expressed as a linear combination of the training samples,

$$\mathbf{w}_0 = \sum_{i=1}^N \alpha_i y_i \mathbf{x}_i.$$

Thus, the linear decision function becomes

$$f(x) = \operatorname{sign}(\mathbf{w}_0 \cdot \mathbf{x} + b_0) = \operatorname{sign}\left(\sum_{i=1}^N \alpha_i y_i (\mathbf{x}_i \cdot \mathbf{x}) + b_0\right).$$

When data are not linearly separable, the above framework is extended through soft margins. Slack variables $\xi_i \geq 0$ are introduced, relaxing the constraints to

$$y_i(\mathbf{w} \cdot \mathbf{x}_i + b) \ge 1 - \xi_i$$

and the optimization objective is modified to penalize violations:

$$\min_{\mathbf{w},b,\xi} \left\{ \frac{1}{2} \|\mathbf{w}\|^2 + C \sum_{i=1}^{\ell} \xi_i \right\},\,$$

where C > 0 controls the trade-off between maximizing the margin and minimizing classification errors.

More importantly, real-world data are often not linearly separable in the original feature space. To address this, SVMs employ a nonlinear mapping $\phi : \mathbb{R}^d \to \mathcal{H}$, where \mathcal{H} is a Hilbert space. Instead of computing $\phi(\mathbf{x})$ explicitly, the kernel trick is applied: dot-products in \mathcal{H} are replaced by a kernel function

$$\phi(\mathbf{x}) \cdot \phi(\mathbf{z}) = K(\mathbf{x}, \mathbf{z}).$$

The decision function thus generalizes to

$$f(x) = \operatorname{sign}\left(\sum_{i=1}^{\ell} y_i \alpha_i K(\mathbf{x}, \mathbf{x}_i) + b\right).$$

A widely adopted choice is the **Radial Basis Function (RBF) kernel**, defined as

$$K(\mathbf{x}, \mathbf{z}) = \exp\left(-\frac{\|\mathbf{x} - \mathbf{z}\|^2}{2\sigma^2}\right),$$

where σ is the kernel width (bandwidth) parameter that controls the spread of the RBF kernel. A larger σ leads to a smoother decision boundary, while a smaller σ allows the model to capture finer details but risks overfitting. The RBF kernel allows the SVM to measure similarity between points in a way that can capture highly flexible, non-linear relationships, without explicitly transforming the data into a higher-dimensional space. Its key property is locality: similarity decays smoothly with Euclidean distance, enabling flexible nonlinear boundaries while controlling complexity.

In summary, SVMs combine rigorous optimization with kernel methods to achieve powerful classification. The RBF kernel, in particular, provides an effective balance between expressiveness and generalization, which explains its widespread use in domains ranging from text classification [43] to image recognition [21].

2.3.2 Random Forests

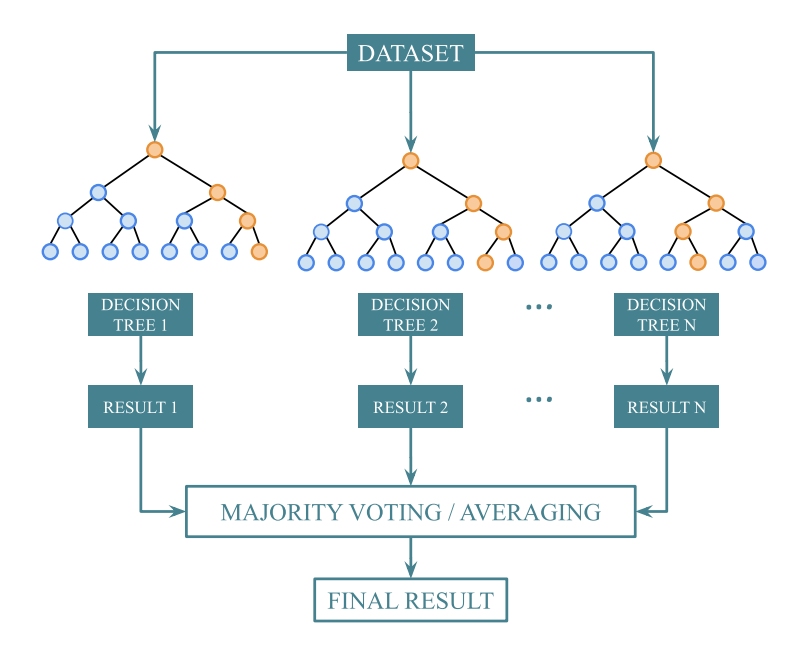


Figure 2.4 Illustration of a Random Forest showing an Ensemble of N Decision Trees and their Aggregated Predictions for two Classes.

Decision Trees are supervised learning models that partition the input space into regions associated with class labels (for classification) or numerical values (for regression). A tree is built by recursively splitting the training data based on feature values. At each internal node, a feature and split threshold are selected to maximize some measure of class purity, such as information gain. The process continues until stopping criteria are met, such as reaching a maximum depth or having too few samples to split further. The terminal nodes, or leaves, assign predictions.

A Decision Tree is a function

$$h(\mathbf{x}): \mathbb{R}^d \to \mathcal{Y},$$

where $\mathbf{x} \in \mathbb{R}^d$ is an input vector and \mathcal{Y} is the label space. The tree partitions the space into

disjoint regions $\{R_m\}$ such that

$$h(\mathbf{x}) = c_m \quad \text{if } \mathbf{x} \in R_m,$$

with c_m the majority class (classification) or average response (regression) within region R_m . While trees are interpretable and flexible, they are prone to high variance and overfitting.

Random Forests (RF), introduced by Breiman [18], deal with the instability of single trees by constructing an ensemble of them and aggregating their predictions. The central intuition is that although individual trees may be weak predictors, combining many diverse trees yields a strong classifier with reduced variance.

Formally, a Random Forest consists of tree classifiers of the form

$$h(\mathbf{x}, \Theta_k), \quad k = 1, \dots, K,$$

where Θ_k are independent identically distributed random vectors controlling the randomness in the k-th tree, such as bootstrap sampling of data or random selection of features at each split. For classification, the forest prediction is obtained by majority voting:

$$H_K(x) = \text{mode}\{h(\mathbf{x}, \Theta_k) : k = 1, \dots, K\}.$$

For regression, the forest prediction is the average of the tree outputs.

The theoretical performance of Random Forests can be analyzed using the *margin function*. For an input–output pair (\mathbf{X}, Y) and a finite forest of K trees, the margin is

$$mg(\mathbf{X}, Y) = \frac{1}{K} \sum_{k=1}^{K} I(h(\mathbf{X}, \Theta_k) = Y) - \max_{j \neq Y} \frac{1}{K} \sum_{k=1}^{K} I(h(\mathbf{X}, \Theta_k) = j),$$

where $I(\cdot)$ is the indicator function. The margin measures how much more the forest favors the correct class Y over its most competitive alternative.

The *generalization error* of the Random Forest is then defined as the probability that the margin is negative:

$$PE^* = \mathbb{P}_{\mathbf{X},Y}(mg(\mathbf{X},Y) < 0).$$

As the number of trees $K \to \infty$, the law of large numbers implies that

$$mg(\mathbf{X}, Y) \longrightarrow mr(\mathbf{X}, Y) = P_{\Theta}(h(\mathbf{X}, \Theta) = Y) - \max_{j \neq Y} P_{\Theta}(h(\mathbf{X}, \Theta) = j),$$

where $mr(\mathbf{X}, Y)$ denotes the expected margin, thus the margin converges to its expectation under the randomization. A central property of Random Forests is that the generalization

error converges almost surely to a limit, meaning that adding more trees does not cause overfitting.

Breiman [18] showed that performance depends on two key factors: the *strength* of individual trees and the *correlation* among them. The strength is defined as the expected margin,

$$s = \mathbb{E}_{\mathbf{X},Y}[mr(\mathbf{X},Y)],$$

and the average correlation of tree errors is denoted by ρ . An upper bound then holds:

$$PE^* \le \frac{\rho \left(1 - s^2\right)}{s^2}.$$

This inequality reveals that the best forests combine accurate individual trees (large s) with low correlation between them (small ρ). Random feature selection at each split is specifically designed to lower correlation while maintaining strength.

From a computational perspective, growing a single unpruned Decision Tree on N samples with M features requires $\mathcal{O}(MN\log N)$ operations. In a Random Forest, only $F\ll M$ features are considered at each split, reducing the cost per tree to $\mathcal{O}(Fn\log n)$, where $n\leq N$ is the number of samples in the bootstrap subset. By combining bagging with random feature selection, Random Forests extend Decision Trees to reduce variance and improve predictive performance. Although training multiple trees increases total computation, Random Forests remain efficient in practice and are capable of handling high-dimensional data with robustness to overfitting.

Chapter 3

Related Work & Methodology

3.1 Datasets

The experiments in this study utilize several publicly available EEG datasets that have become benchmarks for emotion recognition, BCI, and epilepsy detection research. Each dataset differs in its recording setup, stimuli type, and labeling scheme, providing complementary perspectives on affective and cognitive state modeling, as well as clinical EEG analysis.

SEED: The SEED dataset [122] is a widely used benchmark for EEG-based emotion recognition. It comprises EEG recordings from 15 participants while they viewed 15 Chinese film clips, each lasting approximately 4 minutes. Each video was selected to induce one of three affective states—positive, neutral, or negative—resulting in a single categorical label per clip. The EEG signals were recorded using a 62-channel setup following the 10–20 configuration, with an original rate of 1000 Hz, subsequently downsampled to 200 Hz.

DEAP: The DEAP dataset [59] is another widely used benchmark for EEG-based emotion recognition. It comprises recordings from 32 participants while they watched 40 excerpts of music videos, each of 1-minute duration, designed to elicit various affective responses. After each video, participants rated their experience along the dimensions of arousal, valence, liking, dominance, and familiarity on continuous 9-point scales. EEG signals were collected using a 32-channel setup following the international 10–20 system [25] at 512 Hz and downsampled to 128 Hz, together with peripheral physiological measures such as GSR, respiration, and EMG. The dataset provides continuous-valued affective labels in the valence—arousal space, enabling both categorical and dimensional emotion modeling.

BCI Competition IV Dataset 2a: The BCI-IV 2a dataset [20] consists of EEG recordings from 9 subjects performing 4 motor imagery tasks, i.e., left-hand, right-hand, feet, and tongue movement imagery. Each subject completed two sessions on different days, with each session

comprising 6 runs of 48 trials (12 per class), resulting in 288 trials per session. Each trial lasted 6 seconds in total, with an onset cue presented after the first 2 seconds. Subjects performed the instructed motor imagery for the subsequent 4 seconds, which was used as the analysis window. EEG was acquired from 22 channels following the 10–20 configuration [25], along with 3 electrooculogram (EOG) channels, all sampled at 250 Hz.

TUH Epilepsy Corpus: The TUH Epilepsy Corpus (TUEP) [112] is a curated collection of clinical EEG data from Temple University Hospital, including recordings from 100 epileptic and 100 healthy subjects. In total, TUEP contains 698 sessions, yielding 1,785 EEG recordings from epileptic and 513 from non-epileptic patients. Individual recording durations vary from a few seconds to approximately one hour. All EEG signals were acquired using the 10–20 configuration with 19 channels and sampled at 250 Hz with supplementary electrocardiogram (EKG) channels also available.

Further details regarding the experimental setup, data collection procedures, and dataset formats are provided in the Appendices.

3.2 Literature Review

3.2.1 Traditional EEG Features

Traditional EEG analysis has relied on hand-crafted features designed to capture statistical, spectral, and dynamical signal properties. Statistical descriptors such as mean, variance, zero-crossing counts, and autocorrelation have long been used for baseline characterization [96], [113], [117], [118]. However, spectral approaches, particularly Power Spectral Density (PSD), remain the most common approach for quantifying canonical oscillatory rhythms [16], [102]. Recently proposed complementary measures to quantify temporal and spatial complexity include differential entropy [122] and asymmetry indices [103] respectively. Multiscale and non-stationary dynamics are effectively captured by Discrete Wavelet Transform (DWT) and Empirical Mode Decomposition (EMD) [29], [44], [67], while nonlinear descriptors, including fractal dimensions [12], [125] and higher-order spectra [80] have been used to capture the chaotic structure of EEG. Despite this rich toolbox, most approaches rarely target an explicit analysis of transient and nonlinear dynamics in EEG, which motivates the use of operators such as the Teager–Kaiser Energy Operator (TKEO).

3.2.2 TKEO Applications

The TKEO is widely used in signal processing domains for detecting instantaneous energy fluctuations in oscillatory signals, with various applications. In speech processing, it has been leveraged for tasks such as formant detection [46], denoising [58], replayed speech identification [92], and emotion recognition [57], [95]. In music signal analysis, TKEO has been used

for tempo estimation [49], note onset detection [38], instrument [124] and genre recognition [126]. Beyond acoustic signals, TKEO has proven effective in biomedical applications to extract physiologically plausible energy fluctuations. In cardiovascular research, for example, it has enabled automated phonocardiogram (PCG) analysis for the detection of heart valve disorders without requiring prior segmentation [119]. With respect to analysis of neurophysiological recordings, TKEO has been used for electromyography (EMG) segmentation to detect precise movement onsets [15], while modified thresholding strategies have further improved detection accuracy [60].

Beyond its applications in speech, music, and other physiological signals, the TKEO has also been explored for EEG analysis. Early studies focused on fundamental tasks such as differentiating sleep stages [66], discriminating focal from non-focal brain activity [22], and detecting epileptic events [13]. More recent work has extended the use of TKEO to affective computing; for example, it has been employed for stress detection by extracting energy-based features from the alpha and beta bands, where logistic coefficients derived from TKEO demonstrated strong discriminative power between stressed and non-stressed states [62]. In the context of BCI research, Kaleem et al. [55] combined empirical mode decomposition with multivariate phase space (EMD-MPS) and TKEO to classify cognitive tasks such as mental arithmetic, letter composition, and 3D rotation, achieving accuracies of up to 87%. However, not all applications yielded favorable results: Martisius et al. [75] reported that conventional TKEO performed poorly for motor imagery EEG. They showed, nonetheless, that higher-order generalizations—most notably the Homogeneous Multivariate Polynomial Operator (HMPO)—substantially improved classification accuracy, highlighting the importance of operator choice in TKEO-based feature extraction.

3.2.3 EEG-Based Emotion Recognition Methods

EEG has received considerable attention for emotion recognition, as it enables the observation of brain activity underlying emotional processes, providing a direct, noninvasive, and temporally precise measure of affective responses compared to peripheral physiological signals. [7]. Research typically focuses on mapping EEG oscillatory dynamics to emotional dimensions such as valence and arousal, where frontal alpha asymmetry has been linked to valence, and beta or gamma activity to arousal and attentional engagement [7], [103], [122].

As reviewed by Liu et al. [70], traditional EEG-based emotion recognition methods primarily depend on manually engineered features—such as band-limited power spectral density (PSD), differential entropy, and various functional connectivity indices—extracted from preprocessed EEG signals. These hand-crafted features are subsequently used as inputs to classical machine learning classifiers, including Support Vector Machines (SVM), K-means clustering, K-Nearest Neighbors (KNN), and Random Forests, to categorize different emotional states. These approaches have shown consistent performance across public datasets such as DEAP,

SEED, and DREAMER [56]. More recently, deep learning has enabled end-to-end modeling of affective EEG using convolutional [73], recurrent [24], and attention-based [42] architectures, as well as graph neural networks [69] that exploit spatial—temporal relationships between electrodes.

As highlighted by Apicella et al. [9], despite significant advances in EEG-based emotion recognition, achieving robust generalization across subjects and sessions remains a major challenge. This limitation stems largely from the inherent variability and non-stationarity of EEG signals, which lead to dataset shift and hinder consistent model performance. Furthermore, individual differences in psychological, physiological, and environmental factors introduce additional sources of uncertainty, while issues such as subjective affect labeling and the limited interpretability of deep learning models continue to complicate reliable emotion decoding. Current research [9], therefore, emphasizes the development of methods that enhance model robustness, explainability, and cross-subject adaptability—particularly through transfer learning and domain adaptation strategies—to enable more generalizable and practical emotion-aware systems.

3.2.4 EEG-Based Motor Imagery and BCI Systems

Following EEG-based emotion recognition methods, motor imagery (MI) represents another extensively studied paradigm in EEG and brain-computer interface (BCI) research. Owing to its ability to generate distinct and reproducible neural patterns associated with imagined movements, MI provides a valuable framework for both scientific investigation and the development of practical neurotechnology.

Beyond its theoretical significance, MI has demonstrated practical utility in a range of applied domains. One of its primary uses lies in motor rehabilitation, particularly for patients with stroke or severe paresis, where MI-based interventions have shown efficacy in enhancing motor recovery by promoting neuroplasticity and motor relearning [77], [78], [115]. MI is also extensively applied in brain-computer interface (BCI) systems, which translate imagined motor actions into control commands, enabling users to interact with external devices such as computers, robotic systems (e.g. exoskeleton), or wheelchairs without physical movement [8], [89], [121]. These BCI systems benefit from MI's capacity to generate distinguishable neural patterns [68], making them effective for assistive technologies aimed at improving autonomy in individuals with motor impairments [121]. As shown in Fig. 3.1, an MI-based BCI can process EEG signals in real time to control a lower-limb exoskeleton, thereby supporting motor function and rehabilitation. In addition to rehabilitation and assistive control, MI is increasingly employed to enhance performance in healthy individuals. When combined with physical training, it can enhance muscle strength by improving movement technique and fostering individual motivation [64]—often matching or even surpassing the benefits of physical practice alone [61].

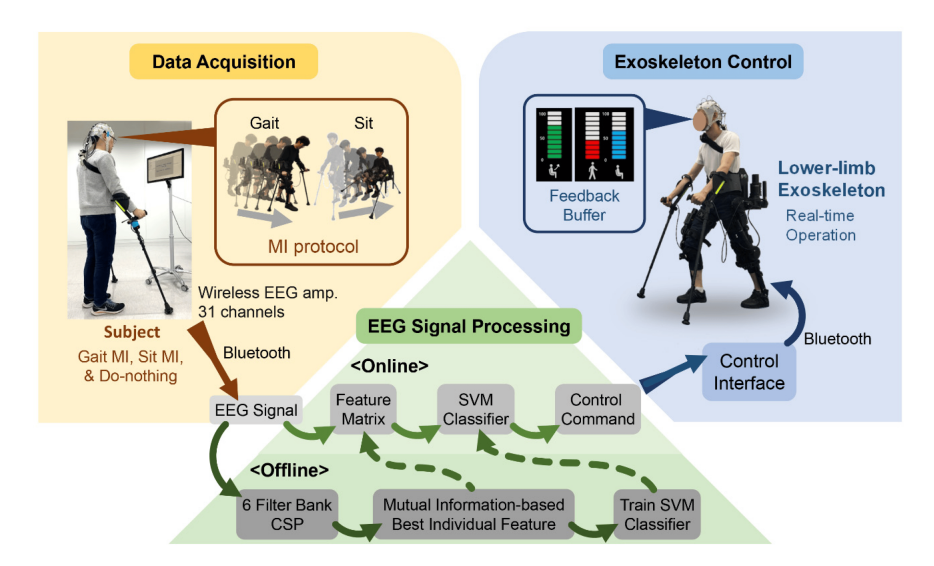


Figure 3.1 Diagram of a MI-based BCI System for Exoskeleton Control [23].

Despite the promising applications of MI-based systems, several significant challenges remain, including time-consuming, user-specific calibration and limited generalizability across individuals [88]. Additionally, translating lab-based technologies into real-world applications requires careful attention to usability, reliability, intuitiveness, and cost, while adapting designs to the specific needs and contexts of target users. Continued research and innovation are essential to overcoming current limitations and fully exploiting the potential of MI not only across clinical contexts, but also in everyday applications.

3.2.5 EEG-Based Epilepsy Detection Methods

Given the clinical importance of EEG analysis, one of its most critical applications lies in the automated detection of epileptic activity. Automated epilepsy detection has emerged as an essential research area within computational neuroscience, focusing on identifying interictal epileptiform discharges (IEDs), which are transient events observed in EEG recordings [2], and seizure episodes in EEG data to assist clinicians in diagnosis and treatment planning. Detection and mapping methods for epileptic activity rely on both scalp EEG (scEEG) and intracranial EEG (iEEG) recordings, which respectively provide non-invasive low-resolution and invasive high-resolution measurements of brain electrical activity [3]. scEEG is widely used in clinical and research settings but is limited by attenuation and noise, whereas iEEG offers highly localized information essential for accurate identification of interictal epileptiform discharges (IEDs) and seizure foci. Consequently, recent work [3] has focused on developing models that can map or translate scEEG to iEEG to enhance diagnostic precision in epilepsy assessment. Techniques range from mimetic approaches and feature extraction

based on linear and non-linear EEG descriptors [116], to more advanced approaches leveraging dynamic functional brain networks and tensor decomposition for feature extraction and epilepsy prediction [65]. In recent years, deep learning approaches—particularly convolutional neural networks (CNNs) and recurrent neural networks (RNNs) [41], [110], [114], generative adversarial networks (GANs) [4], and autoencoders (AEs) [1]—have been applied for detecting IEDs and for mapping scEEG to iEEG. These methods aim to enhance sensitivity and specificity in IED detection, supporting early diagnosis and treatment planning for epilepsy patients.

3.3 Preprocessing

EEG recordings from DEAP and SEED, as noted in the Appendices, are already provided in a preprocessed form. In contrast, datasets available in raw form required additional preprocessing steps. For the rest of the datasets (i.e., BCI-IV 2a and TUEP), we applied a similar pipeline that involved Independent Component Analysis (ICA) to remove EKG artifacts in TUEP and EOG artifacts in BCI-IV 2a. Then, a notch filter with a Finite Impulse Response (FIR) design was applied at 60 Hz for TUEP and 50 Hz for BCI-IV 2a to eliminate powerline interference. Finally, all signals were highpass-filtered at 0.5 Hz using a FIR filter.

All EEG recordings were partitioned into overlapping segments, with window lengths and overlap ratios chosen according to the specific characteristics of each dataset. This approach enables the extraction of temporally localized features while maintaining comparability across different recordings. For the DEAP dataset, the 60-second recordings were segmented into 20-second windows, each with 50% overlap, resulting in 5 windows per sample. Similarly, the SEED recordings, each lasting approximately 4 minutes, were partitioned into 20-second windows with 50% overlap, yielding 23 segments per recording. To ensure consistency with prior work [52], [111], the TUEP samples were segmented into 10-second windows with no overlap, due to computational memory constraints. The resulting number of windows per sample varied according to the recording duration (ranging from approximately 1 minute to 1 hour), resulting in between 11 and 719 windows per sample. For the BCI-IV 2a dataset, each recording consists of a continuous session for a participant, encompassing both cue presentation periods and inter-trial breaks. Since the precise event markers corresponding to cue onset are provided, we extracted fixed-length segments of 4-sec., following each cue presentation. This procedure yielded 288 motor imagery windows per recording.

Before TKEO-based feature extraction, each EEG segment was decomposed into five narrow-band components using bandpass filtering corresponding to the canonical EEG bands. Multiple filterbank configurations (12, 25, and 50 filters) were then applied within the frequency range of each canonical band on the DEAP, SEED, and BCI-IV 2a, in order to systematically evaluate the effect of filterbank resolution on the extracted features. In contrast, only 12 filterbanks were applied to the TUEP dataset due to computational constraints. For base-

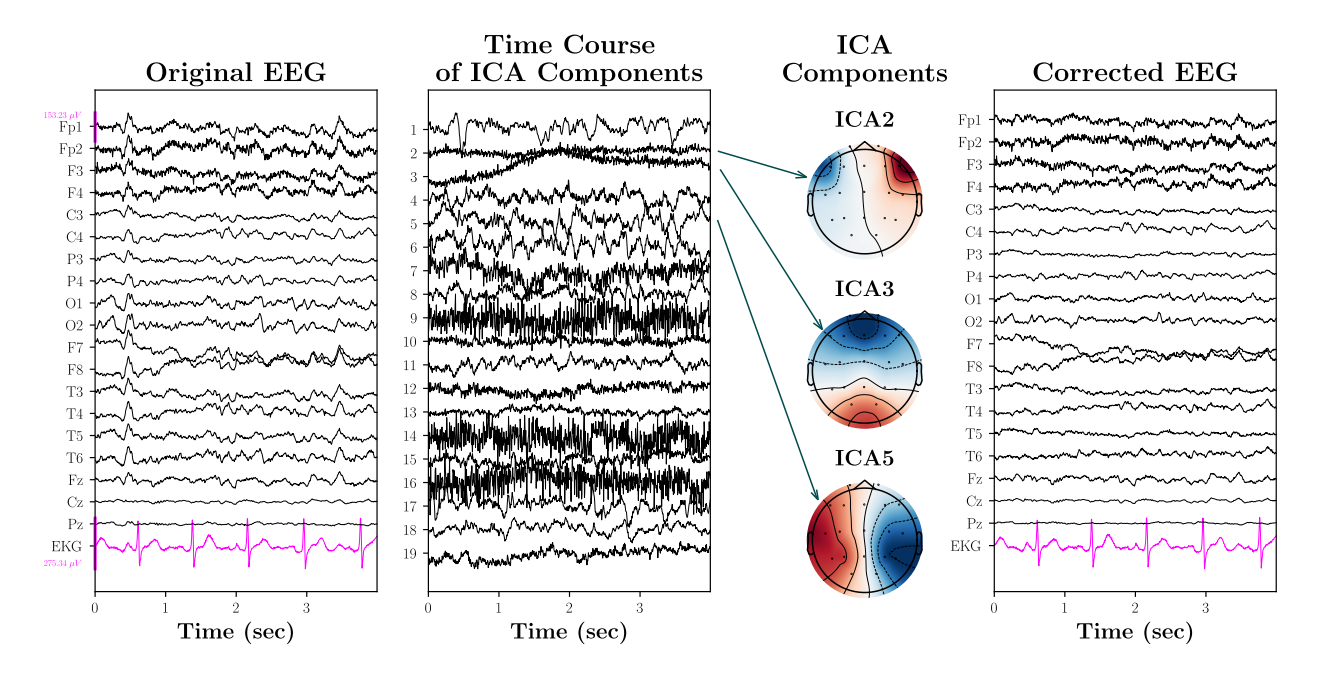


Figure 3.2 Independent Component Analysis (ICA) Applied to EEG Data From the TUEP Dataset. The Figure Shows the Original EEG Channel Signals (Left), the Time Courses of the Extracted ICA Components (Middle), the Corresponding Spatial Topographies of Selected Components (Right Middle), and the Corrected EEG After Artifact Removal (Right).

line comparisons, frequency bands were extracted using a standard 10th-order Butterworth bandpass filter, providing a conventional single-band reference for evaluating the benefit of the filterbank approach. All windowing and filterbank configurations for the datasets used in this study are summarized in Table 3.1.

Dataset	Window (s)	Overlap (%)	# Filters
SEED	20	50	12, 25, 50
DEAP	20	50	12, 25, 50
BCI-IV 2a	4	0	12, 25, 50
TUEP	10	0	12

 Table 3.1 Dataset-wise Preprocessing Parameters.

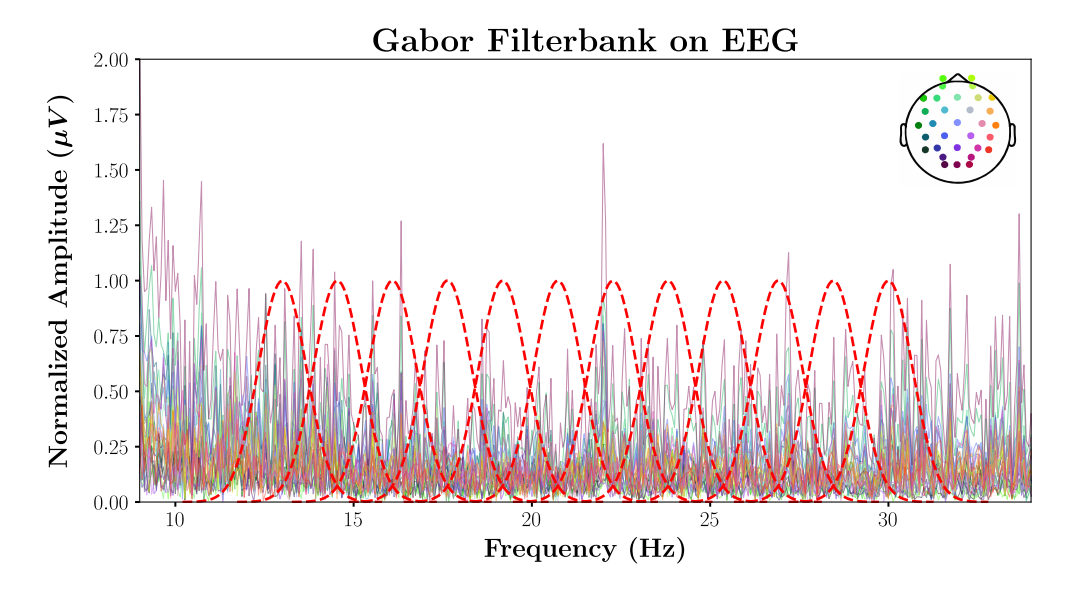


Figure 3.3 Gabor Filterbank with 12 Filters applied to EEG Channels from the DEAP Dataset in the Beta Band. The Red Dashed Curves represent the 12 Gabor Band-pass Filters, while the Colored Traces show the Spectral Amplitudes of Individual EEG Channels. The Channel Topology is displayed in the upper-right inset.

3.4 Feature Extraction

3.4.1 Baseline Features

To enable a comparative evaluation of the proposed approach and to assess its potential complementarity with standard EEG descriptors, we extract a set of baseline features. These features include the *Power Spectral Density (PSD)* and the *Instantaneous Power (IP)* of the signal.

- Power Spectral Density (PSD): Chapter 2 highlighted that the PSD corresponds to the Fourier transform of a signal's autocorrelation. This representation has become a common choice for extracting features from EEG data because it provides access to valuable patterns distributed across established EEG frequency ranges. In this work, the PSD is estimated using Welch's method, producing $\frac{f_s}{2}$ features per extracted window, where f_s denotes the sampling frequency. Consequently, the dimensionality of the PSD features is 64 for the DEAP, 100 for SEED, 125 for TUEP, and 125 for the BCI-IV 2a dataset.
- Squared Energy (SE): The SE, defined as the squared magnitude of the signal at each time instant, corresponds to the instantaneous power $p[n] = |x[n]|^2$ introduced in

Chapter 2. It is commonly used in signal processing as a direct measure of a signal's instantaneous energy. Similar to the proposed TKEO statistical descriptors described below, the *mean Squared Energy* of each band, as well as its contribution to the total signal energy (*mean Relative Squared Energy*) features are extracted.

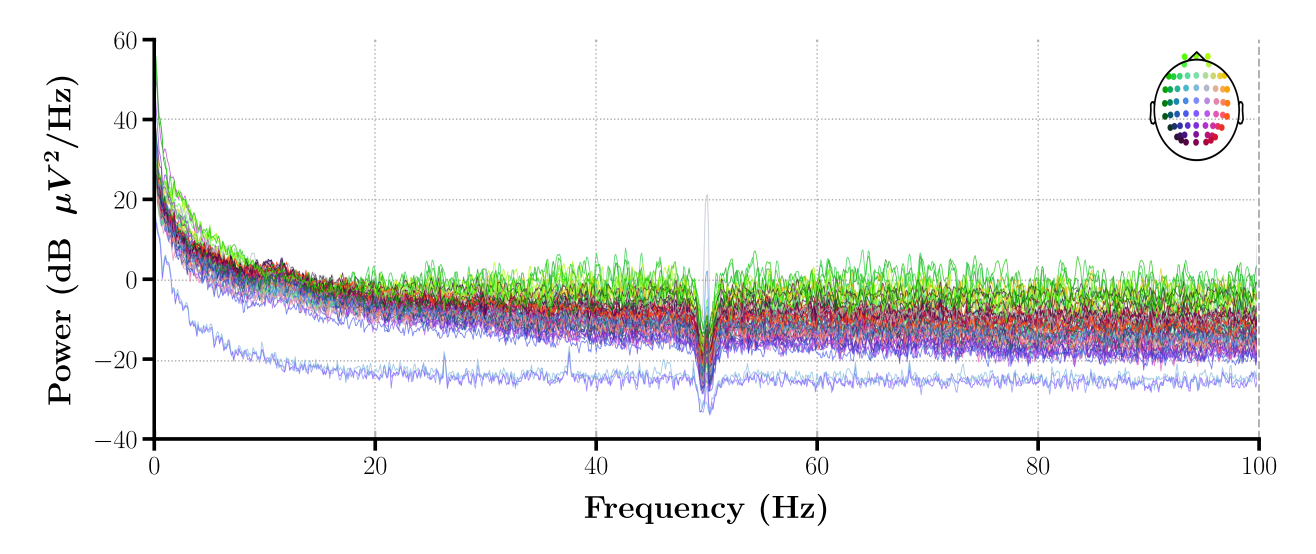


Figure 3.4 Power Spectral Density of EEG Channels from the SEED Dataset. The Signals were Notch-filtered at 50 Hz using Finite Impulse Response Band-pass filter.

3.4.2 TKEO Features

We extract TKEO-based features from EEG signals to get valuable information to use as input in the classification tasks. Each feature is calculated independently for each EEG channel and for each frequency band, resulting in a feature vector of dimensionality (bands × channels × features) for each sample. For clarity, the TKEO-based features can be conceptually divided into three categories: statistic-based, relevant-energy-based, and ESA-based descriptors. The specific measures included in each group are outlined as follows. We constrain our analysis to the discrete-time formulation of the TKEO, i.e., $\Psi \equiv \Psi_d$, for the purpose of this study.

Statistics

Let s denote the signal corresponding to a specific channel-band pair, consisting of N samples, and s_i its i-th sample. We calculate the following:

• Mean Teager–Kaiser energy:

$$\mu_{\Psi}(s) = \frac{1}{N} \sum_{i=1}^{N} \Psi(s_i)$$

• Variance of Teager–Kaiser energy:

$$v-\Psi(s) = \frac{1}{N} \sum_{i=1}^{N} (\Psi(s_i) - \mu_{\Psi}(s))^2,$$

• Absolute difference between the maximum and minimum Teager–Kaiser energies:

$$\operatorname{Max-Min}_{\Psi}(s) = \max_{i \in [1,N]} \{ \Psi(s_i) \} - \min_{i \in [1,N]} \{ \Psi(s) \}$$

• Skewness of TKEO:

$$s-\Psi(s) = \frac{\frac{1}{N} \sum_{i=1}^{N} (\Psi(s_i) - \mu_{\Psi}(s))^3}{\left(\frac{1}{N} \sum_{i=1}^{N} (\Psi(s_i) - \mu_{\Psi}(s))^2\right)^{3/2}}$$

• Kurtosis of TKEO:

$$k-\Psi(s) = \frac{\frac{1}{N} \sum_{i=1}^{N} (\Psi(s_i) - \mu_{\Psi}(s))^4}{\left(\frac{1}{N} \sum_{i=1}^{N} (\Psi(s_i) - \mu_{\Psi}(s))^2\right)^2} - 3$$

• Index of maximum Teager-Kaiser energy:

$$i_{\Psi_{\max}}(s) = \operatorname*{arg\,max}_{i \in [1,N]} \{\Psi(s_i)\}$$

• Absolute difference of the indexes of maximum and minimum Teager-Kaiser energy:

$$i_{\Psi_{\max-\min}}(s) = |\arg\max_{i \in [1,N]} \{\Psi(s_i)\} - \arg\min_{i \in [1,N]} \{\Psi(s_i)\}|$$

Relative Energy

For a band-specific signal s, the *relative* contribution of its Teager–Kaiser energy with respect to all frequency bands under consideration is defined as

$$RE_{band}(s) = \frac{\Psi_{band}(s)}{\sum_{k} \Psi_{k}(s)}$$

where band $k \in \{\text{Delta}, \text{Theta}, \text{Alpha}, \text{Beta}, \text{Gamma}\}$. Consequently, we calculate the following statistics of RE to use as features:

• Mean relative energy:

$$\text{m-RE}_{\text{band}}(s) = \frac{1}{N} \sum_{i=1}^{N} \text{RE}_{\text{band}}(s_i)$$

• Variance of relative energy:

$$v-RE_{band}(s) = \frac{1}{N} \sum_{i=1}^{N} (RE_{band}(s_i) - m-RE_{band}(s))^2,$$

• Absolute difference between the maximum and minimum relative energies:

$$\operatorname{Max-Min}_{\operatorname{RE}}(s) = \max_{i \in [1,N]} \{ \operatorname{RE}_{\operatorname{band}}(s_i) \} - \min_{i \in [1,N]} \{ \operatorname{RE}_{\operatorname{band}}(s_i) \}$$

• Index of maximum relative energy:

$$i_{\text{RE}_{\text{max}}}(s) = \underset{i \in [1,N]}{\operatorname{arg max}} \{ \text{RE}_{\text{band}}(s_i) \}$$

• Absolute difference of the indexes of maximum and minimum relative energy:

$$i_{\text{RE}_{\text{max-min}}}(s) = |\underset{i \in [1,N]}{\operatorname{arg max}} \{ \text{RE}_{\text{band}}(s_i) \} - \underset{i \in [1,N]}{\operatorname{arg min}} \{ \text{RE}_{\text{band}}(s_i) \} |$$

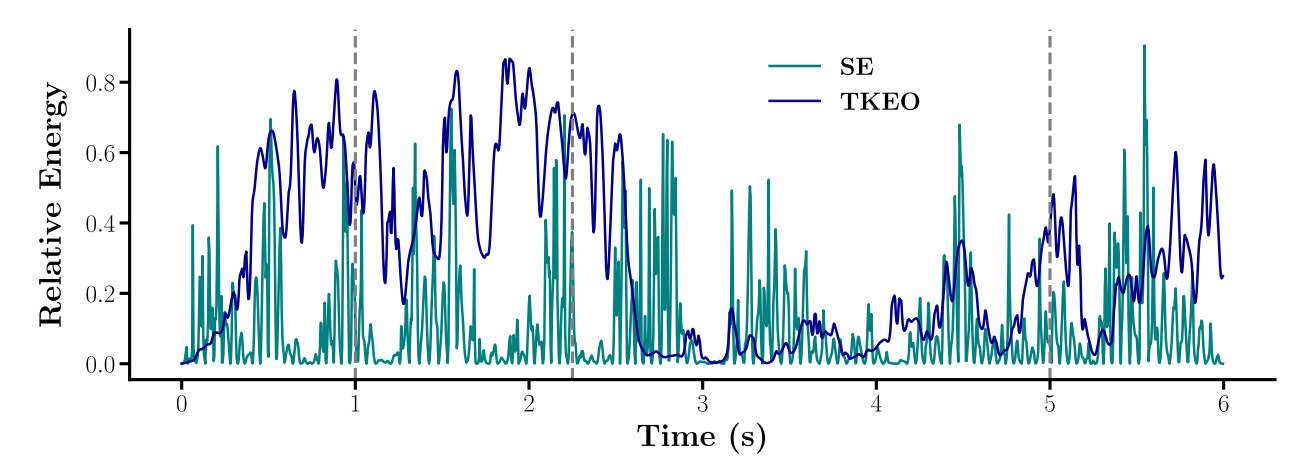


Figure 3.5 Relative Squared and Teager–Kaiser Energies of the FC4 Channel From the BCI-IV 2a Dataset in the Alpha Band. Gray dotted vertical lines represent the Start of the Cue (1s), the End of the Cue (2.25s), and the End of Motor Imagery (5s). TKEO Relative Energy shows fewer variations within each period, remaining low during MI and higher during the Resting Periods, whereas SE exhibits more fluctuations. This indicates that TKEO Relative Energy provides a smoother and more discriminative Representation for MI.

Energy Separation Algorithm

In this work, we adopt the *DESA-1* algorithm to extract the Instant Amplitude Modulation (a(s)) and Instant Frequency Modulation $(\Omega(s))$. Subsequently, we calculate the DESA-based features:

• Mean of Instant Amplitude Modulation (m-IAM) [124]:

$$\text{m-IAM}(s) = \frac{1}{N} \sum_{i=1}^{N} |a(s_i)|$$

• Weighted mean of Instant Frequency Modulation (m-IFM) [124]:

$$\text{m-IFM}(s) = \frac{\sum_{i=1}^{N} \Omega(s_i) \cdot \left(\text{m-IAM}(s_i)\right)^2}{\sum_{i=1}^{N} \left(\text{m-IAM}(s_i)\right)^2}$$

• Variance of the Instant Frequency Modulation (v-IFM):

v-IFM(s) =
$$\frac{1}{N} \sum_{i=1}^{N} (\Omega(s_i) - \mu_{\Omega}(s))^2$$
,

where
$$\mu_{\Omega}(s) = \frac{1}{N} \sum_{i=1}^{N} \Omega(s_i)$$
.

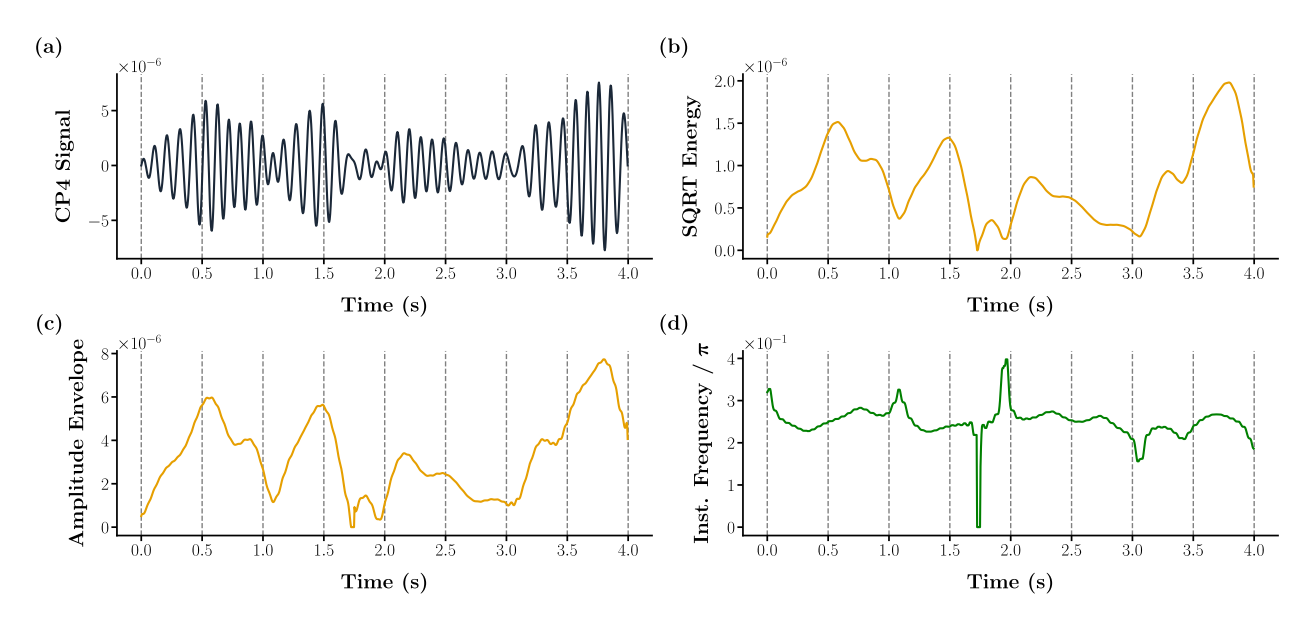


Figure 3.6 (a) CP4 Channel Signal from the BCI-IV 2a Dataset in the Alpha Band. (b) Square Root of TKEO. (c) Estimated Amplitude Envelope using DESA-1. (d) Estimated Instantaneous Frequency using DESA-1, expressed as a fraction of π .

3.4.3 Selection of TKEO Features

In our experimental setup, we initially evaluated the performance of the model using the complete set of 15 extracted features. To further investigate the relative contribution of individual descriptors, we also examined different subsets of features and assessed their effectiveness through systematic testing. Based on these evaluations, we observed that a specific subset consisting of the mean Teager-Kaiser energy (m-TKEO), the mean Relative Energy (m-RE), the mean Instantaneous Amplitude Modulation (m-IAM), and the variance of Instantaneous Frequency Modulation (v-IFM) consistently yielded superior classification performance compared to other feature subsets.

For clarity in subsequent discussions, we define the terminology as follows: the complete set of 15 features is referred to as the "TKEO" features, whereas the reduced subset of the four best descriptors (m-TKEO, m-RE, m-IAM, and v-IFM) is designated as the "Selected TKEO" features. This distinction allows us to explicitly compare the impact of feature dimensionality reduction on classification outcomes in the following chapter. Additionally, we define the term "Combined" features as the set consisting of the Selected TKEO features using a 25-filters filterbank, the PSD, the mean Signal Energy, and the mean Relative Signal

Energy, concatenated. Finally, we denote as "TKEO-N FB", the TKEO features, which are extracted using N filters filterbank configuration.

3.5 Evaluation Protocol

We evaluate the TKEO-based features on the three tasks: Emotion Recognition, Motor Imagery, and Epilepsy Detection. Two evaluation settings are considered: Subject-Dependent and Subject-Independent. In the Subject-Dependent setting, classifiers are trained and tested on data from the same participant and performance is reported as the average across subjects. For the Emotion Recognition datasets, distinct trials are used for training and testing to prevent data leakage, since each participant is exposed to all stimuli. In the Subject-Independent setting, classifiers are trained on data from a group of participants and evaluated on unseen individuals. Then the average across experiment repetitions is reported. For Epilepsy Detection, only Subject-Independent evaluation is performed, since epilepsy is a subject-level condition and Subject-Dependent evaluation is not meaningful.

We note that performance in the Subject-Independent setting is typically lower, due to the strong subject-specific variability inherent in EEG signals [6], and a similar trend is therefore expected in our results.

3.5.1 Classification Models

For all experiments, we adopt a unified classification method that leverages features from all available EEG channels. The pipeline consists of a Standard Scaler, which standardizes the features by subtracting the training-set mean and dividing by the corresponding standard deviation, followed by a classifier. Specifically, we employ an SVM with an RBF kernel for the Subject-Dependent setting, while for the Subject-Independent, we use a Random Forest classifier with 100 estimators, chosen for its computational efficiency and scalability. Experiments address single-label classification tasks, namely: positive, neutral, or negative emotion in SEED; high-low valence and high-low arousal in DEAP, with classes determined by a median split; left hand, right hand, feet, or tongue motor imagery in BCI-IV 2a; and epilepsy versus non-epilepsy in TUEP. Data are divided into 80% training and 20% testing, with evaluation based on a stratified 5-fold cross-validation to preserve label proportions in each split. The datasets are balanced across classes, with the exception of TUEP, which is imbalanced, containing 77.7% of recordings from epileptic patients.

3.5.2 Evaluation Metrics

To assess how efficiently our machine learning models perform, a set of quantitative performance metrics is applied. Among the most widely adopted measures are those derived from

the confusion matrix, which provides a structured summary of classification outcomes by distinguishing between correct and incorrect predictions for each class (Fig. 3.7).

		Predict	ted Class	
		Positive	Negative	
Actual Class	Positive	True Positive TP	False Negative FN	Sensitivity $\frac{TP}{TP + FN}$
Actual	Negative	False Positive FP	True Negative TN	Specificity $\frac{TN}{TN + FP}$
		Precision $\frac{TP}{TP + FP}$	Negative Predictive Value TN TN + FN	$\frac{Accuracy}{TP + TN}$ $\frac{TP + TN}{TP + TN + FP + FN}$

Figure 3.7 Binary Classification Confusion Matrix, presenting key Evaluation Metrics.

True Positives (TP) represent correctly identified positive instances, while True Negatives (TN) correspond to correctly identified negative instances. Conversely, False Positives (FP) occur when negative samples are mislabeled as positive, and False Negatives (FN) arise when positive samples are classified as negative. Collectively, TP and TN constitute the set of correct predictions, whereas FP and FN represent the misclassifications.

In our work, we utilize as metrics the **Balanced Accuracy** and **ROC-AUC**, which are described subsequently. We further note that, in the cases of SEED and DEAP, for evaluation purposes we calculate the average of the per-excerpt metrics for each trial.

Balanced Accuracy: This metric can be applied to both binary and multi-class classification tasks. It is defined as the average of Sensitivity (Recall) and Specificity [19]:

$$Balanced\ Accuracy = \frac{Sensitivity + Specificity}{2},$$

where $Sensitivity = \frac{TP}{TP + TN}$ and $Specificity = \frac{TN}{TN + TP}$, as shown in Fig. 3.7.

ROC-AUC: The Receiver Operating Characteristic (ROC) curve [45] is a standard tool for evaluating the performance of binary classifiers, and it can be extended to multi-class problems. It is generated by plotting the True Positive Rate (Sensitivity) against the False Positive Rate (1 - Specificity) across different decision thresholds (Fig. 3.8). The Area Under the ROC Curve (AUC) provides a single scalar value that summarizes the classifier's ability to distinguish between classes. A model with perfect discrimination would correspond to

a curve reaching the top-left corner of the plot, which reflects both maximum sensitivity (no false negatives) and maximum specificity (no false positives). By contrast, a random classifier produces points that tend to align with the diagonal from (0,0) to (1,1), known as the line of no discrimination. Values above this line indicate performance better than random guessing, while points below suggest worse-than-random behavior—which, in principle, could be inverted into a useful predictor.

Importantly, the AUC metric is *threshold-independent*, as it integrates classifier performance across all possible thresholds. Hence, it provides a value in the range [0, 1], where higher values indicate better discriminative ability.

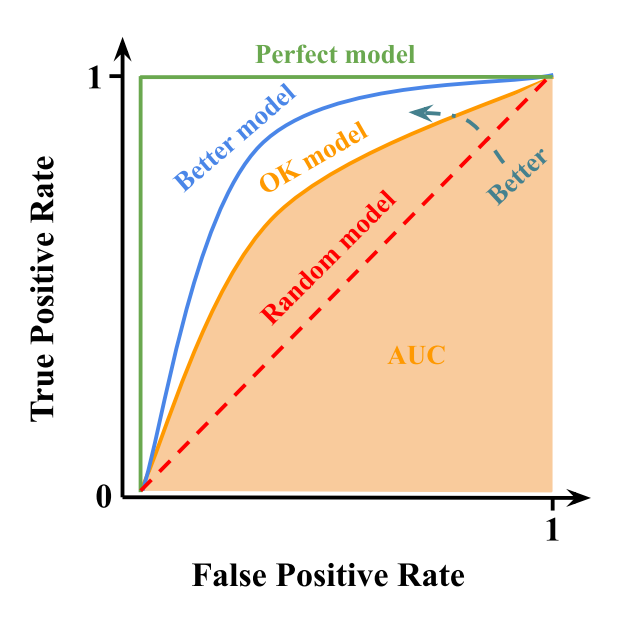


Figure 3.8 ROC Curves for Binary Classifiers, illustrating Model Performance against Random, with the AUC reported for one Model.

Chapter 4

Results & Discussion

The classification results for all features at the 2 settings are summarized in Tables 4.1-4.13. We report results using features extracted directly from the raw signal (raw-band), Alpha, Beta and Gamma bands, which are commonly reported to perform well in these tasks [51], [91], [100], as well as from the fusion of features computed across all canonical frequency bands (fused-band). TKEO features generally outperform the baseline features (PSD and Signal Energy) in Motor Imagery and Epilepsy Detection tasks, whereas in Emotion Recognition, the baselines achieve higher performance. The higher accuracies in Subject-Dependent tasks reflect the general understanding that brain signals are strongly influenced by individual-specific patterns. This is further reflected in the higher standard deviation values, where in the Subject-Dependent setting we observe approximately 10\% or higher variability across subjects. This larger deviation likely arises due to intra-subject model variability, as each model is trained and evaluated on a single individual, capturing unique neural signatures and noise characteristics that differ substantially between subjects. In contrast, the Subject-Independent setting exhibits considerably lower variability—around 1–5% in Emotion Recognition and 3-7% in Motor Imagery tasks—since performance is averaged across multiple train-test folds involving different subject combinations, resulting in more stable, but typically lower accuracies.

4.1 SEED Results

In the SEED dataset, the Subject-Dependent setting (Table 4.1) shows that SE achieves the highest overall Balanced Accuracy of 93.8%. Closely following these results, the TKEO-12 FB features achieve accuracies only 3.6% lower in the fused-band. Notably, across nearly all configurations, TKEO-based features outperform the PSD baseline in Balanced Accuracy and both baselines in ROC-AUC, indicating that the proposed approach provides superior

class separability compared to the baselines. Furthermore, fused-band features outperform single-band features, indicating that integrating information across frequency bands enhances emotion recognition performance. When comparing individual bands, the Beta and Gamma bands yield higher accuracies than the Alpha band, which aligns with the findings reported by Zheng et al. [122].

Features		Balanc	ed Accura	cy (%)		ROC-AUC ($\times 10^2$)					
	Alpha	Beta	Gamma	Raw	Fused	Alpha	Beta	Gamma	Raw	Fused	
SE PSD	$ \begin{array}{c} \hline 84.4_{\pm 10.2} \\ 74.2_{\pm 17.5} \end{array} $	$ \begin{array}{c} 83.1_{\pm 11.1} \\ 79.6_{\pm 18.3} \end{array} $	$ 82.2_{\pm 13.7} 69.8_{\pm 18.8} $	$ 80.4_{\pm 15.1} 85.8_{\pm 11.1} $			$ \begin{array}{r} \hline 94.2_{\pm 7.7} \\ 91.3_{\pm 10.3} \end{array} $	$ \begin{array}{r} \hline 93.5_{\pm 7.7} \\ 87.8_{\pm 10.3} \end{array} $	$89.3_{\pm 7.6}$ $96.4_{\pm 4.1}$	$ \begin{array}{r} \hline 97.6_{\pm 3.7} \\ 94.4_{\pm 6.8} \end{array} $	
TKEO-12 FB	$86.2_{\pm 10.4}$	$89.3_{\pm 9.7}$	$88.0_{\pm 13.4}$	$85.8_{\pm 9.1}$	$90.2_{\pm 8.7}$	$94.7_{\pm 6.3}$	$97.1_{\pm 3.8}$	$93.8_{\pm 8.1}$	$95.3_{\pm 4.8}$	$97.6_{\pm 4.3}$	
TKEO- 25 FB	$86.7_{\pm 12.9}$	$88.9_{\pm 10.5}$	$86.7_{\pm 10.3}$	$87.1_{\pm 9.9}$	$88.4_{\pm 11.0}$		$96.2_{\pm 5.0}$	$95.6_{\pm 5.4}$	$95.6_{\pm 4.5}$	$97.1_{\pm4.7}$	
TKEO- 50 FB	$85.3_{\pm 12.0}$	$87.1_{\pm 10.2}$				$95.6_{\pm 6.1}$	$96.0_{\pm 5.6}$	$94.7_{\pm 7.8}$	$97.3_{\pm4.1}$	$98.2_{\pm2.7}$	
Selected-12 FB	$84.9_{\pm 11.8}$	$83.6_{\pm 17.2}$	$85.8_{\pm 11.9}$	$86.7_{\pm 10.6}$	$87.1_{\pm10.4}$		$95.8_{\pm 7.6}$	$95.8_{\pm7.8}$	$96.2_{\pm 4.7}$	$97.6_{\pm 5.1}$	
Selected-25 FB	$82.2_{\pm 12.1}$	$85.3_{\pm 14.8}$	$86.7_{\pm 11.9}$	$88.0_{\pm 9.8}$	$87.6_{\pm 10.3}$		$96.2_{\pm 4.7}$	$94.2_{\pm 9.1}$	$97.3_{\pm 4.3}$	$97.8_{\pm 5.8}$	
Selected-50 FB		$86.7_{\pm 13.5}$	$84.9_{\pm 11.8}^{-}$	$86.7_{\pm 12.2}$		$95.6_{\pm 6.4}$	$94.5_{\pm 6.8}$	$95.6_{\pm 6.7}$	$97.3_{\pm 4.6}$	$96.4_{\pm 4.6}$	
Combined	$79.1_{\pm 14.8}$		$79.1_{\pm 14.8}$			$91.3_{\pm 10.5}$		$90.2_{\pm 11.1}$	$95.5_{\pm 7.2}$	$95.8_{\pm 5.8}$	

Table 4.1 Subject-Dependent 5-fold Mean Classification Performance and Standard Deviation on SEED.

Our highest accuracy results surpass those reported in [122] under the same setting, as shown in Table 4.2. Specifically, we achieve 90.2% and 88.9% accuracy for the TKEO-12 FB and TKEO-50 FB features at the fused-band, respectively, outperforming the best cases of differential entropy—based hand-crafted features.

Features	Accuracy (%)
Rational Asymmetry [122]	74.74
Differential Asymmetry [122]	75.03
Differential Caudality [122]	77.38
Differential Entropy [122]	86.08
TKEO-50 FB (ours)	88.9
TKEO-12 FB (ours)	90.2

Table 4.2 Comparison of the Highest Reported Accuracies of Differential Entropy—based Features in [122] with the Proposed TKEO-based Features on the SEED Dataset for the Subject-Dependent Task.

In the Subject-Independent setting (Table 4.3), SE achieves also the highest overall Balanced

Accuracy (68.1%) with Selected-25 FB having a 0.5% lower score in fused-band and PSD is once again outperformed by TKEO-based features in all cases, except in the broad, full-spectrum raw-band. Interestingly, in this setting, the Alpha band yields slightly higher accuracies than the Beta and Gamma bands. Furthermore, employing filterbanks with more than 12 filters generally improves accuracy, as the increased spectral resolution enables TKEO to resolve narrowband oscillatory components that would otherwise be smoothed by broader spectral divisions.

Features		Balanc	ed Accura	acy (%)		ROC-AUC ($\times 10^2$)					
	Alpha	Beta	Gamma	Raw	Fused	Alpha	Beta	Gamma	Raw	Fused	
SE PSD	$ \begin{array}{r} \hline 58.1_{\pm 5.8} \\ 46.7_{\pm 4.2} \end{array} $	$\frac{61.4_{\pm 1.7}}{55.5_{\pm 4.7}}$	$ 60.6_{\pm 3.4} $ $55.6_{\pm 4.2}$	$ \begin{array}{r} \hline 55.3_{\pm 4.5} \\ 63.2_{\pm 2.1} \end{array} $	$\overline{68.1_{\pm 3.9}}$ 62.0 $_{\pm 4.2}$	$ 75.7_{\pm 4.7} 64.9_{\pm 5.2} $	$79.4_{\pm 2.4}$ $75.7_{\pm 3.8}$	$79.6_{\pm 3.1} 76.0_{\pm 2.6}$	$73.4_{\pm 4.7}$ $81.4_{\pm 1.8}$	$84.9_{\pm 2.9}$ $80.6_{\pm 3.5}$	
TKEO-12 FB	$62.3_{\pm 3.7}$	$61.1_{\pm 3.2}$	$61.8_{\pm 3.6}$	$60.9_{\pm 3.7}$	$66.7_{\pm 3.9}$	$80.5_{\pm 3.1}$	$79.7_{\pm 2.9}$	$80.1_{\pm 3.3}$	$79.4_{\pm 2.9}$	$83.5_{\pm 3.2}$	
TKEO- 25 FB	$62.8_{\pm 3.9}$	$61.7_{\pm 3.8}$	$61.9_{\pm 3.5}$	$60.7_{\pm2.7}$	$66.5_{\pm 4.0}$	$80.4_{\pm 3.1}$	$79.9_{\pm 3.2}$	$79.9_{\pm 3.1}$	$79.3_{\pm 2.3}$	$83.5_{\pm 3.1}$	
TKEO- 50 FB	$62.6_{\pm 3.8}$	$61.8_{\pm 3.1}$	$61.4_{\pm 3.3}$	$61.4_{\pm3.7}$	$67.0_{\pm 3.9}$	$80.5_{\pm 2.9}$	$\textbf{80.1}_{\pm 2.9}$	$79.9_{\pm 3.1}$	$79.6_{\pm 2.8}$	$83.7_{\pm 3.0}$	
Selected-12 FB	$63.4_{\pm3.8}$	$61.1_{\pm 3.6}$	$62.9_{\pm 2.6}$	$61.4_{\pm 2.7}$	$67.5_{\pm 3.8}$	$81.3_{\pm 3.1}$	$79.6_{\pm 3.1}$	$80.8_{\pm 2.9}$	$79.6_{\pm 2.6}$	$84.3_{\pm 2.6}$	
Selected-25 FB	$63.2_{\pm 3.5}$	$61.4_{\pm 3.5}$	$62.9_{\pm 4.1}$	$62.3_{\pm 3.4}$	$67.6_{\pm 3.5}$	$81.0_{\pm 2.8}$	$79.9_{\pm 3.1}$	$80.6_{\pm 3.4}$	$80.0_{\pm 2.6}$	$84.4_{\pm 2.8}$	
Selected-50 FB	$63.6_{\pm4.0}$	$62.0_{\pm3.9}$	$63.2_{\pm 3.2}$	$62.1_{\pm 2.9}$	$67.0_{\pm 3.9}$	$81.3_{\pm 2.9}$	$80.1_{\pm3.1}$	$80.8_{\pm 3.2}$	$80.1_{\pm 2.3}$	$84.0_{\pm 2.9}$	
Combined	$59.7_{\pm 4.5}$	$57.8_{\pm 4.4}$	$56.1_{\pm3.5}$	$64.2_{\pm 1.8}$		$77.9_{\pm 3.4}$	$77.8_{\pm 3.2}$	$77.1_{\pm2.3}$	$\textbf{82.1}_{\pm 1.8}$	$82.4_{\pm 3.1}$	

Table 4.3 Subject-Independent 5-fold Mean Classification Performance and Standard Deviation on SEED.

We also compare our results with state-of-the-art machine learning techniques on the SEED dataset, as summarized in Table 4.4. The results show that deep learning models outperform our approach, suggesting that effective emotion recognition requires deeper and more complex feature modeling to capture the underlying patterns in EEG signals.

Features/Models	Accuracy (%)
Selected-12 FB (ours)	67.5
Selected-25 FB (ours)	67.6
Attention-LSTM [105]	72.1
Graph-Embedded CNN [104]	82.4
Bipartite Graph Adversarial Network [85]	85.8

Table 4.4 Comparison of the Highest Reported Accuracies of the Proposed TKEO-based Features with State-Of-The-Art Machine Learning Architectures on the SEED Dataset for the Subject-Independent Task.

4.2 DEAP Results

In the Subject-Dependent setting (Tables 4.5, 4.6) of the DEAP dataset, the PSD features achieve the highest overall accuracy in valence classification, with a Balanced Accuracy of 64.7% and a ROC-AUC of 70.2. In contrast, TKEO-based features outperform, in most cases, baseline methods in arousal classification. Among these, the Selected-50 FB features yields the best performance within the TKEO-based approaches, achieving Balanced Accuracy scores of 64.6% (valence) and 59.2% (arousal), and ROC-AUC values of 69.4 and 64.0, respectively, in the fused-band setting. Fusing frequency bands further enhances predictive performance across all TKEO-based variants, confirming that the integration of complementary spectral information benefits EEG-based emotion recognition. In the valence dimension, the Gamma band outperforms the Alpha and Beta bands, suggesting that higher-frequency EEG activity carries richer affective information in this context. Overall, valence classification yields higher performance than arousal across all feature types, indicating that instantaneous energy patterns associated with valence are more discriminative and stable, whereas arousal-related activity tends to be more variable.

Features		Balanc	ed Accura	cy (%)		ROC-AUC ($\times 10^2$)						
	Alpha	Beta	Gamma	Raw	Fused	Alpha	Beta	Gamma	Raw	Fused		
SE PSD	$ 60.8_{\pm 11.8} 59.4_{\pm 10.9} $		$ 61.8_{\pm 8.8} 63.5_{\pm 9.1} $	$\overline{62.8_{\pm 11.6}}_{64.7_{\pm 9.1}}$	$\overline{63.0_{\pm 11.2}\atop 63.8_{\pm 10.6}}$	$\overline{66.1_{\pm 14.7}}$ $62.9_{\pm 13.6}$	$\overline{68.6_{\pm 14.2}}$ $67.6_{\pm 16.7}$	$ 66.7_{\pm 11.8} 67.2_{\pm 13.6} $	$\overline{66.9_{\pm 13.9}}_{70.2_{\pm 10.8}}$	$\overline{68.4_{\pm 12.9}\atop 68.4_{\pm 13.7}}$		
TKEO-12 FB	$60.6_{\pm 10.3}$	$62.0_{\pm 12.0}$	$63.6_{\pm 11.1}$	$62.3_{\pm 11.5}$	$64.3_{\pm 9.2}$	$65.0_{\pm 13.1}$	$65.4_{\pm 15.5}$	$69.2_{\pm 13.8}$	$66.1_{\pm 11.5}$	$\textbf{70.6}_{\pm 10.8}$		
TKEO- 25 FB	$60.2_{\pm 10.6}$	$61.2_{\pm 10.4}$	$64.0_{\pm 10.1}$	$61.2_{\pm 9.2}$	$63.1_{\pm 10.5}$	$63.3_{\pm 12.0}$	$67.6_{\pm 13.5}$	$68.5_{\pm 12.5}$	$65.5_{\pm 9.1}$	$68.5_{\pm 12.1}$		
TKEO- 50 FB	${f 61.4}_{\pm 9.7}$	$60.8_{\pm 12.0}$	$64.2_{\pm 10.4}$	$59.6_{\pm 11.3}$	$64.1_{\pm 9.8}$	$65.6_{\pm 13.0}$	$65.9_{\pm 15.2}$	$\textbf{69.8}{\scriptstyle\pm13.0}$	$64.1_{\pm 12.8}$	$68.4_{\pm 12.3}$		
Selected-12 FB	$61.4_{\pm 11.5}$		$62.9_{\pm 9.1}$	$62.9_{\pm 10.3}$	$64.0_{\pm 10.6}$	$65.5_{\pm 14.0}$	$66.5_{\pm 14.4}$	$67.4_{\pm 12.2}$	$65.9_{\pm 14.2}$	$69.1_{\pm 13.9}$		
Selected-25 FB	60.6 ± 9.7	$61.6_{\pm 10.9}$	$61.1_{\pm10.5}$	$62.3_{\pm 10.4}$	$63.9_{\pm 8.3}$	$62.4_{\pm 15.2}$	$65.5_{\pm 14.1}$	$67.3_{\pm 12.9}$	$69.2_{\pm 13.3}$	$67.8_{\pm 12.2}$		
Selected-50 FB	$60.6_{\pm 12.1}$	$60.3_{\pm 12.3}$	$62.3_{\pm 10.5}$		$\textbf{64.6}{\scriptstyle\pm10.4}$	$63.4_{\pm 15.6}$	$64.6_{\pm 13.9}$	$67.9_{\pm 13.0}$	$64.9_{\pm 14.8}$	$69.4_{\pm 13.5}$		
Combined	$57.5_{\pm 7.5}$	$60.5_{\pm 9.6}$	$60.8_{\pm 8.9}$	$62.7_{\pm 8.8}$	$60.8_{\pm7.7}$	$61.5_{\pm10.5}$	$65.5_{\pm 12.5}$	$64.9_{\pm 11.3}$	$66.9_{\pm 11.4}$	$65.1_{\pm 10.5}$		

Table 4.5 Subject-Dependent of Valence 5-fold Mean Classification Performance and Standard Deviation on DEAP.

The Subject-Independent setting (Tables 4.7, 4.8) demonstrates the expected decrease in overall accuracy compared to the Subject-Dependent scenario, reflecting the greater variability introduced by inter-subject differences. In this configuration, performance values converge toward the mid-50% range, highlighting the challenge of generalizing across participants in Emotion Recognition tasks. Among the evaluated features, TKEO-based representations perform comparably to conventional PSD and SE baselines, maintaining Balanced Accuracy between 50–53% and ROC-AUC values around 51–56. The best results are achieved by the Combined and the Selected-12 FB features, which slightly outperform other variants with Balanced Accuracy of 54.2% and 54.0% and ROC-AUC of 56.2 and 54.8, respectively. These

Features		Baland	ced Accura	acy (%)		ROC-AUC ($\times 10^2$)						
	Alpha	Beta	Gamma	Raw	Fused	Alpha	Beta	Gamma	Raw	Fused		
SE PSD	$\overline{57.0_{\pm 8.7}}$ $54.3_{\pm 8.7}$	$\overline{56.4_{\pm 9.8}\atop 56.2_{\pm 10.9}}$	$\begin{array}{c} 55.6_{\pm 9.6} \\ 54.7_{\pm 9.9} \end{array}$	$ 53.4_{\pm 11.6} $ $55.2_{\pm 10.0}$	$\overline{58.5_{\pm 8.2}}$ $57.0_{\pm 9.5}$	$ \begin{array}{c} \hline 62.4_{\pm 12.5} \\ 58.0_{\pm 12.9} \end{array} $	$ 59.8_{\pm 14.1} 56.9_{\pm 15.4} $	$ 59.3_{\pm 11.9} 55.5_{\pm 13.9} $	$ 54.6_{\pm 14.3} $ $57.5_{\pm 13.6}$	$\overline{62.6_{\pm 10.7}\atop 60.4_{\pm 13.1}}$		
TKEO-12 FB	$58.0_{\pm 8.9}$	$55.2_{\pm 12.2}$	$56.6_{\pm 11.3}$	$\textbf{58.1}_{\pm 10.0}$	$58.0_{\pm 8.8}$	$59.4_{\pm 12.6}$	$59.1_{\pm 15.2}$	$60.2_{\pm 14.6}$	$60.7_{\pm 14.2}$	$63.3_{\pm 11.3}$		
TKEO- $25~\mathrm{FB}$	$54.0_{\pm 9.9}$	$55.6_{\pm 12.1}$	$58.2_{\pm10.1}$	$55.4_{\pm 10.0}$	$57.1_{\pm 9.8}$	$57.4_{\pm 13.8}$	$56.6_{\pm 16.5}$	$61.0_{\pm 14.8}$	$60.6_{\pm 11.5}$	$61.7_{\pm 12.7}$		
TKEO-50 FB	$55.6_{\pm 7.9}$	$56.2_{\pm 11.8}$	$56.9_{\pm 9.6}$	$56.1_{\pm 10.2}$	$58.3_{\pm 7.9}$	$58.7_{\pm 12.1}$	$57.2_{\pm 15.9}$	$59.7_{\pm 13.1}$	$57.4_{\pm 14.7}$	$61.5_{\pm 11.2}$		
Selected-12 FB	$56.8_{\pm 9.8}$	$55.1_{\pm 10.0}$	$57.2_{\pm 11.5}$	$57.5_{\pm 8.6}$	$58.9_{\pm 8.6}$	$61.4_{\pm 14.4}$	$58.7_{\pm 15.4}$	${\bf 61.6}_{\pm 13.2}$	$\textbf{60.9}_{\pm 12.4}$	$62.8_{\pm 11.4}$		
Selected-25 FB	$57.2_{\pm 9.5}$			$57.1_{\pm 10.7}$	$57.6_{\pm 10.0}$	$60.1_{\pm 13.6}$	$58.6_{\pm 13.6}$	$59.7_{\pm 15.0}$	$60.5_{\pm 12.5}$	$60.7_{\pm 14.9}$		
Selected-50 FB	$58.2_{\pm 8.7}$		$55.8_{\pm 8.7}$	$56.3_{\pm 10.0}$	$59.2_{\pm7.8}$	$61.0_{\pm 13.3}$	$\textbf{60.9}_{\pm 13.9}$		$60.0_{\pm 13.9}$	$64.0_{\pm11.1}$		
Combined	$55.8_{\pm6.5}$		$53.5_{\pm 8.0}$	$55.0_{\pm7.9}$	$54.9_{\pm 6.9}$	$57.6_{\pm 7.6}$	$55.4_{\pm 12.8}$	$56.3_{\pm 11.0}$	$57.2_{\pm 11.4}$	$58.4_{\pm 9.7}$		

Table 4.6 Subject-Dependent of Arousal 5-fold Mean Classification Performance and Standard Deviation on DEAP.

findings suggest that while TKEO captures informative local energy dynamics, its discriminative capacity is constrained under Subject-Independent conditions. In contrast to the Subject-Dependent setting, frequency-band fusion provides only marginal gains here, indicating that cross-subject generalization relies more on invariant temporal—spatial patterns than on band-specific spectral energy differences.

Features		Balance	ed Accura	acy (%)		ROC-AUC ($\times 10^2$)						
	Alpha	Beta	Gamma	Raw	Fused	Alpha	Beta	Gamma	Raw	Fused		
SE PSD	$ 52.8_{\pm 2.4} 51.0_{\pm 0.6} $	$\overline{53.6_{\pm 2.6}}$ $53.0_{\pm 2.6}$	$ 51.1_{\pm 4.4} $ $52.5_{\pm 1.9}$	$\overline{54.0_{\pm 2.6}}$ $53.4_{\pm 2.8}$	$\overline{53.6_{\pm 3.3}}$ $54.7_{\pm 3.6}$	$\overline{53.7_{\pm 3.2}}$ $52.4_{\pm 4.2}$	$\overline{54.8_{\pm 4.2}}$ $54.1_{\pm 3.9}$	$\overline{51.3_{\pm 6.3}}$ $51.4_{\pm 0.8}$	$\overline{55.9_{\pm 3.9}}$ $54.5_{\pm 2.2}$	$\overline{54.8_{\pm 5.2}}$ $56.0_{\pm 5.0}$		
TKEO-12 FB TKEO-25 FB TKEO-50 FB Selected-12 FB Selected-25 FB Selected-50 FB Combined	$\begin{array}{c} 52.0_{\pm 1.7} \\ 52.3_{\pm 1.0} \\ 52.5_{\pm 2.4} \\ 52.2_{\pm 1.3} \\ 52.8_{\pm 1.9} \\ 53.1_{\pm 1.7} \\ \textbf{53.2}_{\pm 3.1} \end{array}$	$\begin{array}{c} 53.4_{\pm 3.2} \\ 52.4_{\pm 3.4} \\ 53.0_{\pm 3.4} \\ \textbf{54.0}_{\pm 2.5} \\ 52.3_{\pm 3.0} \\ 52.5_{\pm 2.3} \\ 53.6_{\pm 2.6} \end{array}$	$\begin{array}{c} 51.5_{\pm3.6} \\ 51.0_{\pm2.5} \\ 50.3_{\pm3.5} \\ 51.0_{\pm3.1} \\ 51.1_{\pm2.8} \\ 50.8_{\pm3.2} \\ \textbf{52.8}_{\pm4.1} \end{array}$	$\begin{array}{c} 50.7_{\pm 2.8} \\ 51.1_{\pm 1.1} \\ 51.0_{\pm 1.8} \\ 50.1_{\pm 2.2} \\ 50.6_{\pm 2.1} \\ 50.3_{\pm 1.7} \\ 54.2_{\pm 3.7} \end{array}$	$\begin{array}{c} 52.6_{\pm 2.8} \\ 52.5_{\pm 3.3} \\ 53.2_{\pm 3.0} \\ 52.6_{\pm 2.4} \\ 52.0_{\pm 3.1} \\ 52.8_{\pm 2.5} \\ 54.1_{\pm 2.7} \end{array}$	$\begin{array}{c} 52.9_{\pm 2.1} \\ 53.6_{\pm 1.6} \\ 53.3_{\pm 2.6} \\ 52.7_{\pm 1.4} \\ 54.1_{\pm 2.3} \\ 53.4_{\pm 2.2} \\ 54.8_{\pm 3.9} \end{array}$	$\begin{array}{c} 53.4_{\pm 4.1} \\ 53.2_{\pm 4.8} \\ 53.0_{\pm 4.8} \\ 54.8_{\pm 3.2} \\ 53.5_{\pm 3.6} \\ 53.3_{\pm 3.5} \\ \textbf{55.2}_{\pm 4.4} \end{array}$	$\begin{array}{c} 51.8_{\pm 4.9} \\ 51.6_{\pm 3.5} \\ 51.0_{\pm 5.2} \\ 50.8_{\pm 4.7} \\ 51.6_{\pm 5.0} \\ 50.7_{\pm 4.9} \\ \textbf{53.0}_{\pm 5.8} \end{array}$	$\begin{array}{c} 51.0_{\pm3.6} \\ 51.5_{\pm1.7} \\ 51.5_{\pm2.7} \\ 50.3_{\pm2.9} \\ 50.8_{\pm2.8} \\ 50.3_{\pm2.9} \\ 56.2_{\pm5.3} \end{array}$	$52.9_{\pm 4.7}$ $53.1_{\pm 4.7}$ $53.3_{\pm 4.7}$ $52.9_{\pm 3.6}$ $53.1_{\pm 3.5}$ $53.6_{\pm 4.1}$ $55.2_{\pm 4.7}$		

Table 4.7 Subject-Independent of Valence 5-fold Mean Classification Performance and Standard Deviation on DEAP.

We compare our best-performing TKEO-based features with recent fractal and deep learning approaches on the DEAP dataset (Table 4.9). While the Combined TKEO configuration achieves 54.2% and 51.1% accuracy for valence and arousal, respectively, multiscale fractal and deep models report considerably higher scores, often exceeding 60%. We observe a similar pattern to that seen in the SEED dataset, and this consistency across datasets suggests that

Features		Balance	ed Accura	acy (%)		ROC-AUC ($\times 10^2$)					
	Alpha	Beta	Gamma	Raw	Fused	Alpha	Beta	Gamma	Raw	Fused	
SE PSD	$\begin{array}{c} \hline 50.1_{\pm 0.9} \\ 50.6_{\pm 0.2} \end{array}$	$\overline{51.9_{\pm 2.0}}$ $50.3_{\pm 2.0}$	$\frac{51.5_{\pm 1.7}}{50.9_{\pm 0.8}}$	$\overline{49.3_{\pm 1.5}\atop 52.0_{\pm 2.4}}$	$51.9_{\pm 1.5}$ $50.7_{\pm 2.8}$	$51.3_{\pm 1.3}$ $50.2_{\pm 1.5}$	$\overline{52.3_{\pm 3.2}}$ $51.6_{\pm 2.6}$	$\frac{52.3_{\pm 2.3}}{50.3_{\pm 0.8}}$	$\overline{49.0_{\pm 2.5}}$ $50.3_{\pm 3.3}$	$52.8_{\pm 2.8}$ $50.9_{\pm 3.5}$	
TKEO-12 FB TKEO-25 FB TKEO-50 FB Selected-12 FB Selected-25 FB Selected-50 FB Combined	$\begin{array}{c} 51.5_{\pm 1.6} \\ 51.1_{\pm 1.2} \\ 50.8_{\pm 1.5} \\ 50.9_{\pm 1.3} \\ 51.4_{\pm 0.7} \\ 51.2_{\pm 1.7} \\ 51.7_{\pm 0.7} \end{array}$	$50.4_{\pm 1.4}$ $50.1_{\pm 1.6}$ $50.4_{\pm 1.9}$ $49.4_{\pm 0.3}$ $49.9_{\pm 0.8}$ $49.7_{\pm 0.6}$ $51.0_{\pm 1.6}$	$\begin{array}{c} 52.0_{\pm 1.4} \\ 51.1_{\pm 1.1} \\ 52.1_{\pm 1.5} \\ \textbf{52.2}_{\pm 1.5} \\ 51.5_{\pm 1.2} \\ 50.7_{\pm 2.1} \\ 51.4_{\pm 1.6} \end{array}$	$\begin{array}{c} 51.5_{\pm 2.7} \\ \textbf{52.1}_{\pm 1.7} \\ 50.1_{\pm 2.5} \\ 50.4_{\pm 1.5} \\ 50.8_{\pm 1.8} \\ 50.5_{\pm 1.4} \\ 51.1_{\pm 2.5} \end{array}$	$\begin{array}{c} 51.9_{\pm 1.4} \\ \textbf{52.3}_{\pm 1.0} \\ 52.1_{\pm 1.2} \\ 51.4_{\pm 1.6} \\ 52.1_{\pm 1.7} \\ 52.0_{\pm 1.0} \\ 52.0_{\pm 0.8} \end{array}$	$\begin{array}{c} 51.8_{\pm 1.9} \\ 51.7_{\pm 0.9} \\ 51.9_{\pm 1.6} \\ 51.5_{\pm 1.4} \\ 52.0_{\pm 2.1} \\ 51.5_{\pm 2.0} \\ 52.0_{\pm 0.8} \end{array}$	$49.9_{\pm 1.6}$ $50.5_{\pm 1.3}$ $50.9_{\pm 2.0}$ $49.1_{\pm 0.8}$ $49.8_{\pm 0.5}$ $50.2_{\pm 1.6}$ $52.2_{\pm 2.1}$	$\begin{array}{c} 52.8_{\pm 2.0} \\ 52.1_{\pm 1.5} \\ 52.8_{\pm 2.8} \\ \textbf{52.9}_{\pm 2.0} \\ 51.8_{\pm 1.7} \\ 51.0_{\pm 2.1} \\ 52.1_{\pm 2.8} \end{array}$	$51.6_{\pm 3.3}$ $52.4_{\pm 2.2}$ $50.7_{\pm 2.8}$ $51.1_{\pm 1.9}$ $50.9_{\pm 2.5}$ $51.4_{\pm 2.5}$ $51.4_{\pm 3.3}$	$\begin{array}{c} 52.0_{\pm 1.9} \\ \textbf{53.6}_{\pm 1.6} \\ 53.3_{\pm 2.0} \\ 52.1_{\pm 2.0} \\ 52.5_{\pm 2.3} \\ 52.5_{\pm 1.6} \\ 53.0_{\pm 1.6} \end{array}$	

Table 4.8 Subject-Independent of Arousal 5-fold Mean Classification Performance and Standard Deviation on DEAP.

deeper architectures are better suited to capturing the intricate dynamics of emotional EEG responses.

Features/Models	Valence – Arousal (%)
TKEO-25 FB (ours)	52.5 – 52.3
Combined TKEO (ours)	54.2 – 51.1
Multiscale Fractal Dimension [12]	56.6-63.1
Spectral topography maps of	59.2 – 55.7
different bands $+ \text{ CNN} [90]$	
Variational Mode Decomposition + DNN [90]	62.5 – 61.3

Table 4.9 Comparison of the Highest Reported Accuracies of the Proposed TKEO-based Features with State-of-the-Art Machine Learning Models on the DEAP Dataset for the Subject-Independent Task.

4.3 BCI-IV 2a Results

As shown in Tables 4.10 and 4.11, in the BCI-IV 2a dataset the Selected TKEO features consistently outperform all other feature sets in the Motor Imagery task in both settings. In Subject-Dependent setting, the fused-band yields the highest overall performance (Balanced Accuracy of 51.2%, ROC-AUC of 77.0), substantially exceeding chance level. Additionally, integrating TKEO features with baselines yields performance gains over the PSD baseline alone, highlighting their complementary nature. When comparing different filterbank configurations, we observe that employing more than 12 filters seems to improve performance in

most cases. This suggests that a finer filterbank provides higher spectral resolution, enabling the TKEO to capture narrowband EEG dynamics that are otherwise averaged out with fewer filters. Additionally, Beta band appears to perform better in TKEO-based features, when compared to the other single bands, which is consistent with Scherer et al. [100] for the Motor Imagery task.

Features		Balance	ed Accura	cy (%)		ROC-AUC $(\times 10^2)$						
	Alpha	Beta	Gamma	Raw	Fused	Alpha	Beta	Gamma	Raw	Fused		
SE PSD	$44.1_{\pm 14.7}\atop 40.7_{\pm 13.2}$	$43.6_{\pm 7.5}\atop38.2_{\pm 6.6}$	$37.6_{\pm 8.2}$ $28.3_{\pm 5.3}$	$40.4_{\pm 8.1}\atop43.2_{\pm 5.9}$	$47.1_{\pm 8.8}\atop40.6_{\pm 6.0}$	$70.4_{\pm 12.8}\atop 65.7_{\pm 13.4}$	$70.6_{\pm 8.0}\atop 67.4_{\pm 5.7}$	$\overline{66.3_{\pm 8.5}}$ $56.2_{\pm 6.3}$	$67.3_{\pm 8.4}$ $71.7_{\pm 6.1}$	$ 73.7_{\pm 8.2} 67.9_{\pm 7.7} $		
TKEO - 12 FB TKEO - 25 FB TKEO - 50 FB Selected - 12 FB Selected - 25 FB Selected - 50 FB Combined	$\begin{array}{c} 44.6_{\pm 12.6} \\ 43.4_{\pm 13.1} \\ 44.9_{\pm 13.1} \\ 45.4_{\pm 14.3} \\ \textbf{45.8}_{\pm 13.3} \\ 45.7_{\pm 13.5} \\ 42.7_{\pm 12.6} \end{array}$	$48.6_{\pm 10.3}\\48.4_{\pm 10.4}\\49.1_{\pm 11.3}$	$\begin{array}{c} 43.5_{\pm7.0} \\ 43.3_{\pm7.4} \\ 43.1_{\pm7.9} \\ 44.9_{\pm7.5} \\ \textbf{45.3}_{\pm7.1} \\ 45.2_{\pm7.4} \\ 31.3_{\pm6.3} \end{array}$	$45.9_{\pm 9.2}$	$50.1_{\pm 11.0}$	$68.9_{\pm 13.8}\atop 69.9_{\pm 13.5}\atop 71.2_{\pm 12.3}$	$74.6_{\pm 9.7}$ $74.9_{\pm 9.2}$ $74.8_{\pm 9.8}$ $75.0_{\pm 10.7}$ $76.1_{\pm 9.9}$ $76.1_{\pm 9.1}$ $68.3_{\pm 7.7}$	$\textbf{72.5}_{\pm 8.1}$	$\begin{array}{c} 72.7_{\pm 9.8} \\ 72.4_{\pm 9.7} \\ 72.4_{\pm 9.7} \\ 73.3_{\pm 11.4} \\ 73.0_{\pm 11.5} \\ \textbf{73.7}_{\pm 11.6} \\ 72.4_{\pm 6.8} \end{array}$	$74.9_{\pm 9.0}$ $75.4_{\pm 8.8}$ $75.0_{\pm 8.8}$ $75.8_{\pm 8.8}$ $76.3_{\pm 8.6}$ $77.0_{\pm 8.6}$ $68.6_{\pm 8.5}$		

Table 4.10 Subject-Dependent 5-fold Mean Classification Performance and Standard Deviation on BCI-IV 2a.

In the Subject-Independent setting (Table 4.10), we observe similar trends. Selected-50 FB features exhibit the highest Balanced Accuracy of 41.0% and ROC-AUC value of 66.8. Combining PSD with TKEO further improves performance, echoing the Subject-Dependent case. Likewise, using filterbanks with more than 12 bands consistently yields higher accuracy in both settings, suggesting that finer spectral resolution is beneficial. Among single-band models, the Beta band again provides the strongest results in this setting.

Features	Balanced Accuracy (%)					ROC-AUC (×10²)				
	Alpha	Beta	Gamma	Raw	Fused	Alpha	Beta	Gamma	Raw	Fused
SE PSD	$\overline{37.3_{\pm 6.8}}$ $36.1_{\pm 6.7}$	$35.1_{\pm 5.3}$ $35.6_{\pm 3.1}$	$ \begin{array}{r} \hline 32.8_{\pm 1.5} \\ 27.8_{\pm 2.2} \end{array} $	$\overline{35.3_{\pm 4.3}\atop 38.0_{\pm 5.8}}$	$\overline{37.4_{\pm 4.8}}$ $36.4_{\pm 5.0}$	$\overline{64.0_{\pm 6.1}\atop 62.3_{\pm 6.7}}$	$ 62.3_{\pm 4.8} 62.2_{\pm 4.0} $	$\overline{60.0_{\pm 1.3}\atop 54.1_{\pm 2.7}}$	$ 62.0_{\pm 4.5} 64.0_{\pm 6.0} $	$\overline{64.0_{\pm 5.0}\atop 63.0_{\pm 5.7}}$
TKEO - 12 FB TKEO - 25 FB TKEO - 50 FB Selected - 12 FB Selected - 25 FB Selected - 50 FB	$37.8_{\pm 8.3}$ $38.6_{\pm 7.6}$ $37.4_{\pm 7.4}$ $38.4_{\pm 8.0}$ $38.6_{\pm 8.1}$ $39.2_{\pm 9.1}$	$38.2_{\pm 6.2}$ $38.8_{\pm 6.6}$ $39.7_{\pm 7.9}$ $40.2_{\pm 8.8}$ $39.4_{\pm 7.9}$ $40.5_{\pm 7.9}$	$35.3_{\pm 3.9}$ $35.5_{\pm 2.6}$ $36.8_{\pm 2.3}$ $37.5_{\pm 3.3}$ $39.0_{\pm 3.1}$ $38.3_{\pm 3.1}$	$\begin{array}{c} 39.2_{\pm 6.1} \\ 39.7_{\pm 5.5} \\ 38.4_{\pm 4.8} \\ 40.0_{\pm 6.1} \\ \textbf{40.8}_{\pm 6.5} \\ 39.6_{\pm 6.8} \end{array}$	$38.4_{\pm 6.7}$ $39.5_{\pm 5.8}$ $39.1_{\pm 6.7}$ $39.9_{\pm 6.8}$ $39.8_{\pm 7.3}$ 41.0 _{±7.3}	$\begin{array}{c} 64.1_{\pm 7.3} \\ 65.2_{\pm 6.5} \\ 64.0_{\pm 6.9} \\ 64.9_{\pm 7.6} \\ 64.9_{\pm 7.4} \\ \textbf{65.4}_{\pm 7.9} \end{array}$	$\begin{array}{c} 65.0_{\pm 6.3} \\ 65.4_{\pm 6.2} \\ 66.1_{\pm 7.0} \\ 66.3_{\pm 7.2} \\ 66.2_{\pm 7.0} \\ 67.2_{\pm 6.8} \end{array}$	$62.8_{\pm 4.3}$ $63.0_{\pm 3.3}$ $63.2_{\pm 2.8}$ $63.8_{\pm 3.3}$ $64.7_{\pm 3.4}$ $65.0_{\pm 3.0}$	$65.5_{\pm 5.0}$ $65.3_{\pm 5.5}$ $64.4_{\pm 5.9}$ $65.9_{\pm 6.5}$ $66.0_{\pm 6.2}$ $66.0_{\pm 6.6}$	$65.3_{\pm 6.4}$ $65.9_{\pm 5.3}$ $65.4_{\pm 5.6}$ $66.6_{\pm 6.4}$ $66.2_{\pm 6.3}$ $66.8_{\pm 6.4}$
Combined	$37.0_{\pm 7.9}$	$36.5_{\pm 4.2}$	$32.8_{\pm 3.2}$	$37.6_{\pm 6.4}$	$37.3_{\pm 6.6}$	$64.0_{\pm 7.2}$		$60.0_{\pm 2.9}$	$64.8_{\pm 5.3}$	$64.2_{\pm 5.6}$

Table 4.11 Subject-Independent 5-fold Mean Classification Performance and Standard Deviation on BCI-IV 2a.

Additionally, we investigate the impact of each frequency band to the fused-band overall accuracies. As shown in Fig. 4.1, the SHAP [72] heatmap highlights elevated contributions in sensorimotor regions (C3, C4, CP3, CP4) in Alpha–Beta bands that capture event-related desynchronization/synchronization (ERD/ERS) during imagined movements. Such ERD is also evident in Fig. 3.5, where the Teager–Kaiser relative energy in the Alpha band shows a significant decrease during MI and increases during the resting periods. This pattern aligns with well-established neurophysiological findings of motor imagery [100], indicating that TKEO effectively captures the physiology of the brain.

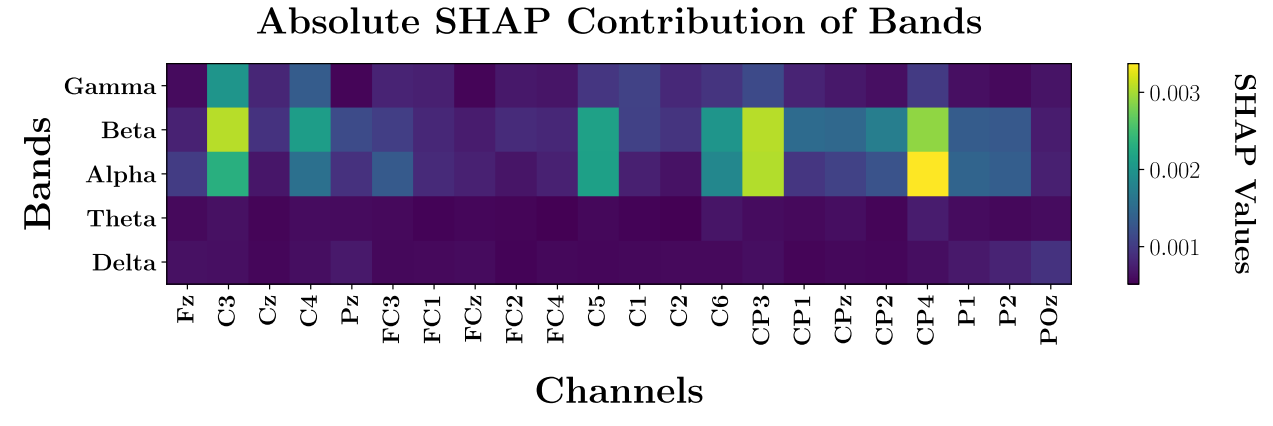


Figure 4.1 Absolute SHAP Values of Frequency Bands, indicating their contributions to Fused-band TKEO Predictions across EEG Channels in BCI-IV 2a; higher SHAP values represent greater contribution.

Features/Models	Accuracy (%)
EEG Image [120] RNN [120] Selected-25 FB (ours) Selected-50 FB (ours)	32.7 35.5 40.8 41.0
EEGNet [120] Convolutional Recurrent Attention Model [120]	51.3 59.1

Table 4.12 Comparison of the Highest Reported Accuracies of the Proposed TKEO-based Features with different Machine Learning Architectures proposed by [120] on the BCI-IV 2a Dataset for the Subject-Independent Task.

We compare our best-performing results with those reported by Zhang et al. [120] at Table 4.12, who evaluated several well-known machine learning models on the Motor Imagery task and proposed a novel approach of their own. While our results are below those of advanced deep learning models such as EEGNet (51.3%) and the Convolutional Recurrent Attention Model (59.1%), they exceed the results obtained with the RNN and EEG Image, which are simpler architectures. This indicates that the hand-crafted TKEO features contain meaningful information for motor imagery classification and serve as a competitive alternative when data resources are limited.

4.4 TUEP Results

In the TUEP dataset (Table 4.13), Combined features in almost all cases achieve the highest performance, highlighting the complementary nature of TKEO with the baseline features. In the Epilepsy Detection task, this complementarity between PSD and TKEO-based features is intuitive: TKEO likely captures the transient modulations that occur across different stages of epilepsy, while PSD may primarily reflect the ictal stage, where the EEG signal is dominated by a specific frequency component. Within the Combined features, the Gamma band achieves the highest Balanced Accuracy (78.4%)—approximately 15% higher than other feature sets—and the highest ROC-AUC (86.0). This result is consistent with previous findings indicating that epilepsy detection performance improves with higher-frequency EEG features [51]. Indicatively, we present in Fig. 4.2 the topology maps of the v-IFM features for an epileptic and a non-epileptic signal across frequency bands. The epileptic signal exhibits high variations in instantaneous frequency uniformly across the channels, in contrast to the non-epileptic one, where the variations are lower. This highlights the Gamma band frequency variations as a reliable indicator of epileptic activity.

Features	Balanced Accuracy (%)					ROC-AUC ($\times 10^2$)				
	Alpha	Beta	Gamma	Raw	Fused	Alpha	Beta	Gamma	Raw	Fused
SE PSD	$ 59.2_{\pm 2.5} 58.2_{\pm 2.4} $		$\overline{63.2_{\pm 8.4}}$ $61.7_{\pm 9.3}$		$\frac{61.4_{\pm 6.0}}{61.1_{\pm 7.6}}$		$ \begin{array}{r} \hline 64.5_{\pm 13.5} \\ 72.3_{\pm 13.6} \end{array} $			$ 75.5_{\pm 13.5} 74.2_{\pm 13.6} $
TKEO Selected Combined	$\begin{array}{c} 58.5_{\pm 2.3} \\ 59.0_{\pm 2.8} \\ \textbf{66.3}_{\pm 6.2} \end{array}$	$61.0_{\pm 0.9} \\ 60.0_{\pm 9.8} \\ \textbf{70.9}_{\pm 10.0}$	$61.6_{\pm 7.2}$	$58.7_{\pm 6.3}$	$61.2_{\pm5.9}$	$66.3_{\pm2.9}$		$70.3_{\pm 13.6}$	$70.5_{\pm 14.5}$	

Table 4.13 Subject-Independent 5-fold Mean Classification Performance and Standard Deviation on TUEP.

TKEO features alone achieve performance comparable to the baseline features, further underscoring their complementary contribution when combined. Interestingly, in the raw-band,

accuracies decrease in most cases relative to both the single-bands and fused-band, suggesting that the complementary effect of TKEO features diminishes when applied to wideband signals. This observation further emphasizes the narrowband sensitivity of the TKEO.

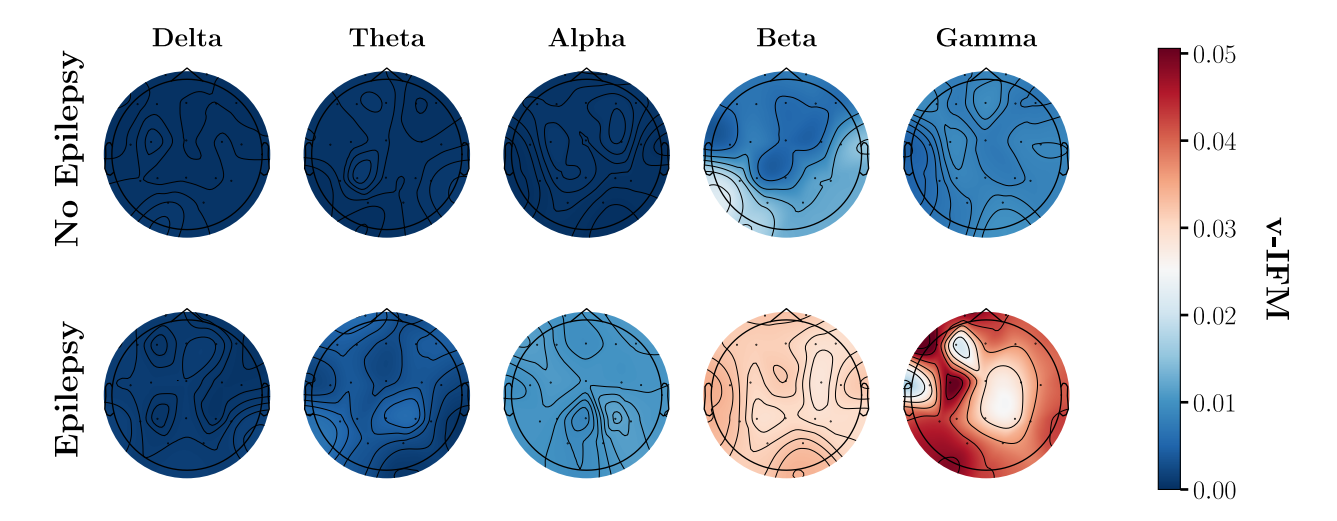


Figure 4.2 Topology Maps of EEG Channels from the TUEP Dataset across Frequency Bands of the v-IFM Feature.

We compare our best results with those reported by Uyttenhove et al. [111]. Since our model produces predictions for each 10-second EEG window, we align our evaluation with the window-level performance metrics they reported. In addition, we include results from a second state-of-the-art model described in [108]. Both studies report Sensitivity (Recall) and Specificity, allowing us to compute the corresponding Balanced Accuracy values. These are summarized in Table 4.14.

Features/Models	Accuracy (%)			
EEGNet [111]	64.4			
TKEO (ours)	64.8			
t-VGG Global Average Pooling [111]	76.2			
Combined TKEO (ours)	78.4			
Convolutional LSTM [108]	92.1			

Table 4.14 Comparison of the Highest Reported Accuracies of the Proposed TKEO-based Features with State-Of-The-Art Machine Learning Architectures on the TUEP Dataset for the Subject-Independent Task.

The proposed TKEO-based features achieve a Balanced Accuracy of 64.8%, comparable to EEGNet (64.4%), a compact CNN tailored for EEG decoding. This shows that the hand-crafted energy-based descriptors capture discriminative temporal patterns similar to those learned by deep models. When combined with additional features ("Combined"), the accuracy rises to 78.4%, confirming their complementary value. The Convolutional LSTM from [108] reaches 92.1%, benefiting from deeper spatio-temporal modeling and large-scale training. Although not matching this level, our method offers a lightweight and interpretable alternative suitable for limited-data or low-resource settings.

4.5 Ablation Study

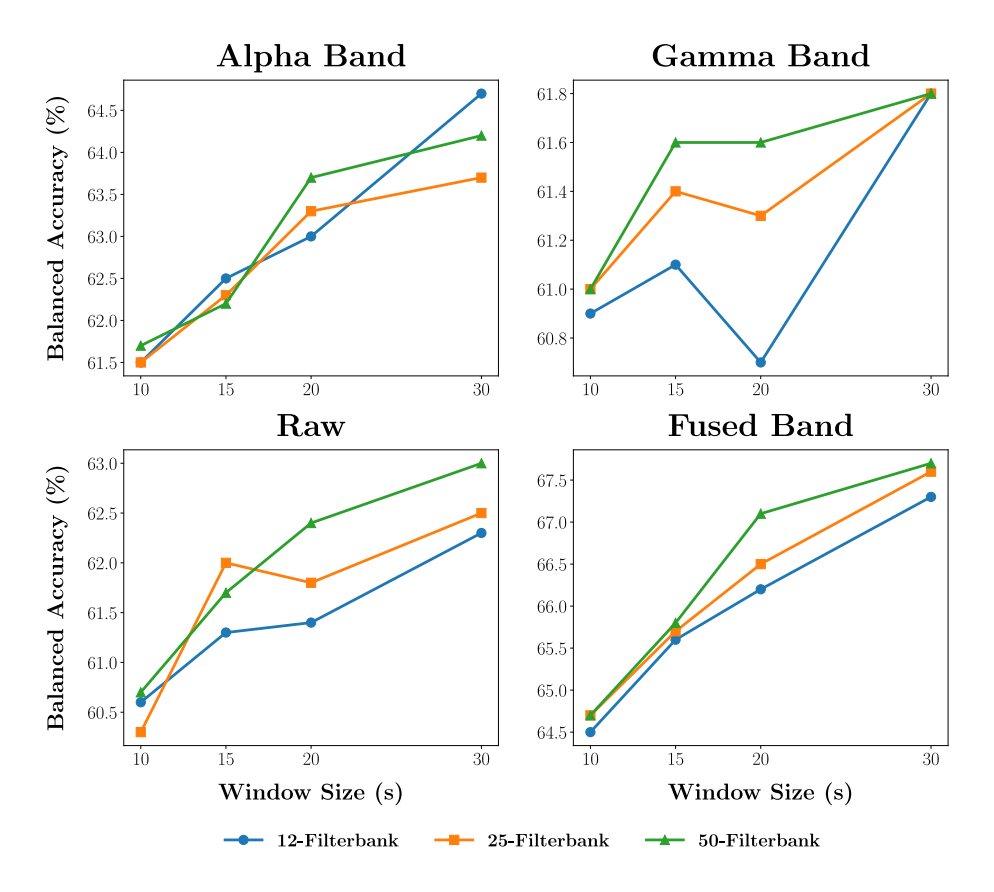


Figure 4.3 Comparison of Prediction Accuracies across Different Window Sizes and Filterbank Configurations on the SEED Dataset for the Subject-Independent Setting.

Since the number of filters is a key parameter in our approach, we further conducted an ablation study to analyze the effect of different filterbank configurations and window sizes

on the SEED dataset. The corresponding results are shown in Figures 4.3 and 4.4. We observe that increasing the window size leads to higher Balanced Accuracy, likely due to the longer temporal context available to the classifier. In the Alpha band (8–12 Hz), which is the narrowest among those considered, a 12-filter configuration provides sufficient frequency resolution to capture relevant EEG dynamics. Adding more filters does not yield meaningful improvements, suggesting that 12 filters offer an optimal balance between resolution and redundancy. For the wider bands—Gamma and raw—the filterbank configuration becomes more critical, as the broader spectral range benefits from having more filters to better resolve distinct frequency components. Finally, in the fused-band condition, we observe in the Subject-Independent setting that increasing the number of filters allows the TKEO to capture EEG energy dynamics more effectively, similar to the Gamma band. However, the performance gains are smaller, indicating that the number of filters has a less pronounced impact in the fused-band case than in the single Gamma band. This trend is not evident in the Subject-Dependent setting, where inter-subject variability generally leads to less consistent and less interpretable results.

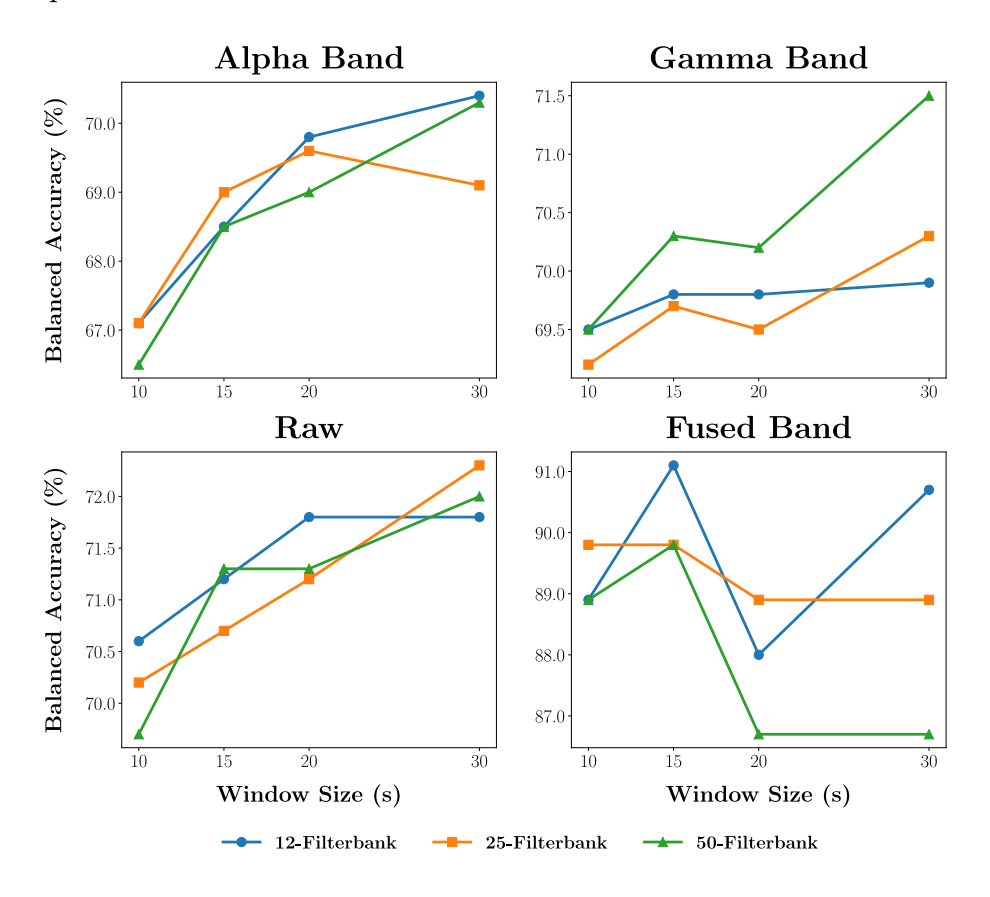


Figure 4.4 Comparison of Prediction Accuracies across Different Window Sizes and Filterbank Configurations on the SEED Dataset for the Subject-Dependent Setting.

4.6 Summary

The proposed TKEO-based features demonstrate superior relative performance in Motor Imagery and Epilepsy Detection tasks compared to Emotion Recognition. This observation underscores their effectiveness in applications characterized by transient temporal dynamics, while also revealing their limitations in domains where discriminative information is less temporally localized. Furthermore, the fused-band representation in most cases outperforms the other bands within the TKEO feature set, indicating the benefits of aggregating information across multiple frequency bands while maintaining the narrowband sensitivity inherent to the TKEO.

The integration of PSD and TKEO-based features generally leads to improved classification accuracy, emphasizing the complementary nature of spectral power and energy operator—based temporal information, especially in the Epilepsy Detection task. Our ablation study further confirms the robustness of the proposed approach, showing that increasing the window size improves Balanced Accuracy and that filterbank configurations must be adapted to the bandwidth of each frequency band to optimize performance.

Finally, comparisons across individual frequency bands yield results consistent with prior studies across all examined tasks. Although deep learning models generally achieve higher performance—particularly on emotion recognition datasets such as SEED and DEAP—the proposed approach outperforms other hand-crafted features like Differential Entropy and simpler architectures such as RNNs, demonstrating that TKEO-based features effectively capture meaningful temporal dynamics. Additionally, they offer interpretable, and physiologically meaningful representations of neural activity, providing a competitive alternative in scenarios with limited data or computational resources.

Chapter 5

Conclusion

In this Thesis, we systematically evaluated TKEO-based features across two tasks characterized by well-established transient dynamics—Motor Imagery and Epilepsy Detection—as well as in Emotion Recognition, which tests the method's applicability beyond its original motivating context. Through this evaluation, we clarified the strengths and limitations of TKEO features in EEG analysis and identified conditions under which it provides added value.

5.1 Summary of the Contributions

- 1. We propose a comprehensive set of EEG features derived from instantaneous energy analysis using the Teager–Kaiser Energy Operator (TKEO). These features include statistical descriptors, relative energy measures, and instantaneous amplitude and frequency components, the latter obtained via the DESA-1 demodulation algorithm.
- 2. To extract narrowband EEG components, we employ Gabor filterbanks with varying numbers of filters. Our results indicate that increasing the number of filters enhances predictive performance, as a finer filterbank provides higher spectral resolution to some extend. This improved resolution allows the TKEO to capture narrowband EEG dynamics that would otherwise be averaged out with coarser filterbanks, consistent with established TKEO theory.
- 3. We conduct a systematic evaluation of TKEO-derived features against conventional Power Spectral Density and Squared-Energy-based features across three representative EEG benchmark datasets, employing Support Vector Machine and Random Forest classifiers. The evaluation is performed under both Subject-Dependent and Subject-Independent settings to assess the generalizability of the proposed approach. Experi-

- mental results demonstrate that TKEO-based features achieve competitive or superior performance relative to baseline measures—improving classification accuracy in Motor Imagery and Epilepsy Detection tasks, while achieving comparable results to energy-based features in Emotion Recognition.
- 4. Through experimental analysis, we demonstrate that the TKEO provides complementary information to conventional energy measures, particularly in tasks characterized by transient and nonlinear EEG dynamics, thereby offering potential to enhance predictive accuracy.

5.2 Future Work

- 1. Integration of TKEO-based Features with Deep Learning: While deep learning models, particularly convolutional and transformer-based architectures [85], [90], [105], [108], [120], outperform the proposed approach in most benchmarks, TKEO-derived features demonstrated complementary properties and superior performance in simpler architectures such as RNNs. Future work could focus on hybrid architectures that integrate instantaneous energy features into deep networks—for example, by using TKEO-based feature maps as auxiliary inputs, attention cues, or regularization signals to enhance interpretability and robustness.
- 2. Adaptive Filterbanks: The current approach relies on fixed Gabor filterbanks for narrowband decomposition. Future research could explore adaptive or learnable filterbanks that jointly optimize the spectral decomposition and the TKEO feature extraction process. This would allow the system to tailor the frequency resolution to individual subjects or specific EEG tasks dynamically.
- 3. Combination with Temporal-Spatial Modeling: Future work could incorporate spatial information (e.g., electrode topology) and temporal context to better capture distributed EEG dynamics. The TKEO's sensitivity to instantaneous energy changes may complement spatiotemporal models that otherwise rely on global spectral patterns.
- 4. Extension to Additional EEG Paradigms: Building upon the current evaluation on emotion recognition, epilepsy detection, and motor imagery, future work could incorporate additional EEG tasks—such as attention monitoring, sleep stage classification, and complex sequential movement imagery—along with applications in neurore-habilitation and sports neuroscience, to further assess the versatility and robustness of TKEO-based features across diverse neural processes.

Appendix A

The SEED Dataset

The SJTU Emotion EEG Dataset (SEED) [122] is a multimodal corpus developed to support research in electroencephalography (EEG)-based emotion recognition. It was constructed at Shanghai Jiao Tong University with the aim of investigating the neural signatures of affective states and providing a benchmark dataset for affective computing, brain-computer interface (BCI) research, and computational neuroscience. The dataset has been made freely available for academic use via the Brain-Like Computing and Machine Intelligence (BCMI) laboratory at SJTU.

Stimuli Selection

The elicitation of reliable emotional responses is a fundamental requirement for emotion recognition research. In the SEED dataset, affective states were induced using film clips that provide audiovisual stimulation, which has been shown to be more effective than static images or music alone. Fifteen film excerpts were chosen for each experimental session, divided equally into positive, neutral, and negative emotional categories (five clips per category).

Each clip was approximately 4 minutes in duration and was drawn from Chinese-language films, ensuring cultural and linguistic consistency for the native Chinese participants. The clips were selected through a preliminary study to guarantee their ability to evoke the intended emotions. Unlike static picture paradigms or music-only protocols, film clips combine dynamic visual and auditory information, thereby facilitating immersion and yielding strong subjective and physiological responses.

Participants

A total of 15 healthy subjects (7 male, 8 female) participated in the SEED experiments. The mean age was 23.3 years (SD = 2.4). All participants were right-handed, had normal or corrected-to-normal vision, and reported normal hearing. Participants were recruited from the student population at Shanghai Jiao Tong University.

To ensure that subjects were able to elicit consistent emotions during the experiment, participants were screened using the Eysenck Personality Questionnaire (EPQ). Individuals with more stable moods and extraverted personality traits were prioritized, as such characteristics are associated with reliable affective elicitation in controlled laboratory settings.

Each participant completed the experiment twice, separated by at least one week. This design enables the assessment of intra-subject consistency of emotion-related EEG features across time (see Fig. A.1).



Figure A.1 Experimental Setup [122].

EEG Recording Experiment

Experiments were conducted in a quiet laboratory environment during the morning or early afternoon to minimize circadian effects.

- Recording system: EEG was recorded using an ESI NeuroScan system with a 62-channel electrode cap, positioned according to the international 10–20 system (see Fig. A.2).
- Sampling rate: Data were sampled at 1000 Hz.

- Additional signals: Electrooculogram (EOG) was also recorded to enable detection and correction of eye-movement artifacts. Frontal face video was captured via a camera positioned in front of the subject to monitor facial expressions and compliance.
- **Protocol:** Each experiment consisted of 15 trials corresponding to the 15 film clips. A 5-second cue preceded each clip. Following the clip, participants completed a 45-second self-assessment period and then rested for 15 seconds before the next trial.

Self-assessment questions, following Philippot's guidelines, probed participants on (1) the emotions they experienced while watching the clip, (2) whether they had seen the movie before, and (3) whether they understood the clip.

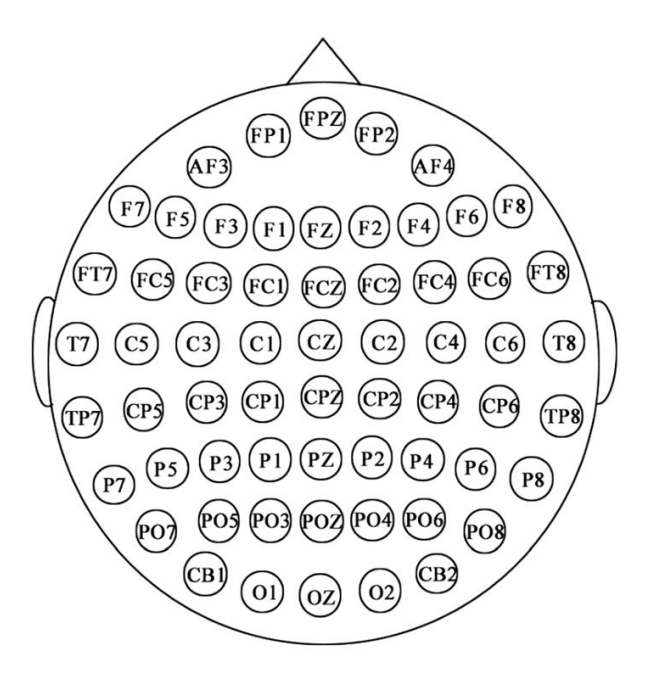


Figure A.2 62-Channel EEG Electrode Layout [122].

Data Preprocessing

The EEG data were subjected to a rigorous preprocessing pipeline to ensure signal quality:

- 1. **Epoch selection:** Only EEG segments corresponding to time periods where the target emotion was elicited were retained.
- 2. **Downsampling:** Raw EEG recordings were downsampled from 1000 Hz to 200 Hz.
- 3. Filtering: Signals were lowpass filtered at 75 Hz to remove high-frequency noise.

4. **Artifact rejection:** Segments heavily contaminated by muscle (EMG) or ocular (EOG) activity were manually removed. EOG channels were used to identify blink-related artifacts.

All signal processing was performed using MATLAB.

Availability

The SEED dataset is freely available for research purposes through the BCMI Lab at Shanghai Jiao Tong University. Both raw and preprocessed data are provided, along with stimulus details and participant self-reports. Access requires a request via the project website: bcmi.sjtu.edu.cn/home/seed.

Appendix B

The DEAP Dataset

The Database for Emotion Analysis using Physiological Signals (DEAP) [59] is a large-scale multimodal dataset designed for affective computing and brain-computer interface (BCI) research. Developed through a collaboration between Queen Mary University of London, the University of Geneva, the University of Twente, and EPFL, DEAP provides synchronized electroencephalogram (EEG), peripheral physiological, and facial video recordings alongside subjective self-reports of emotion. Its design was motivated by the need for high-quality, reproducible benchmarks for emotion recognition studies that combine neural and physiological measurements with naturalistic audiovisual stimuli.

The dataset has become one of the most widely used resources in computational neuroscience and affective computing due to its scale, multimodality, and innovative semi-automated stimulus selection process.

Stimuli Selection

Selecting appropriate affective stimuli is a central challenge for emotion recognition research. DEAP employed a three-stage strategy to construct a balanced and validated set of music video clips capable of eliciting diverse emotions.

Initial Collection

An initial pool of 120 candidate videos was compiled using both automated and manual strategies. Sixty videos were identified through the Last.fm online music platform, where user-generated emotional tags such as depressing, aggressive, or happy were exploited to retrieve songs strongly associated with affective descriptors. From over 1000 tagged songs, subsets were curated to represent each quadrant of the valence—arousal space (low/high arousal

crossed with low/high valence) [59]. To minimize cultural mismatch, preference was given to European and North American artists, aligning with the participant demographic.

The remaining 60 videos were selected manually by researchers, ensuring clear emotional relevance and even coverage across the four quadrants. Each song was required to have an accessible music video and to be contextually suitable for laboratory testing.

Affective Highlight Detection

To ensure that participants were exposed to emotionally salient segments, a content-based affective highlight detection method was applied. Each music video was segmented into overlapping one-minute excerpts. Acoustic and visual features—including loudness, motion intensity, color variance, and lighting—were extracted and mapped to valence and arousal dimensions using regression models trained on annotated movie datasets. The one-minute segment with the highest emotional salience score was retained as the candidate highlight. In a few cases, highlights were manually adjusted to capture well-known or particularly evocative sections of the song [59].

Online Annotation and Final Selection

A large-scale web-based subjective assessment was conducted to evaluate the 120 one-minute highlights. Each clip was rated by 14–16 volunteers on discrete 9-point scales for valence, arousal, and dominance. To maximize emotional clarity and reduce variability, 40 clips were chosen for the final laboratory experiment. The selection was balanced across quadrants of the normalized valence—arousal space, with preference given to clips eliciting strong, consistent responses. Of these, 17 originated from the Last.fm tag-based retrieval, validating the semi-automated selection procedure. The distribution of candidate and selected stimuli across the valence—arousal space is shown in Fig. B.1.

Participants

The experimental dataset includes recordings from 32 healthy adult volunteers, equally balanced across gender (16 male, 16 female). Participants were aged between 19 and 37 years (Average Age = 26.9).

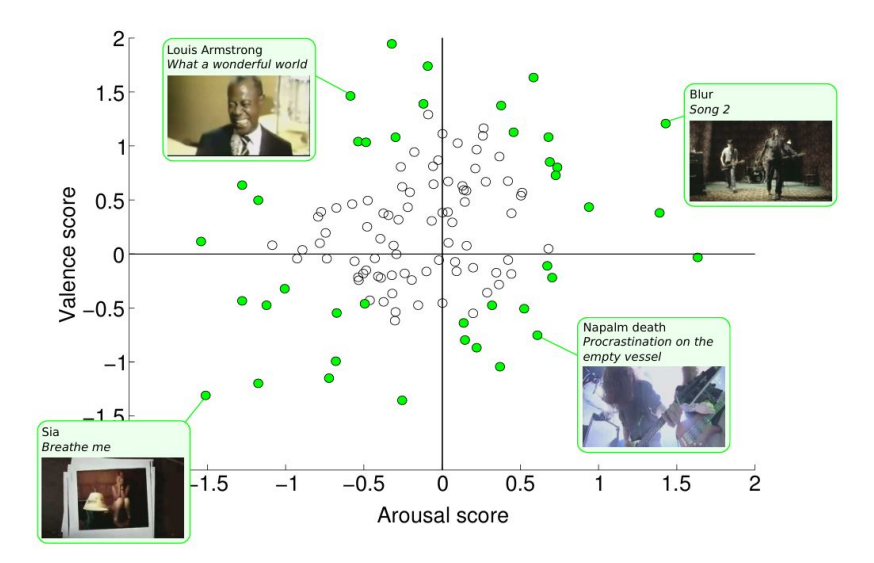


Figure B.1 Distribution of the 120 Candidate Music Video Stimuli in the Valence–Arousal Space, based on Online Subjective Ratings. The 40 Final Clips used in the DEAP Experiment are Highlighted in Green [59].

EEG and Physiological Recording

Recording Environment and Hardware

Recordings were conducted in controlled laboratory environments with consistent illumination. A BioSemi ActiveTwo system was used to capture EEG data at a sampling rate of 512 Hz across 32 AgCl electrodes placed according to the international 10–20 system.

In addition to EEG, thirteen peripheral physiological signals were acquired, including:

- Electrooculogram (EOG) from electrodes around the eyes.
- Electromyogram (EMG) from the zygomaticus major and trapezius muscles.
- Galvanic skin response (GSR) measured via two channels.
- Blood volume pressure (BVP) via plethysmography.
- Skin temperature.
- Respiration.

For 22 participants, frontal face video was also recorded using a consumer-grade digital camcorder, providing complementary behavioral data on facial expressions.

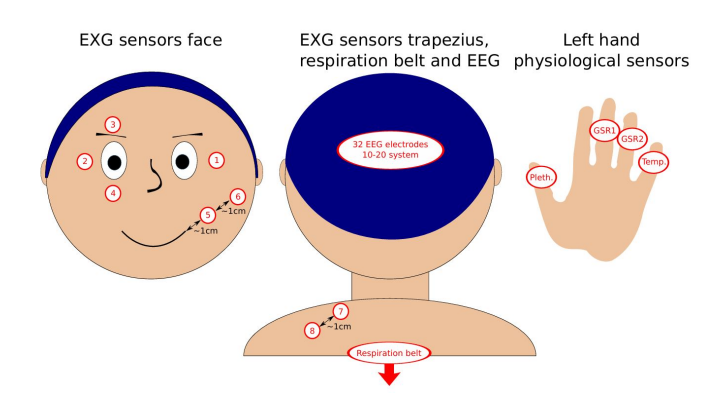


Figure B.2 Placement of Physiological Sensors [59].

Experiment Protocol

Each participant completed a single experimental session consisting of 40 trials, one per selected music video. The procedure was as follows:

- 1. A 2-minute resting baseline with fixation cross.
- 2. A trial sequence including:
 - 2-second trial indicator.
 - 5-second fixation baseline.
 - 60-second music video presentation.
 - Self-assessment of emotional state.
- 3. After 20 trials, participants were given a short break, during which signal quality and electrode placement were checked.

Stimuli were presented on a 17-inch screen at 800×600 resolution, approximately one meter from the participant. Stereo speakers delivered audio at a comfortable, individually adjusted volume. Synchronization markers ensured precise alignment of multimedia presentation and physiological recording.

Self-Assessment Procedure

Following each video, participants reported their affective responses using Self-Assessment Manikins (SAM). Four continuous 9-point scales were employed:

• Valence: ranging from unpleasant to pleasant.

- Arousal: ranging from calm/bored to excited/alert.
- **Dominance:** ranging from submissive to empowered.
- **Liking:** ranging from strong dislike to strong liking.

The SAM figures (and thumbs-down/up symbols for liking) were displayed with numerical anchors (1–9). Participants indicated their response by clicking with a mouse, producing a quasi-continuous measure.

At the end of the experiment, participants also provided familiarity ratings for each song on a 1–5 scale, ranging from "never heard before" to "knew very well."

Data Preprocessing

To ensure consistency and usability of the signals, the DEAP dataset includes both raw and preprocessed data:

- 1. **EEG downsampling:** Raw EEG sampled at 512 Hz was downsampled to 128 Hz.
- 2. **Filtering:** A bandpass filter between 4–45 Hz was applied to remove slow drifts and high-frequency noise.
- 3. **Artifact handling:** EOG channels were retained to enable ocular artifact correction. Segments with extreme contamination were excluded.
- 4. **Referencing:** Signals were re-referenced to the common average.

Both EEG and peripheral channels were released in MATLAB format, enabling straightforward use in machine learning pipelines.

Availability

The DEAP dataset is freely available for academic research purposes through Queen Mary University of London's repository: eecs.qmul.ac.uk/mmv/datasets/deap.

Appendix C

The BCI-IV 2a Dataset

The BCI Competition IV dataset 2a [20] is a benchmark corpus designed for the evaluation of electroencephalography (EEG)-based motor imagery (MI) brain—computer interfaces (BCIs). It was created at Graz University of Technology and released as part of the 2008 BCI Competition series. The dataset was specifically constructed to enable rigorous comparison of algorithms for multiclass motor imagery classification, a central challenge in BCI research. It provides high-quality, artifact-annotated EEG data along with standardized evaluation protocols, making it one of the most widely used resources in motor imagery decoding, signal processing, and machine learning research for BCIs.

Experimental Paradigm

The dataset consists of EEG recordings from 9 healthy subjects, each of whom participated in two sessions recorded on different days. The paradigm was a cue-based motor imagery task involving four distinct classes:

- Left hand motor imagery (class 1)
- Right hand motor imagery (class 2)
- Both feet motor imagery (class 3)
- Tongue motor imagery (class 4)

Each session comprised 6 runs, separated by short breaks. Each run contained 48 trials (12 per class), yielding a total of 288 trials per session and 576 trials per subject across both sessions.

At the beginning of each session, a 5-minute EOG calibration block was recorded to capture

ocular artifacts. This calibration consisted of three segments: two minutes eyes open, one minute eyes closed, and one minute with deliberate eye movements. Due to technical issues, subject A04 performed only the eye movement condition.

The timing protocol of each trial was as follows. At t = 0 s, a fixation cross appeared at the center of the screen together with a warning tone. At t = 2 s, a directional cue (arrow left, right, down, or up) was presented for 1.25 s, instructing the subject which imagery to perform. Subjects carried out the mental task until t = 6 s, when the fixation cross disappeared. A variable inter-trial interval with a blank screen followed before the next trial.

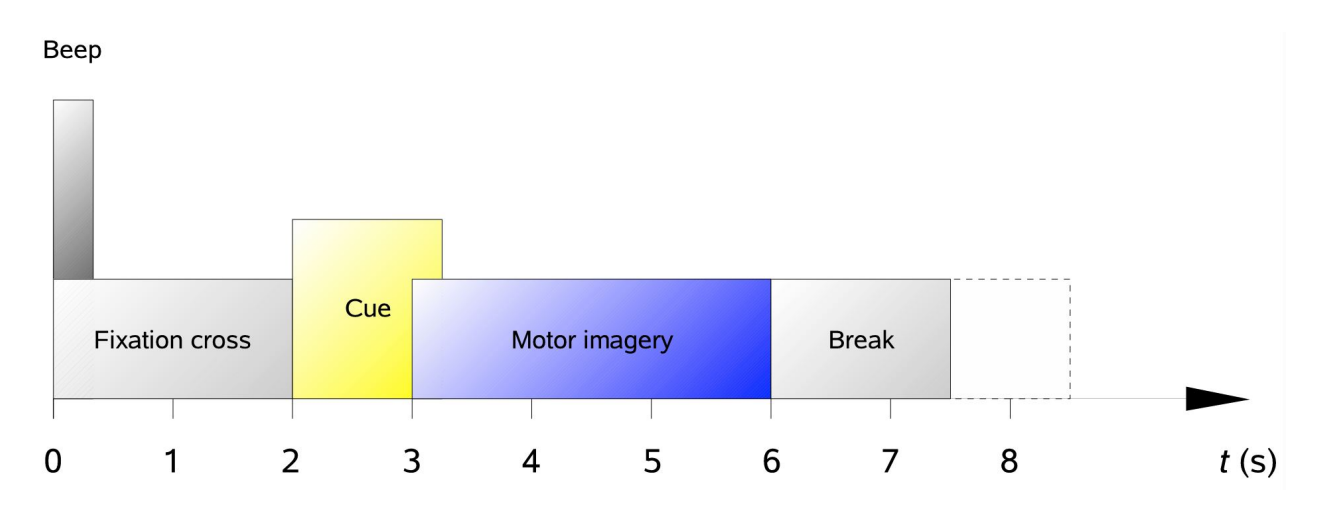


Figure C.1 Timing scheme of one trial in the BCI Competition IV 2a Dataset [20].

EEG Recording

EEG was recorded using 22 Ag/AgCl electrodes positioned according to the international 10-20 system with an inter-electrode spacing of 3.5 cm. The left mastoid served as reference, and the right mastoid as ground.

• Sampling rate: 250 Hz

• Bandpass filter: 0.5–100 Hz

• Notch filter: 50 Hz (to remove line noise)

• Amplifier sensitivity: 100 μV

Additionally, three monopolar EOG channels were recorded with the same sampling and filtering settings (amplifier sensitivity: 1 mV). These channels were included for artifact detection and correction but were not intended for classification.

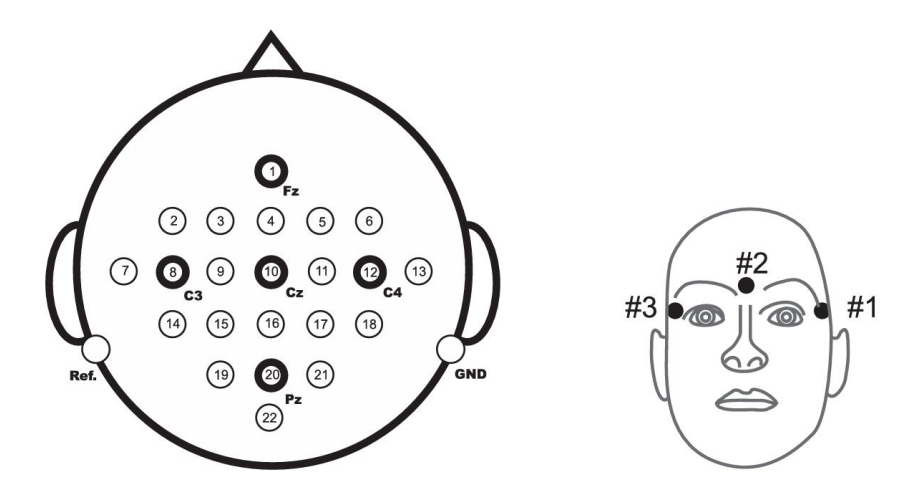


Figure C.2 Electrode montage for EEG (left) and EOG (right) recordings [20].

The EEG recordings are provided in the General Data Format (GDF), with one file corresponding to each subject and session. For every subject, one session is designated as the labeled training set, while the other is reserved as the unlabeled evaluation set. Alongside the raw signals, event annotations are included to mark trial onsets, cue presentations, calibration periods, and segments excluded due to artifacts. Class labels corresponding to motor imagery tasks (left hand, right hand, feet, and tongue) are available only for the training data, whereas the evaluation set remains unlabeled in order to support standardized benchmarking of algorithm performance.

Availability

The BCI Competition IV 2a dataset is freely available for academic research. It includes EEG and EOG recordings together with artifact annotations and event markers, providing a comprehensive benchmark for motor imagery studies. The dataset can be obtained from the official competition website: bbci.de/competition/iv.

Appendix D

The TUEP Dataset

The Temple University Hospital EEG (TUH-EEG) Corpus [112] is the largest publicly accessible database of clinical electroencephalographic recordings. It was developed at Temple University as part of the Neural Engineering Data Consortium (NEDC) and represents over 14 years of routine clinical practice. The corpus was designed to provide a resource for computational neuroscience, clinical decision support, and machine learning applied to EEG interpretation. In contrast to research-oriented datasets collected under tightly controlled laboratory conditions, TUH-EEG captures the heterogeneity of real-world clinical data, including variability in electrode montages, equipment, sampling rates, and patient populations. This diversity makes the dataset particularly valuable for developing robust algorithms capable of generalizing to uncontrolled environments.

Data Collection and Processing

The recordings are stored in the European Data Format (EDF), a widely adopted standard that ensures compatibility with common signal processing and analysis tools. To protect patient privacy, all personally identifiable information—such as names, dates of birth, and medical record numbers—was thoroughly removed. Each patient was assigned a randomized identifier, allowing the data to remain anonymous while still preserving the ability to track multiple sessions from the same individual. Each EEG study was paired with its corresponding physician report, which summarizes the clinical history, relevant medications, and diagnostic impressions. Only sessions with both valid EEG recordings and associated reports were included in the curated release.

The corpus follows a hierarchical directory structure: patients are grouped in batches of approximately one hundred, each with subfolders for individual recording sessions. A session folder contains one or more EEG files in EDF format and the associated physician report

in plain text. Long-term monitoring sessions are split into multiple EDF segments, allowing manageable file sizes and session-level organization.

The TUH EEG Epilepsy Corpus (TUEP)

Within the broader TUH-EEG collection, a subset known as the *TUH EEG Epilepsy Corpus* (*TUEP*) has been defined to specifically support research in epilepsy. While TUH-EEG includes diverse neurological conditions, TUEP emphasizes cases in which epilepsy-related pathology is present and well-documented. TUEP distills these cases into a structured dataset that can be used to train and evaluate automated systems for epilepsy-related analysis.

The TUEP dataset comprises EEG recordings and reports from 200 patients. Of these, 100 patients were diagnosed with epilepsy and 100 patients were classified as non-epileptic controls. The corpus contains 698 sessions in total, of which 530 sessions (1785 EEG files) are from the epilepsy group and 168 sessions (513 EEG files) from the control group. These figures reflect the state of the corpus at the time of analysis; however, the dataset is continuously updated, and new recordings are periodically incorporated.

EEG Recording

The TUEP dataset shows substantial variability in the number of EEG channels across recordings, reflecting differences in clinical acquisition protocols based on the international 10–20 system. Recordings were sampled at either 250 Hz or 256 Hz. In addition to EEG, electrocardiogram (EKG) channels were also recorded to provide complementary physiological information.

Availability

The TUH EEG Epilepsy Corpus is freely available for academic use through the Neural Engineering Data Consortium (NEDC) at Temple University. Data are distributed in EDF format along with de-identified neurologist reports. Access requires registration on the NEDC website: isip.piconepress.com/projects/nedc/html/tuh eeg.

Appendix E

List of Publications

This Thesis has resulted in a paper that is currently under review for ICASSP 2026:

• I. Chourdaki, K. Avramidis, C. Garoufis, A. Zlatintsi, P. Maragos, "Teager-Kaiser Energy Methods For EEG Feature Extraction In Biomedical Applications," under review for the *Proc. of the International Conference on Acoustics, Speech and Signal Processing (ICASSP)*, IEEE, 2026.

During the course of this Thesis, we also participated in the Signal Processing Grand Challenge on EEG-based Music Emotion Recognition, hosted at ICASSP 2025, where our team won third place in the competition, and the work was subsequently published:

• C. Garoufis, M. Glytsos, I. Chourdaki, P.P. Filntisis and P. Maragos, "Power in Unity: Combining in-Domain and out-of-Domain Pre-Training Strategies for EEG-Based Person Identification," in *Proc. International Conference on Acoustics, Speech and Signal Processing (ICASSP)*, IEEE, April, 2025.

- [1] Abdi-Sargezeh, B., Oswal, A., and Sanei, S., "Mapping Scalp to Intracranial EEG using Generative Adversarial Networks for Automatically Detecting Interictal Epileptiform Discharges," in *Proc. IEEE Statistical Signal Processing Workshop (SSP)*, Jul. 2023.
- [2] Abdi-Sargezeh, B., Shirani, S., Sanei, S., Took, C., Geman, O., Alarcon, G., and Valentin, A., "A review of signal processing and machine learning techniques for interictal epileptiform discharge detection," *Comput. Biol. Med.*, vol. 168, p. 107782, Jan. 2024.
- [3] Abdi-Sargezeh, B., Shirani, S., Valentin, A., Alarcon, G., and Sanei, S., "EEG-to-EEG: Scalp-to-Intracranial EEG Translation Using a Combination of Variational Autoencoder and Generative Adversarial Networks," *Sensors*, vol. 25, no. 2, Jan. 2025.
- [4] Abdi-Sargezeh, B., Shirani, S., Valentin, A., Alarcon, G., and Sanei, S., "EEG-to-EEG: Scalp-to-Intracranial EEG Translation Using a Combination of Variational Autoencoder and Generative Adversarial Networks," *Sensors*, vol. 25, no. 2, p. 494, Jan. 2025.
- [5] Abo-Zahhad, M., Ahmed, S., and Abbas, S., "A New EEG Acquisition Protocol for Biometric Identification Using Eye Blinking Signals," *International Journal of Intelligent Systems and Applications*, vol. 7, no. 6, pp. 48–54, May 2015.
- [6] Alarcao, S. and Fonseca, M., "Emotions recognition using EEG signals: A survey," *IEEE transactions on affective computing*, vol. 10, no. 3, pp. 374–393, Jun. 2017.
- [7] Alarcão, S. M. and Fonseca, M. J., "Emotions Recognition Using EEG Signals: A Survey," *IEEE Transactions on Affective Computing*, vol. 10, no. 3, pp. 374–393, Jun. 2019.
- [8] Ang, K. and Guan, C., "EEG-Based Strategies to Detect Motor Imagery for Control and Rehabilitation," *IEEE Transactions on Neural Systems and Rehabilitation Engineering*, vol. 25, no. 4, pp. 392–401, Dec. 2017.

[9] Apicella, A., Arpaia, P., D'Errico, G., Marocco, D., Mastrati, G., Moccaldi, N., and Prevete, R., "Toward cross-subject and cross-session generalization in EEG-based emotion recognition: Systematic review, taxonomy, and methods," *Neurocomputing*, vol. 604, p. 128 354, Nov. 2024.

- [10] Artinis Medical Systems, "What Is the 10-20 System for EEG?," Jan. 2024, Available: https://info.tmsi.com/blog/the-10-20-system-for-eeg.
- [11] Asadi-Pooya, A., Brigo, F., Lattanzi, S., and Blumcke, I., "Adult epilepsy," *The Lancet*, vol. 402, no. 10399, pp. 412–424, Jul. 2023.
- [12] Avramidis, K., Zlatintsi, A., Garoufis, C., and Maragos, P., "Multiscale Fractal Analysis on EEG Signals for Music-Induced Emotion Recognition," in *Proc. 29th European Signal Processing Conf. (EUSIPCO)*, Aug. 2021.
- [13] Badani, S., Saha, S., Kumar, A., Chatterjee, S., and Bose, R., "Detection of Epilepsy Based on Discrete Wavelet Transform and Teager-Kaiser Energy Operator," in *Proc. IEEE Calcutta Conf. (CALCON)*, IEEE, Dec. 2017.
- [14] Bajaj, N., "Wavelets for EEG Analysis," in Wavelet Theory, IntechOpen, Feb. 2021.
- [15] Besharat, A. and Samadzadehaghdam, N., "Improving Upper Limb Movement Classification from EEG Signals Using Enhanced Regularized Correlation-Based Common Spatio-Spectral Patterns," *IEEE Access*, vol. 13, pp. 71432–71446, Jun. 2025.
- [16] Bin Ng, W., Saidatul, A., Chong, Y., and Ibrahim, Z., "PSD-Based Features Extraction for EEG Signal During Typing Task," *IOP Conference Series: Materials Science and Engineering*, vol. 557, no. 1, p. 012032, Jun. 2019.
- [17] BioRender, "Electroencephalography (EEG) Recording," 2025, Available: https://www.biorender.com/template/electroencephalography-eeg-recording.
- [18] Breiman, L., "Random forests," Machine learning, vol. 45, no. 1, pp. 5–32, 2001.
- [19] Brodersen, K., Ong, C., Stephan, K., and Buhmann, J., "The Balanced Accuracy and Its Posterior Distribution," in *Proc. 20th Int'l Conf. on Pattern Recognition*, IEEE, Aug. 2010.
- [20] Brunner, C., Leeb, R., Müller-Putz, G., Schlögl, A., and Pfurtscheller, G., "Bci competition 2008–graz data set a," *Institute for knowledge discovery (laboratory of brain-computer interfaces)*, Graz University of Technology, vol. 16, no. 1-6, p. 34, 2008.
- [21] Chandra, M. and Bedi, S., "Survey on SVM and their application in image classification," *Int. J. Inf. Technol.*, vol. 13, no. 5, pp. 1–11, Oct. 2021.

[22] Chatterjee, S., "Detection of focal electroencephalogram signals using higher-order moments in EMD-TKEO domain," *Healthcare Technology Letters*, vol. 6, no. 3, pp. 64–69, May 2019.

- [23] Choi, J., Kim, K., Jeong, J., Kim, L., Lee, S., and Kim, H., "Developing a motor imagery-based real-time asynchronous hybrid BCI controller for a lower-limb exoskeleton," *Sensors* (*Basel*), vol. 20, no. 24, p. 7309, Dec. 2020.
- [24] Chowdary, M., Anitha, J., and Hemanth, D., "Emotion Recognition from EEG Signals Using Recurrent Neural Networks," *Electronics*, vol. 11, no. 15, p. 2387, Jul. 2022.
- [25] Cobb, W., Gastaut, H., Hess Jr, R., Jung, R., Magnus, O., and Terzian, H., "Report of the Committee on Methods of Clinical Examination in Electroencephalography," Electroencephalogr. Clin. Neurophysiol, vol. 10, no. 2, pp. 370–375, 1957.
- [26] Comon, P., "Independent component analysis, A new concept?" Signal Processing, vol. 36, no. 3, pp. 287–314, Apr. 1994.
- [27] Cooley, J. and Tukey, J., "An algorithm for the machine calculation of complex fourier series," *Mathematics of computation*, vol. 19, no. 90, pp. 297–301, Apr. 1965.
- [28] Cortes, C. and Vapnik, V., "Support-Vector Networks," *Machine learning*, vol. 20, no. 3, pp. 273–297, Sep. 1995.
- [29] Das, A. B. and Bhuiyan, M. I. H., "Discrimination and classification of focal and non-focal EEG signals using entropy-based features in the EMD-DWT domain," *Biomedical Signal Processing and Control*, vol. 29, pp. 11–21, Aug. 2016.
- [30] Davak, A., Tomar, P., and Garud, N., "A Comprehensive Review on Epilepsy and Its Diagnosis/Treatment Using EEG Signals," *EPH International Journal of Medical and Health Science*, vol. 11, no. 1, pp. 103–114, May 2025.
- [31] Decety, J., "Do imagined and executed actions share the same neural substrate?" *Cognitive Brain Research*, vol. 3, no. 2, pp. 87–93, Mar. 1996.
- [32] Decety, J. and Jeannerod, M., "Mentally simulated movements in virtual reality: does Fitt's law hold in motor imagery?" *Behavioural Brain Research*, vol. 72, no. 1–2, pp. 127–134, Dec. 1995.
- [33] Dewey, J., "The theory of emotion.," Psychological Review, vol. 2, no. 1, p. 13, 1895.
- [34] Dimitriadis, D., Maragos, P., and Potamianos, A., "Robust AM-FM Features for Speech Recognition," *IEEE Signal Processing Letters*, vol. 12, no. 9, pp. 621–624, Sep. 2005.

[35] Dunn, D. and Higgins, W., "Optimal Gabor filters for texture segmentation," *IEEE Transactions on Image Processing*, vol. 4, no. 7, Jul. 1995.

- [36] Ekman, P., "An argument for basic emotions," Cognition & emotion, vol. 6, no. 3-4, pp. 169–200, May 1992.
- [37] Ekman, P. and Friesen, W., "Constants across cultures in the face and emotion," Journal of Personality and Social Psychology, vol. 17, no. 2, p. 124, Feb. 1971.
- [38] Feng, Y., Li, Q., and Guan, X., "Entropy of teager energy in wavelet-domain algorithm applied in note onset detection," in *Proc. 7th Int'l Conf. on Natural Computation*, Jul. 2011.
- [39] Fisher, R., Acevedo, C., Arzimanoglou, A., Bogacz, A., Cross, J., Elger, C., Engel Jr, J., Forsgren, L., French, J., Glynn, M., Hesdorffer, D., Lee, B., Mathern, G., Moshé, S., Perucca, E., Scheffer, I., Tomson, T., Watanabe, M., and Wiebe, S., "ILAE official report: A practical clinical definition of epilepsy," *Epilepsia*, vol. 55, no. 4, pp. 475–482, Apr. 2014.
- [40] Fisher, R., Cross, J., French, J., Higurashi, N., Hirsch, E., Jansen, F., Lagae, L., Moshé, S., Peltola, J., Roulet Perez, E., Scheffer, I., and Zuberi, S., "Operational classification of seizure types by the International League Against Epilepsy: Position Paper of the ILAE Commission for Classification and Terminology," *Epilepsia*, vol. 58, no. 4, pp. 522–530, Mar. 2017.
- [41] Fürbass, F., Kural, M., Gritsch, G., Hartmann, M., Kluge, T., and Beniczky, S., "An artificial intelligence-based EEG algorithm for detection of epileptiform EEG discharges: Validation against the diagnostic gold standard," *Clinical Neurophysiology*, vol. 131, no. 6, pp. 1174–1179, Jun. 2020.
- [42] Gong, L., Li, M., Zhang, T., and Chen, W., "EEG emotion recognition using attention-based convolutional transformer neural network," *Biomedical Signal Processing and Control*, vol. 84, p. 104 835, Jul. 2023.
- [43] Goudjil, M., Koudil, M., Bedda, M., and Ghoggali, N., "A novel active learning method using SVM for text classification," *Int. J. Autom. Comput.*, vol. 15, no. 3, pp. 290–298, Jun. 2018.
- [44] Gupta, A., Kumar, D., Verma, H., Tanveer, M., Javier, A., Lin, C.-T., and Prasad, M., "Recognition of multi-cognitive tasks from EEG signals using EMD methods," Neural Computing and Applications, vol. 35, no. 31, pp. 22989–23006, Jun. 2022.
- [45] Hanley, J. and McNeil, B., "The meaning and use of the area under a receiver operating characteristic (ROC) curve.," *Radiology*, vol. 143, no. 1, pp. 29–36, Apr. 1982.

[46] Hanson, H., Maragos, P., and Potamianos, A., "A system for finding speech formants and modulations via energy separation," *IEEE Transactions on Speech and Audio Processing*, vol. 2, no. 3, pp. 436–443, Jul. 1994.

- [47] Hyvarinen, A., "Fast and robust fixed-point algorithms for independent component analysis," *IEEE Transactions on Neural Networks*, vol. 10, no. 3, pp. 626–634, May 1999.
- [48] Iasemidis, L., Principe, J., and Sackellares, J., "Measurement and Quantification of Spatiotemporal Dynamics of Human Epileptic Seizures," in *Nonlinear Biomedical Signal Processing: Dynamic Analysis and Modeling, Volume II*, M. Akay, Ed., vol. 2, Sep. 2000, pp. 294–318.
- [49] Istvanek, M., Smekal, Z., Spurny, L., and Mekyska, J., "Enhancement of Conventional Beat Tracking System Using Teager-Kaiser Energy Operator," Applied Sciences, vol. 10, no. 1, p. 379, Jan. 2020.
- [50] Ji, Y., Chang, K., and Hung, C.-C., "Efficient edge detection and object segmentation using gabor filters," in *Proc. of the 42nd Annual ACM Southeast Conf.*, Apr. 2004.
- [51] Jiang, X., Liu, X., Liu, Y., Wang, Q., Li, B., and Zhang, L., "Epileptic seizures detection and the analysis of optimal seizure prediction horizon based on frequency and phase analysis," *Frontiers in Neuroscience*, vol. 17, p. 1191683, May 2023.
- [52] Jonas, S., Rossetti, A., Oddo, M., Jenni, S., Favaro, P., and Zubler, F., "EEG-based outcome prediction after cardiac arrest with convolutional neural networks: Performance and visualization of discriminative features," *Human brain mapping*, vol. 40, no. 16, pp. 4606–4617, Jul. 2019.
- [53] Jung, T.-P., Makeig, S., Humphries, C., Lee, T.-W., Mckeown, M., Iragui, V., and Sejnowski, T., "Removing electroencephalographic artifacts by blind source separation," *Psychophysiology*, vol. 37, no. 2, pp. 163–178, Mar. 2000.
- [54] Kaiser, J., "On a simple algorithm to calculate the 'energy' of a signal," in *Proc. Int'l Conf. on Acoustics, Speech, and Signal Processing (ICASSP)*, Apr. 1990.
- [55] Kaleem, M., Guergachi, A., and Krishnan, S., "Application of a Variation of Empirical Mode Decomposition and Teager Energy Operator to EEG Signals for Mental Task Classification," in *Proc. 35th Annual Int'l Conf. of the IEEE Engineering in Medicine and Biology Society (EMBC)*, Jul. 2013.
- [56] Katsigiannis, S. and Ramzan, N., "DREAMER: A Database for Emotion Recognition Through EEG and ECG Signals From Wireless Low-cost Off-the-Shelf Devices," *IEEE Journal of Biomedical and Health Informatics*, vol. 22, no. 1, pp. 98–107, Mar. 2018.

Bibliography Bibliography

[57] Kerkeni, L., Serrestou, Y., Raoof, K., Mbarki, M., Mahjoub, M. A., and Cleder, C., "Automatic speech emotion recognition using an optimal combination of features based on EMD-TKEO," *Speech Communication*, vol. 114, pp. 22–35, Nov. 2019.

- [58] Khaldi, K., Boudraa, A.-O., and Komaty, A., "Speech enhancement using empirical mode decomposition and the Teager-Kaiser energy operator," *The Journal of the Acoustical Society of America*, vol. 135, no. 1, pp. 451–459, Jan. 2014.
- [59] Koelstra, S., Muhl, C., Soleymani, M., Lee, J.-S., Yazdani, A., Ebrahimi, T., Pun, T., Nijholt, A., and Patras, I., "DEAP: A Database for Emotion Analysis using Physiological Signals," *IEEE transactions on affective computing*, vol. 3, no. 1, pp. 18–31, Jun. 2011.
- [60] Krishnapriya, G., Ponnalagu, R., and Goel, S., "Accuracy Improved Muscle Onset and Termination Detection in EMG Signal Processing Using STKEO," in *Proc. 16th Int'l Conf. on Sensing Technology (ICST)*, IEEE, Dec. 2023.
- [61] Ladda, A., Lebon, F., and Lotze, M., "Using motor imagery practice for improving motor performance A review," *Brain and Cognition*, vol. 150, p. 105705, Jun. 2021.
- [62] Lahane, P. and Thirugnanam, M., "Human emotion detection and stress analysis using EEG signal," *International Journal of Innovative Technology and Exploring Engineering (IJITEE)*, vol. 8, no. 4S2, pp. 96–100, Mar. 2019.
- [63] Lange, C. and James, W., "The emotions, Vol. 1.," 1922.
- [64] Lebon, F., Collet, C., and Guillot, A., "Benefits of Motor Imagery Training on Muscle Strength," *Journal of Strength and Conditioning Research*, vol. 24, no. 6, pp. 1680–1687, Jun. 2010.
- [65] Li, H., Zhang, Q., Lin, Z., and Gao, F., "Prediction of Epilepsy Based on Tensor Decomposition and Functional Brain Network," *Brain sciences*, vol. 11, no. 8, p. 1066, Aug. 2021.
- [66] Li, K., Li, M., Liu, W., Wu, Y., Li, F., Xie, J., Zhou, S., Wang, S., Guo, Y., Pan, J., and Wang, X., "Electroencephalographic differences between waking and sleeping periods in patients with prolonged disorders of consciousness at different levels of consciousness," Frontiers in Human Neuroscience, vol. 19, p. 1521355, Feb. 2025.
- [67] Li, M., Chen, W., and Zhang, T., "Classification of epilepsy EEG signals using DWT-based envelope analysis and neural network ensemble," *Biomedical Signal Processing and Control*, vol. 31, pp. 357–365, Jan. 2017.

[68] Lin, C.-L. and Chen, L.-T., "Improvement of brain-computer interface in motor imagery training through the designing of a dynamic experiment and FBCSP," *Heliyon*, vol. 9, no. 3, e13745, Mar. 2023.

- [69] Lin, X., Chen, J., Ma, W., Tang, W., and Wang, Y., "EEG emotion recognition using improved graph neural network with channel selection," *Computer Methods and Programs in Biomedicine*, vol. 231, p. 107380, Apr. 2023.
- [70] Liu, H., Zhang, Y., Li, Y., and Kong, X., "Review on Emotion Recognition Based on Electroencephalography," Frontiers in Computational Neuroscience, vol. 15, p. 758 212, Oct. 2021.
- [71] Lotze, M. and Halsband, U., "Motor imagery," *Journal of Physiology-Paris*, vol. 99, no. 4–6, pp. 386–395, Jun. 2006.
- [72] Lundberg, S. and Lee, S.-I., "A Unified Approach to Interpreting Model Predictions," in Advances in Neural Information Processing Systems, I. Guyon, U. V. Luxburg, S. Bengio, H. Wallach, R. Fergus, S. Vishwanathan, and R. Garnett, Eds., Curran Associates, Inc., Dec. 2017.
- [73] Mahmoud, A., Amin, K., Al Rahhal, M., Elkilani, W., Mekhalfi, M., and Ibrahim, M., "A CNN Approach for Emotion Recognition via EEG," Symmetry, vol. 15, no. 10, Sep. 2023.
- [74] Maragos, P., Kaiser, J., and Quatieri, T., "Energy separation in signal modulations with application to speech analysis," *IEEE Transactions on Signal Processing*, vol. 41, no. 10, pp. 3024–3051, Oct. 1993.
- [75] Martisius, I., Damasevicius, R., Jusas, V., and Birvinskas, D., "Using Higher Order Nonlinear Operators for SVM Classification of EEG Data," *Electronics and Electrical Engineering*, vol. 119, no. 3, pp. 99–102, Mar. 2012.
- [76] McDermott, B., Porter, E., Hughes, D., McGinley, B., Lang, M., O'Halloran, M., and Jones, M., "Gamma Band Neural Stimulation in Humans and the Promise of a New Modality to Prevent and Treat Alzheimer's Disease," *Journal of Alzheimer's Disease*, vol. 65, no. 2, A. Clements-Cortes, Ed., pp. 363–392, Jul. 2018.
- [77] Mokienko, O., Chernikova, L., Frolov, A., and Bobrov, P., "Motor Imagery and Its Practical Application," *Neuroscience and Behavioral Physiology*, vol. 44, no. 5, pp. 483–489, May 2014.
- [78] Monteiro, K., Cardoso, M. d. S., Cabral, V. d. C., Santos, A. dos, Silva, P. da, Castro, J. de, and Vale, R. d. S., "Effects of Motor Imagery as a Complementary Resource on the Rehabilitation of Stroke Patients: A Meta-Analysis of Randomized Trials," *Journal of Stroke and Cerebrovascular Diseases*, vol. 30, no. 8, p. 105 876, Aug. 2021.

[79] mrAnmol, "Circumplex model of emotion," Jun. 2023, Available: https://commons.wikimedia.org/wiki/File:Circumplex_model_of_emotion.svg.

- [80] Murariu, M.-G., Tărniceriu, D., Hrișcă-Eva, O.-D., and Lazăr, A.-M., "An Approach to Identify Different Types of EEG Epileptic Signals Based on Higher-Order Spectra (HOS) Features," in *Proc. 14th Int'l Conf. on Electronics, Computers and Artificial Intelligence (ECAI)*, IEEE, Jun. 2022.
- [81] Naik, G. and Kumar, D., "An overview of independent component analysis and its applications," *Informatica*, vol. 35, no. 1, pp. 63–81, Jan. 2011.
- [82] Nait-Ali, A., Advanced Biosignal Processing. Springer Science & Business Media, Dec. 2009.
- [83] Neofect, "Brain Anatomy 101: Major Structures and Functions," Nov. 2019, Available: https://www.neofect.com/us/blog/brain-anatomy-101-major-structures-and-functions.
- [84] Nguyen, D., Barbieri, R., Wilson, M., and Brown, E., "Instantaneous frequency and amplitude modulation of EEG in the hippocampus reveals state dependent temporal structure," in *Proc. 30th Annual Int'l Conf. of the IEEE Engineering in Medicine and Biology Society*, Aug. 2008.
- [85] Niaki, M., Dharia, S., Chen, Y., and Valderrama, C., "Bipartite Graph Adversarial Network for Subject-Independent Emotion Recognition," *IEEE Journal of Biomedical and Health Informatics*, vol. 29, no. 10, pp. 7234–7247, May 2025.
- [86] Oishi, K., Kasai, T., and Maeshima, T., "Autonomic Response Specificity during Motor Imagery," *Journal of Physiological Anthropology and Applied Human Science*, vol. 19, no. 6, pp. 255–261, Nov. 2000.
- [87] Oppenheim, A. and Schafer, R., *Discrete-Time Signal Processing*, 3rd. USA: Prentice Hall Press, Aug. 2009.
- [88] Padfield, N., Zabalza, J., Zhao, H., Masero, V., and Ren, J., "EEG-Based Brain-Computer Interfaces Using Motor-Imagery: Techniques and Challenges," *Sensors*, vol. 19, no. 6, p. 1423, Mar. 2019.
- [89] Palumbo, A., Gramigna, V., Calabrese, B., and Ielpo, N., "Motor-Imagery EEG-Based BCIs in Wheelchair Movement and Control: A Systematic Literature Review," *Sensors*, vol. 21, no. 18, p. 6285, Sep. 2021.
- [90] Pandey, P. and Seeja, K., "Subject independent emotion recognition from EEG using VMD and deep learning," *Journal of King Saud University-Computer and Information Sciences*, vol. 34, no. 5, pp. 1730–1738, May 2022.

Bibliography Bibliography

[91] Pane, E., Wibawa, A., and Pumomo, M., "Channel Selection of EEG Emotion Recognition using Stepwise Discriminant Analysis," in *Proc. Int'l Conf. on Computer Engineering, Network and Intelligent Multimedia (CENIM)*, Nov. 2018.

- [92] Patil, H. A., Kamble, M. R., Patel, T. B., and Soni, M. H., "Novel Variable Length Teager Energy Separation Based Instantaneous Frequency Features for Replay Detection," in *Proc. Interspeech*, ISCA, Aug. 2017.
- [93] Plutchik, R., "A psychoevolutionary theory of emotions," Soc. Sci. Inf. (Paris), vol. 21, no. 4-5, pp. 529–553, Jul. 1982.
- [94] Plutchik, R., "The nature of emotions," American Scientist, vol. 89, no. 4, pp. 344–350, Jul. 2001.
- [95] Ravi and Taran, S., "A nonlinear feature extraction approach for speech emotion recognition using VMD and TKEO," *Applied Acoustics*, vol. 214, p. 109667, Nov. 2023.
- [96] Risqiwati, D., Wibawa, A. D., Pane, E. S., Islamiyah, W. R., Tyas, A. E., and Purnomo, M. H., "Feature Selection for EEG-Based Fatigue Analysis Using Pearson Correlation," in *Proc. Int'l Seminar on Intelligent Technology and Its Applications (ISITIA)*, IEEE, Jul. 2020.
- [97] Russell, J., "A circumplex model of affect," Journal of personality and social psychology, vol. 39, no. 6, pp. 1161–1178, Dec. 1980.
- [98] Russell, J. and Mehrabian, A., "Evidence for a three-factor theory of emotions," *Journal of research in Personality*, vol. 11, no. 3, pp. 273–294, Sep. 1977.
- [99] S., T., "Nerve Cells (Neurons): Types, Structure, Functions, Diseases," Apr. 2024, Available: https://microbenotes.com/nerve-cells/.
- [100] Scherer, R. and Vidaurre, C., "Chapter 8 Motor imagery based brain-computer interfaces," in *Smart Wheelchairs and Brain-Computer Interfaces*, P. Diez, Ed., Academic Press, 2018, pp. 171–195.
- [101] Schomer, D. and Lopes da Silva, F., Niedermeyer's Electroencephalography: Basic Principles, Clinical Applications, and Related Fields. Oxford University Press, Nov. 2017.
- [102] Siddiqui, M. M., Srivastava, G., and Saeed, S. H., "Diagnosis of insomnia sleep disorder using short time frequency analysis of PSD approach applied on EEG signal using channel ROC-LOC," *Sleep Science*, vol. 9, no. 3, pp. 186–191, Jul. 2016.
- [103] Smith, E. E., Reznik, S. J., Stewart, J. L., and Allen, J. J., "Assessing and conceptualizing frontal EEG asymmetry: An updated primer on recording, processing, analyzing,

- and interpreting frontal alpha asymmetry," *International Journal of Psychophysiology*, vol. 111, pp. 98–114, Jan. 2017.
- [104] Song, T., Zheng, W., Liu, S., Zong, Y., Cui, Z., and Li, Y., "Graph-embedded convolutional neural network for image-based EEG emotion recognition," *IEEE Transactions on Emerging Topics in Computing*, vol. 10, no. 3, pp. 1399–1413, Jun. 2021.
- [105] Song, T., Zheng, W., Lu, C., Zong, Y., Zhang, X., and Cui, Z., "MPED: A Multi-Modal Physiological Emotion Database for Discrete Emotion Recognition," *IEEE Access*, vol. 7, pp. 12177–12191, Jan. 2019.
- [106] Sudhakar Jebaraj, G. and Elango, K., "A Comprehensive Review of EEG-Based Seizure Detection Techniques," *IEEE Access*, vol. 13, pp. 103531–103564, Jun. 2025.
- [107] Supratak, A., Wu, C., Dong, H., Sun, K., and Guo, Y., "Survey on feature extraction and applications of biosignals," in *Machine Learning for Health Informatics: State-of-the-Art and Future Challenges*, A. Holzinger, Ed. Cham: Springer International Publishing, Dec. 2016, pp. 161–182.
- [108] Tawhid, M., Siuly, S., and Li, T., "A Convolutional Long Short-Term Memory-Based Neural Network for Epilepsy Detection From EEG," *IEEE Transactions on Instru*mentation and Measurement, vol. 71, pp. 1–11, Oct. 2022.
- [109] Teplan, M., "Fundamentals of EEG Measurement," Measurement Science Review, vol. 2, pp. 1–11, Jan. 2002.
- [110] Tjepkema-Cloostermans, M., Carvalho, R. de, and Putten, M. van, "Deep learning for detection of focal epileptiform discharges from scalp EEG recordings," *Clinical Neurophysiology*, vol. 129, no. 10, pp. 2191–2196, Oct. 2018.
- [111] Uyttenhove, T., Maes, A., Steenkiste, T. V., Deschrijver, D., and Dhaene, T., "Interpretable Epilepsy Detection in Routine, Interictal EEG Data using Deep Learning," in *Proc. of the Machine Learning for Health NeurIPS Workshop*, E. Alsentzer, M. B. A. McDermott, F. Falck, S. K. Sarkar, S. Roy, and S. L. Hyland, Eds., ser. Proceedings of Machine Learning Research, Dec. 2020.
- [112] Veloso, L., McHugh, J., Weltin, E. von, Lopez, S., Obeid, I., and Picone, J., "Big data resources for EEGs: Enabling deep learning research," in *Proc. IEEE Signal Processing in Medicine and Biology Symposium (SPMB)*, Nov. 2017.
- [113] Wang, X., Wang, A., Zheng, S., Lin, Y., and Yu, M., "A Multiple Autocorrelation Analysis Method for Motor Imagery EEG Feature Extraction," in *Proc. 26th Chinese Control and Decision Conf. (2014 CCDC)*, IEEE, May 2014.

[114] Wei, B., Zhao, X., Shi, L., Xu, L., Liu, T., and Zhang, J., "A deep learning framework with multi-perspective fusion for interictal epileptiform discharges detection in scalp electroencephalogram," *Journal of Neural Engineering*, vol. 18, no. 4, 0460b3, Jul. 2021.

- [115] Xu, F., Miao, Y., Sun, Y., Guo, D., Xu, J., Wang, Y., Li, J., Li, H., Dong, G., Rong, F., Leng, J., and Zhang, Y., "A transfer learning framework based on motor imagery rehabilitation for stroke," *Scientific Reports*, vol. 11, no. 1, p. 19783, Oct. 2021.
- [116] Yuan, Q., Zhou, W., Liu, Y., and Wang, J., "Epileptic seizure detection with linear and nonlinear features," *Epilepsy & Behavior*, vol. 24, no. 4, pp. 415–421, Aug. 2012.
- [117] Zanetti, R., Pale, U., Teijeiro, T., and Atienza, D., "Approximate zero-crossing: A new interpretable, highly discriminative and low-complexity feature for EEG and iEEG seizure detection," *Journal of Neural Engineering*, vol. 19, no. 6, p. 066018, Nov. 2022.
- [118] Zebende, G., Oliveira Filho, F., and Leyva Cruz, J., "Auto-correlation in the motor/imaginary human EEG signals: A vision about the FDFA fluctuations," *PLOS ONE*, vol. 12, no. 9, D. Yao, Ed., e0183121, Sep. 2017.
- [119] Zeng, W., Su, B., Yuan, C., and Chen, Y., "Automatic detection of heart valve disorders using Teager–Kaiser energy operator, rational-dilation wavelet transform and convolutional neural networks with PCG signals," *Artificial Intelligence Review*, vol. 56, no. 1, pp. 781–806, Apr. 2022.
- [120] Zhang, D., Yao, L., Chen, K., and Monaghan, J., "A Convolutional Recurrent Attention Model for Subject-Independent EEG Signal Analysis," *IEEE signal processing letters*, vol. 26, no. 5, pp. 715–719, Mar. 2019.
- [121] Zhang, J. and Wang, M., "A survey on robots controlled by motor imagery brain-computer interfaces," *Cognitive Robotics*, vol. 1, pp. 12–24, Feb. 2021.
- [122] Zheng, W.-L. and Lu, B.-L., "Investigating Critical Frequency Bands and Channels for EEG-Based Emotion Recognition with Deep Neural Networks," *IEEE Transactions on Autonomous Mental Development*, vol. 7, no. 3, pp. 162–175, May 2015.
- [123] Zlatintsi, Α., "Επεξεργασία σημάτων μουσικής και εφαρμογές αναγνώρισης," 2014.
- [124] Zlatintsi, A. and Maragos, P., "Am-fm modulation features for music instrument signal analysis and recognition," in *Proc. 20th European Signal Processing Conf. (EU-SIPCO)*, Aug. 2012.

[125] Zlatintsi, A. and Maragos, P., "Multiscale Fractal Analysis of Musical Instrument Signals With Application to Recognition," *IEEE Transactions on Audio, Speech, and Language Processing*, vol. 21, no. 4, pp. 737–748, Nov. 2013.

[126] Zlatintsi, A. and Maragos, P., "Comparison of different representations based on non-linear features for music genre classification," in *Proc. 22nd European Signal Processing Conf. (EUSIPCO)*, Sep. 2014.